# An Investigation of the Effects of the Processing Parameters on Laser Powder Bed Fused 17-4 PH Stainless Steel

By

**Keshav Malhotra**

A Thesis Submitted to the Faculty of Graduate Studies of

The University of Manitoba

In Partial Fulfilment of the Requirements of the Degree of

**MASTER OF SCIENCE**

Department of Mechanical Engineering

University of Manitoba

Winnipeg

Copyright ©__2025 by Keshav Malhotra

# Abstract

The 17-4 precipitation hardened (PH) series of stainless steel (SS), which is well known for its exceptional mechanical strength and corrosion resistance, has been extensively employed in the aerospace, automotive, and biomedical sectors. 17-4 PH SS is particularly suitable for laser powder bed fusion (LPBF) due to its inherent weldability. Despite its advantages, the intricate interplay of the LPBF process parameters can result in components with inconsistent mechanical properties, which are predominantly attributed to the formation of manufacturing defects and variations in phase composition. However, the influence of the process parameters on these variables has yet to be fully understood. This study conducts a comprehensive quantitative investigation of microstructural manufacturing defects across a matrix of different combinations of process parameters, including laser power, scanning speed, and powder bed preheating temperature, to delineate an optimal process window. The defect-free samples are also subjected to a post-LPBF heat treatment. The microstructural phases present in the material are examined and quantified in both the as-built and heat-treated conditions by using x-ray diffraction and transmission electron microscopy. A high relative density that exceeds 99.5% is consistently achieved within the identified process window, although variations in phase composition are observed. After the heat treatment, the samples fabricated under the optimized conditions show a uniform phase composition and superior mechanical properties. This investigation elucidates the critical impact of LPBF process parameters on the formation of manufacturing defects and microstructural changes in 17-4 PH SS, thus providing insights into refining the LPBF process to yield defect-free builds with improved mechanical properties.

## Acknowledgements

The successful completion of this project would not have been possible without the support and guidance of several individuals. First and foremost, I would like to express my sincere gratitude to my supervisor, **Dr. Olanrewaju Ojo**, and my co-supervisor, **Dr. Guozhen Zhu**, for granting me the opportunity to pursue my M.Sc. at the University of Manitoba and for their steadfast technical guidance and encouragement throughout this degree. I am also deeply thankful to **Dr. Ehab Samuel** for his valuable insights and continuous support, as well as for giving me the opportunity to work on this project.

I would also like to extend my heartfelt thanks to **Dr. Lina Zhang** and **Mike Boswick** for their invaluable technical guidance and support throughout the course of this project. Special thanks are due to **Dr. Abdul Khan** at the *Manitoba Institute of Materials* and **Mark Cooper** from the *Geological X-Ray Laboratory* at the University of Manitoba for their assistance with the transmission electron microscopy and X-ray diffraction analyses. I am sincerely grateful to my examination committee, **Dr. Chuang Deng** and **Dr. Qingjin Peng**, for their time, thoughtful feedback, and interest in my work. I would also like to acknowledge the **University of Manitoba**, **National Research Council Canada(NRC)**, and **Natural Sciences and Engineering Research Council (NSERC)** of Canada for their generous financial support throughout my studies.

Finally, I would like to express my deepest gratitude to my parents, **Dinesh and Neetu Malhotra**, my brother **Saket Malhotra**, and my partner **Madhuri Sinha** for their unwavering belief in me and their constant support throughout every step of this journey. Their love, encouragement, and patience have been my greatest source of strength.

# Dedication

I dedicate this thesis to my father, **Dinesh Malhotra**; my mother, **Neetu Malhotra**; my grandmother, **Asha Ahuja**; my brother, **Saket Malhotra**; and my partner, **Madhuri Sinha**. Your unwavering support, encouragement, and love have been my greatest sources of strength throughout this journey. I am deeply grateful for your constant presence and belief in me.

# Table of Contents

**Abstract** ..... ii

**Acknowledgements** ..... iii

**Dedication** ..... iv

**List of Figures** ..... viii

**List of Tables** ..... x

**Chapter 1: Introduction** ..... 1

**1.1 Background** ..... 1

**1.2 Thesis Objectives** ..... 2

**1.3 Thesis Organization** ..... 3

**Chapter 2: Literature Review** ..... 4

**2.1 Metal Additive Manufacturing** ..... 4

**2.1.1 Laser Powder Bed Fusion** ..... 6

**2.1.1.1 Lack of Fusion Defects** ..... 8

**2.1.1.2 Keyhole Defects** ..... 8

**2.1.1.3 Balling** ..... 9

**2.1.1.4 Gas Porosity** ..... 9

**2.1.1.5 Oxidation** ..... 10

**2.1.1.6 Loss of Alloying Elements** ..... 10

**2.1.1.7 Cracking** ..... 11

**2.1.2 Influence of Process Parameters on Formation of Manufacturing Defects** ..... 12

**2.1.2.1 Laser Power and Scanning Speed** ..... 12

**2.1.2.2 Hatch Distance and Layer Thickness** ..... 15

**2.1.2.3 Laser Scanning Strategy** ..... 16

**2.1.2.4 Powder Bed Preheating** ..... 17

**2.2 LPBF of 17-4 PH SS** ..... 19

**2.2.1 Influence of Various Process Parameters on the As-built Condition** ..... 20

**2.2.1.1 Powder Characteristics** ..... 20

**2.2.1.2 Effect of Parameters Affecting Energy Density** ..... 21

**2.2.1.3 Laser Scanning Strategy** ..... 22

**2.2.1.4 Powder Bed Preheating** ..... 24

**2.2.2 Effect of Heat Treatment** ..... 24
**2.3 Summary and Research Gap** ..... 28
**Chapter 3: Materials and Methodology** ..... 31
**3.1 Experimental Plan** ..... 31
**3.2 Production of Test Materials** ..... 32
**3.2.1 Powder Characterization** ..... 32
**3.2.2 Printing of Specimens** ..... 33
**3.2.3 Heat Treatment** ..... 36
**3.3 Manufacturing Defect Quantification and Analysis** ..... 36
**3.3.1 Sample Preparation and Imaging** ..... 36
**3.3.2 Customized Python Script** ..... 37
**3.3.3 Scanning Electron Microscopy** ..... 39
**3.4 Material Characterization** ..... 39
**3.4.1 Metallography** ..... 40
**3.4.2 X-Ray Diffraction** ..... 40
**3.4.3 Transmission Electron Microscopy** ..... 40
**3.5 Mechanical Testing** ..... 41
**3.5.1 Hardness Testing** ..... 41
**3.5.2 Tensile Testing** ..... 41
**Chapter 4: Results and Discussion** ..... 43
**4.1 Effect of Process Parameters on Manufacturing Defects** ..... 43
**4.1.1 Effect of Laser Scanning Speed** ..... 43
**4.1.2 Effect of Laser Power** ..... 48
**4.1.3 Effect of Powder Bed Preheating Temperature** ..... 52
**4.1.4 Summary of Process Parameters and Defect Formation** ..... 57
**4.2 Mechanical Performance of the As-built Material** ..... 58
**4.2.1 Effect of Manufacturing Defects on Mechanical Behavior** ..... 59
**4.2.2 Samples with Near-zero Manufacturing Defects** ..... 62
**4.2.3 Summary of Mechanical Properties in As-built Condition** ..... 72
**4.3 Effect of Heat Treatment** ..... 74
**4.3.1 Effect on Phases** ..... 74
**4.3.2 Effect on Mechanical Properties** ..... 77

**4.3.3 Summary of Effect of Heat Treatment** ..... 81
**4.4 Summary of Results** ..... 82
**Chapter 5: Conclusions** ..... 85
**5.1 Effect of Process Parameters on Formation of Manufacturing Defects** ..... 85
**5.2 Mechanical Behaviour of As-built Samples** ..... 86
**5.3 Effect of Heat Treatment** ..... 86
**Chapter 6: Recommendations for Future Work** ..... 88
**References** ..... 90

# List of Figures

**Figure 2.1** Classification of Single-Step Metal Additive Technologies as per ASTM F2792-12 [9] ..... 5
**Figure 2.2** Schematic of LPBF machine ..... 7
**Figure 2.3** Schematic process map with laser power and scanning speed ..... 15
**Figure 2.4** Schematic representation of (a) stripe, (b) chessboard, and (c) hexagonal scanning strategies ..... 17
**Figure 2.5** Schematic of effect of powder bed preheating on LPBF process ..... 19
**Figure 2.6** Standard heat treatment cycles for precipitation hardening of 17-4 PH SS ..... 25
**Figure 2.7** Mechanical properties of 17-4 PH SS produced through LPBF, after heat treatment (Condition A + H900) based on literature compared to ASTM A693 [80] ..... 27
**Figure 2.8** Fractured surfaces of tensile test samples produced in optimized window as reported by (a, c) Kovacs et al. [6] , and (b, d) Mahmoudi et al. [81] at lower and higher magnifications which reveal unmelted powder ..... 28
**Figure 3.1** SEM image of 17-4 H SS powder at (a) lower magnification with size distribution, and (b) high magnification showing some satellite particles ..... 31

**Figure 3.2** Images of printing setup: (a) main printer, (b) supporting stations, and (c) an in-process image ..... 33

**Figure 3.3** Sample printed for (a) microstructural analysis, and (b) blanks for tensile testing ..... 34

**Figure 3.4** Methodology for calculating fractions of manufacturing defect from optical micrographs ..... 37

**Figure 3.5** Method used to obtain samples for (a) tensile testing from additively manufactured material, along with (b) detailed dimensions ..... 42
**Figure 4.1** Effect of scanning speed on manufacturing defect formation shown through (a) optical micrographs, and (b) data across all laser powers, with trends of (c) low energy density, (d) moderate energy density, and (e) high energy density regimes ..... 45

**Figure 4.2** Effect of laser scanning speed on manufacturing defect size distribution, for samples printed at 200 W and (a) 1600 mm/s, (b) 1200 mm/s, (c) 1000 mm/s and (d) 250 W, 600 mm/s ..... 46

**Figure 4.3** (a) Optical micrograph and corresponding SEM image of sample built in low LED regime which shows unmelted powder particles. Etched optical micrographs reveal (b) insufficient overlap of melt pool in the low LED sample and (c) large circular (keyhole) defects in the high LED sample ..... 48

**Figure 4.4** Effect of laser power on manufacturing defect formation: (a) optical micrographs, and (b) data across all scanning speeds, with patterns show for (c) low energy density, (d) moderate energy density, and (e) high energy density regimes ..... 50

**Figure 4.5** Optical micrographs of samples produced at (a) 150 W (poor), (b) 200 W (Intermediate-low LED), and (c)300 W (Intermediate-high LED) that show manufacturing defect formation mechanism of each case ..... 51

**Figure 4.6** Optical micrographs that show effect of powder bed preheating on manufacturing defects for samples produced at different laser power and scanning speeds .....53
**Figure 4.7** Manufacturing defect fraction with (a) process map across increasing powder bed preheating temperatures, (b) energy density dependence, and (c) enhanced working ranges .55
**Figure 4.8** Etched micrographs that show partial melt pool overlap at (a) 200ºC, and (b) 300ºC, and complete melt pool overlap at (c) 400ºC, and (d) 500ºC .....57
**Figure 4.9** Correlation of (a) hardness, (b) strength, and (c) ductility with manufacturing defect fraction and LED……..60

**Figure 4.10** Tensile properties of samples in as-built condition, compared to samples that follow ASTM A693-24 in terms of (a) strength, and (b) ductility……61

**Figure 4.11** Hardness of samples within optimal processing window that show near zero manufacturing defects.....63
**Figure 4.12** Samples with near-zero manufacturing defects that show varying (a) tensile curves, (b) yield strength, and (c) ductility…….…..63

**Figure 4.13** Optical micrograph that show dual grain structure of fully dense samples built at (a) 200°C, (b) 300°C, (c) 400°C, and (d) 500°C……..65

**Figure 4.14** XRD patterns for the samples built at (a) lower (200°C, and 300°C), and (b) higher (400°C and 500°C) powder bed temperatures .....66
**Figure 4.15** (a) TEM image and corresponding selected area diffraction pattern (SADP), (b) corresponding high-angle annular dark-field (HAADF) image, and (c)-(i) EDS mapping which reveals nano-scale oxides without any copper clustering in as-built condition.....67
**Figure 4.16** Schematic CCT curves for LPBF produced 17-4 PH SS to explain variation with powder bed preheating temperature……..68

**Figure 4.17** Correlating preheating temperature with amount of retained austenite, and (a) hardness, (b) strength, and (c) ductility .....70
**Figure 4.18** Work hardening behavior of the samples built at (a) 200ºC, (b) 300ºC, (c) 400ºC, and 500ºC.....71
**Figure 4.19** Optical micrographs of heat-treated samples with different combinations of process parameters .....75
**Figure 4.20** X-ray diffraction patterns of samples built at (a) 200ºC, 300ºC, and (b) 400ºC, 500ºC in the fully heat-treated condition……...74

**Figure 4.21** STEM image of (a) heat-treated condition that shows spherical precipitates of two kinds (b) fine Cu-rich and Nb-rich precipitates, and the corresponding EDS maps (c) - (f)…...75

**Figure 4.22** Hardness of manufacturing defect free-samples built with (a) different processing conditions, after heat treatment and comparison with (b) as-built samples……..76

**Figure 4.23** Comparison of (a) elongation, (b) UTS, and (c) yield strength, of heat-treated samples, with the as-built samples and the standard expectations of the alloy .....79
**Figure 4.24** Tensile properties of LPBF manufactured samples, following heat treatment procedures in literature, and current study, compared to ASTM standard requirements.....81

# List of Tables

**Table 3.1** Chemical composition of powder used for printing 17-4 PH SS..... 32
**Table 3.2** Recipes used for process parameter investigation of 17-4PH SS ..... 34
**Table 3.3** Recipes used for producing blanks for tensile testing and category..... 35
**Table 3.4** Results for select samples from each category calculated by using traditional image analysis method with Image J software vs. customized Python script compared via paired t-test ..... 39

# Chapter 1: Introduction

## 1.1 Background

Since its advent, metal additive manufacturing (AM) has enabled the fabrication of products with highly complex geometries, thus overcoming many of the constraints inherent to traditional subtractive manufacturing methods. Metal AM has been widely adopted in industries such as the aerospace, biomedical, and automotive sectors due to its ability to produce intricate components with customized properties. Among the different metal AM techniques, laser powder bed fusion (LPBF) is at the forefront because this method offers exceptional resolution and structural integrity. However, the process subjects materials to extreme cooling rates and complex thermal cycles, which lead to manufacturing defects (e.g., cracking, loss of alloying elements, oxidation, etc.) and phase composition problems. These thermal conditions are greatly influenced by the process parameters, making their optimization essential for achieving high-quality LPBF builds.

The 17 -4 precipitation hardened (PH) stainless steel (SS) is a material that has been widely used in various industries, and has remained one of the most successful precipitate-hardened SSs since the 1940s [1]. 17-4 PH SS offers exceptional corrosion resistance and mechanical strength, which makes it ideal for applications that require these properties. Industries such as the aerospace, biomedical, oil and gas, and automotive industries favour 17-4 PH SS due to its exceptional performance in harsh environments. Its excellent corrosion resistance to a variety of different environments and high-temperature oxidation are due to its contents of 17% chromium and 4% nickel. Its ability to form nano-scale copper-rich clusters following a PH heat treatment further enhances its strength. Finally, 17-4 PH SS exhibits good weldability, thus making it a strong candidate for the LPBF process.

Despite the good printability of 17-4 PH SS, the extreme cooling rates of the LPBF process lead to unpredictable mechanical properties [2], [3], [4], [5]. Printed builds often fail to meet ASTM mechanical property requirements [6], [7] which show significant variations due to manufacturing defects and phase composition inconsistencies. Even after a commercial heat treatment, residual manufacturing defects can act as stress concentrators, thus resulting in reduced ductility and strength of 17-4 PH SS. Additionally, phase variations may persist, which inhibits the PH process and prevents the formation of strengthening copper precipitates, thus ultimately causing a significant loss in strength [8]. Therefore, a more in-depth understanding of the correlations among the process parameters, manufacturing defects, and changes in the phases is crucial to increase the reliability of additively manufactured 17-4 PH SS.

## 1.2 Thesis Objectives

The objectives of this thesis are as follows:

1. To investigate the influence of the process parameters on the formation of microstructural manufacturing defects in order to identify an optimal processing window and understand the underlying mechanisms that are responsible for manufacturing defects
2. To evaluate the mechanical response of as-built samples by correlating the response with manufacturing defects and the processing parameters. Additionally, to investigate whether the mechanical behavior is affected by other microstructural variables in the absence of manufacturing defects, and
3. To investigate how LPBF-manufactured 17-4 PH SS responds to commercial heat treatment, by specifically examining the changes in the phases and corresponding changes in mechanical properties.

## 1.3 Thesis Organization

This thesis is structured as follows.

- **Chapter 1** provides the background information, discusses the motivation, and lists the objectives of the research work.
- **Chapter 2** presents a detailed literature review. First, the primary metal AM technologies and LPBF are summarized with a primary focus on issues related to LPBF due to improper process parameter selection, and their implications for the mechanical properties. Secondly, the material-specific problems encountered in LPBF-produced 17-4 PH SS are discussed, thus pointing out the research gaps.
- **Chapter 3** details the experimental plan used to answer the research objectives, along with details of the equipment utilized for the work.
- **Chapter 4** presents the results obtained and discusses their implications.
- **Chapter 5** points out some of the limitations, and recommends areas for future research work.
- **Chapter 6** draws conclusions based on the information in the previous chapters.

# Chapter 2: Literature Review

This chapter provides a comprehensive review of the literature on the LPBF process of 17-4 PH SS. The chapter is structured into two main sections. The first section provides an introduction on metal AM, with a focus on LPBF. Common manufacturing defects that arise from improper process parameter selection and their impact on the mechanical properties are discussed. The second section explores the LPBF processing of 17-4 PH SS, which emphasizes how researchers have studied the influence of the process parameters on an as-built microstructure and properties. The chapter then examines the response of the material to conventional heat treatment. Finally, the chapter summarizes the key findings in the literature and highlights gaps in existing research work.

## 2.1 Metal Additive Manufacturing

In ASTM F2792-12, ASTM International defines metal AM as "(a) process of joining metals to make objects from a 3D model data, usually, layer upon layer, as opposed to subtractive manufacturing technologies" [9]. Metal AM allows the production of designs that were once considered not possible due to the geometric limitations of traditional subtractive methods. Metal AM is a general term and many manufacturing methods like three-dimensional (3D) printing, binder jetting, extrusion, powder bed fusion or even sheet lamination fall under this umbrella term. All of these processes are typically executed layer-by-layer from a ".STL" file generated by slicing a CAD model, which allows for the production of nearly any thinkable design.

As shown in **Figure 2.1**, metal AM processes can be divided into two categories based on the method of fusion: the solid-state method, and the molten-state method. While the solid-state

method typically uses a sheet metal material and bond a stack of sheets by using ultrasonic welding, the molten-state method creates a build-on substrate by using an energy source. These processes can be divided into two standard categories [10], with one being direct energy deposition (DED), and the other being powder bed fusion (PBF).

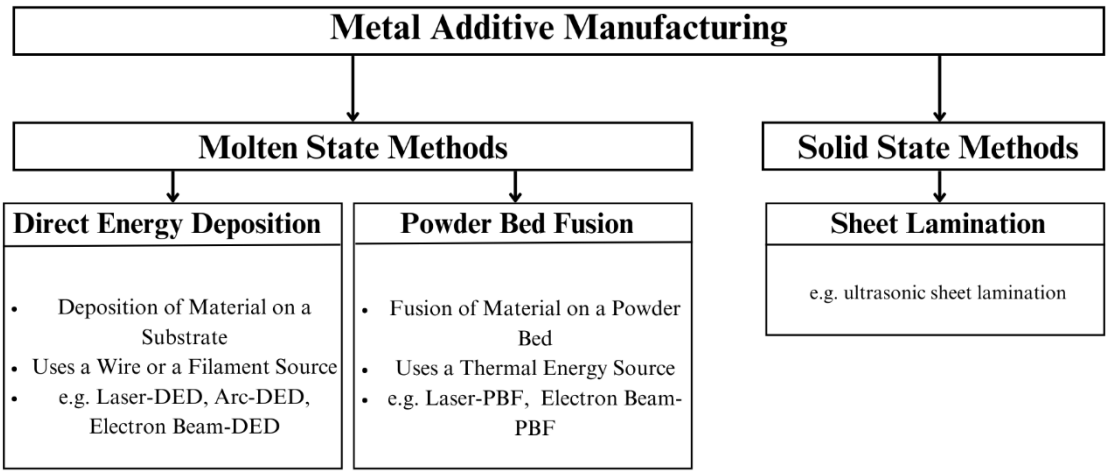



**Figure 2.1** Classification of Single-Step Metal Additive Technologies as per ASTM F2792-12 [9]

A typical DED method feeds wire or powder material through a nozzle, and an energy source is used that selectively melts the material and then deposits the material onto the substrate in the desired shape. The DED process uses various energy sources, the most commonly used are the wire arc, a laser beam, or an electron beam. DED has a fast build rate and can be used to build a material if it can be welded. However, owing to the large diameter of the deposited wire, it is difficult to achieve a high-resolution deposit.

A PBF process on the other hand, uses a metal powder, supplied by a powder chamber, with an energy source successively scanning the desired contours and welding the material to a base plate. Similar to DED processes, a variety of energy sources may be used, with the most common ones being a laser, which results in the LPBF process, and an electron beam, which results in the electron beam powder bed fusion (EB-PBF) process. Materials that can be joined by laser or electron beam welding are suitable for this process. The PBF process allows for the

production of components with a very high resolution and can create extremely intricate parts. This, however, comes at the cost of longer build times.

Both the DED and PBF processes require metal with good weldability to produce the components. The build is deposited onto a plate and has to be separated following the deposition. Among the two methods, DED provides a high build rate so that the method is suitable for repair work of large-scale components like those used in the automobile and aerospace industries. PBF, on the other hand, provides builds with an extremely high resolution, so that they are suitable for applications involving parts with intricate cooling channels and very complex geometries, such as those used in biomedical, aerospace, and automobile applications.

Overall, both PBF and DED processes allow for the production of parts that have complex geometries, with each specific process providing unique advantages and disadvantages, which make them suitable for a variety of applications. In practice, the process used depends on factors such as the part geometry, build volume, required precision, and volume to be manufactured.

### 2.1.1 Laser Powder Bed Fusion

LPBF is a PBF technique that utilizes a high-power laser as a thermal energy source to selectively fuse metal powder. A typical LPBF setup is illustrated in **Figure 2.2**. The system consists of a powder chamber and a build chamber, both of which are purged with an inert gas, such as argon (Ar) or nitrogen (N), to minimize oxidation. The build chamber contains a build plate, onto which a recoater spreads a uniform layer of powder. A high-precision laser, guided by scanning mirrors and focused with the use of an optical lens, selectively melts the powder according to a predefined scanning path. Once a layer is completed, the build plate is lowered

by a predefined thickness, and fresh powder is dispensed from the powder reservoir. The recoater again spreads the new layer, and the laser carries out the next contour scan of the part. This process is repeated layer-by-layer from the bottom-up until the entire component is built, which is surrounded by unfused powder. When the process is completed, the part remains in the powder bed for cooling. Once cooled, the build is transferred to a depowdering station, where the excess powder is removed. The printed component is then removed from the build plate, typically by using a technique such as electrical discharge machining (EDM).

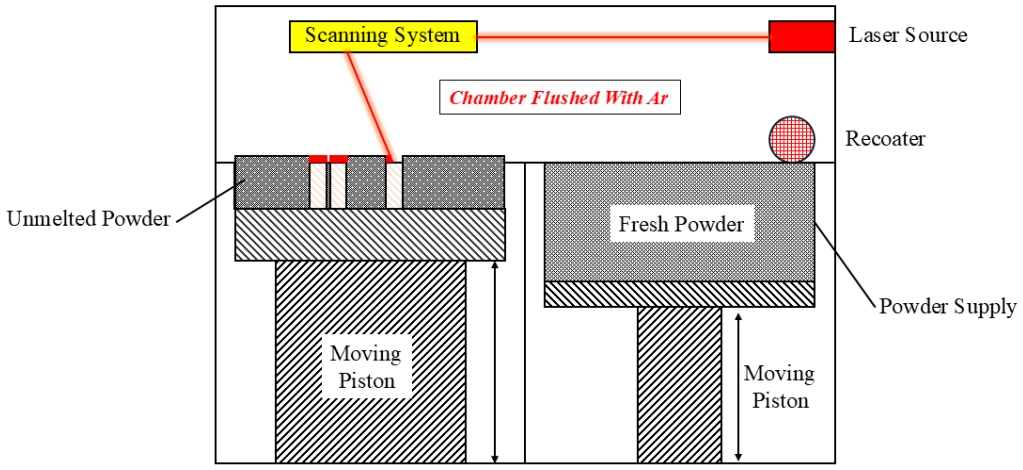



**Figure 2.2** Schematic of LPBF machine

The LPBF process is governed by a number of process parameters, the key ones being laser power, scanning speed, powder bed temperature, layer thickness, hatch distance, and scanning strategy [11], [12]. Since these parameters are crucial for ensuring high-quality builds, deviations from an optimal parameter combination can introduce significant manufacturing defects, thus ultimately compromising the mechanical performance of the part. Understanding the types of manufacturing defects that form and their underlying formation mechanisms is essential for optimizing the process. Some of the common manufacturing defects associated with LPBF are discussed in the following, including lack of fusion (LOF) and keyhole defects, balling, gas porosity, oxidation, loss of alloying elements, and cracking.

#### 2.1.1.1 Lack of Fusion Defects

LOF defects are among the most common manufacturing defects in LPBF, which are produced from insufficient melting of the powder bed [12]. The defects form when the energy input, for a given layer thickness and hatch distance, is too low to allow complete melting and interlayer fusion. Inadequate energy input prevents proper penetration of the melt pool [13] into the underlying layer, which results in weak metallurgical bonding [14]. LOF defects are typically large, which can range from a few micrometres to a few millimetres, and have a highly irregular morphology, including extremely sharp edges [15]. Usually, LOF defects are preferentially found at the melt track edges and impact the weld pool dynamics of the successive layers, which leads to increased formation of manufacturing defects [16]. Mukherjee et al. [13] proposed metrics such as the LOF index (given by the ratio of the weld pool depth to the layer thickness) that show a good correlation with the quantity of LOF defects within builds. Their results indicated that it is essential to choose a process recipe that provides appropriate weld pool depth and width to mitigate the formation of LOF defects.

#### 2.1.1.2 Keyhole Defects

Keyhole defects are large, near-circular pores that form in an LPBF build when LPBF is conducted at large energy inputs [17]. Some reports suggest that an excessive energy density leads to an interplay between vapor depression and melt pool dynamics, which then leads to Marangoni flow. When the Marangoni flow dominates the buoyancy, this can lead to keyhole defects [18]. Some in-situ observations identify three reasons for the formation of keyhole defects: 1. sudden changes in the laser path of the adopted scanning strategy, 2. abrupt shut off of the laser at the end of a weld track, and 3. instability of the vapor depression and weld pool dynamics at high energy densities [19]. However, some reports show that energy input is not

the only parameter to predict and quantify the formation of keyhole defects, and resort to parameters like normalized enthalpy and modified energy density to obtain a better physics-based explanation [20], [21]. Overall, recognizing the formation of keyhole defects, and their formation mechanism remains elusive and requires further investigation for a better understanding.

#### 2.1.1.3 Balling

Balling is a defect caused by the surface tension of the molten material during LBPF. Under certain conditions, the melt pool becomes too long and thin. The liquid metal then reaches a point of critical instability in which the melt pool minimizes its surface free energy by forming spherical droplets instead of a continuous and uniform track [22]. This discontinuous melt track has negative impacts on the adhesion of the layers and density of the resultant part. A number of investigations have shown that when the melt track reaches a certain point of becoming too long and thin, especially at high scanning speeds, Plateau-Rayleigh instability occurs. This instability is driven by the effects of the surface tension, which leads to balling [23], [24], [25]. Some precious metals have a high thermal conductivity and are generally resistant to Plateau-Rayleigh instability, but still show balling at high scanning speeds [26]. Gu and Shen [23] also indicated that in poorly packed powder beds, balling can occur at high scanning speeds and the use of a high power electron beam, irrespective of the material.

#### 2.1.1.4 Gas Porosity

Gas porosity is the most common type of weld porosity which is resultant of the entrapment of gas pores. These nearly spherical voids in LPBF builds are caused by trapped gas [27]. Their origin can either be linked to manufacturing defects inherent in the powder or process-induced entrapment during melting. Gas atomization that uses N or Ar can trap gas within the powder

particles, which then causes porosity in the final build [28]. Additionally, during laser scanning, vapor depression and melt pool dynamics can produced trapped gas bubbles due to rapid solidification [29]. While powder-induced porosity cannot be mitigated by adjusting the process parameters, process-induced porosity can be reduced by slowing down the scanning speed, which allows the gas bubbles to escape before solidification occurs [30].

#### 2.1.1.5 Oxidation

A critical aspect of an LPBF build is to maintain low levels of oxygen within the build chamber. High levels of oxygen can lead to oxidation. Even in small amounts, oxygen may be absorbed by the molten metal during the AM process, which leads to the formation of oxides such as aluminium oxide ($Al_2O_3$), chromium oxide ($Cr_2O_5$), and silicon dioxide ($SiO_2$). Alloying elements such as manganese (Mn), Si, and Al have high affinity to oxygen and can cause major problems in materials for example, Inconel 718, margining steel, and SS by affecting their ductility and strength [31], [32]. Sometimes, the powder surface may oxidize, which can interfere with the molten pool dynamics, thus leading to unstable flow, and the formation of other manufacturing defects such as balling and porosity. Over repeated thermal cycles, these oxides may also lead to the emergence of cracks, thus negatively affecting the material performance [33].

#### 2.1.1.6 Loss of Alloying Elements

In the LPBF process, materials are subjected to extreme temperatures, particularly beneath the laser spot, which often exceed their melting points and cause vaporization. This results in abnormal temperature gradients that can vaporize alloying elements, which leads to compositional variations between the powder and the as-built component. Studies have shown

that elements tend to deplete at lower vaporization temperatures but become enriched at higher vaporization temperatures, which can potentially change the final properties of the material [34], [35].

#### 2.1.1.7 Cracking

The LPBF process exposes materials to extreme thermal cycles at rapid heating and cooling rates (~$10^6$ K/s), which leads to high residual stress and potential cracking. The two primary cracking mechanisms are solidification and liquation cracking [12]. Solidification cracking occurs in the fusion zone during the final stages of solidification when the interdendritic liquid in the mushy zone fails under shrinkage stress, thus resulting in cracks that propagate across multiple melt pools [36]. This issue is exacerbated in alloys with a wide solidification range and poor grain boundary wetting. Liquation cracking, on the other hand, occurs in the heat-affected zone (HAZ), where partial melting can occur due to subsequent laser passes. Alloys prone to low-melting eutectic phase formation, such as high-strength steels and nickel-based superalloys, experience liquation cracking as thin liquid films that lack mechanical integrity form and tear apart under residual tensile stresses [37], [38]. The presence of impurities such as sulfur, phosphorus, and carbon can further promote this failure. To mitigate the impact of these defects, strategies such as preheating and optimized scanning strategies are employed to control thermal gradients and reduce stress accumulation. Proper selection of alloy composition and processing parameters is essential for minimizing cracking and ensuring high-quality LPBF components.

Overall, a number of manufacturing defects form during the LPBF process, and a significant factor that influences the formation of manufacturing defects is improper selection of the process parameters. Therefore, it is essential to understand how process parameters and their

interaction affect the formation of microstructural manufacturing defects during the LPBF process.

### 2.1.2 Influence of Process Parameters on Formation of Manufacturing Defects

The following is a review of the literature that addresses how various process parameters influence the formation of manufacturing defects during the LPBF process, including laser power and scanning speed, hatch distance and layer thickness, scanning strategy and powder bed preheating.

#### 2.1.2.1 Laser Power and Scanning Speed

The laser scanning speed (v) and laser power (P) are two crucial parameters for creating defect-free builds and often examined together by using a single parameter called volumetric energy density (VED). The VED is obtained by:

$$VED = \frac{P}{vht} \tag{1}$$

where h is the hatch distance and t is the layer thickness. It is common practice to use constants h and t and focus on the effects of P and v to understand the solidification process and cooling rate found within a given scan. In such a case, VED is simplified to linear energy density (LED) as follows:

$$LED = \frac{P}{v} \tag{2}$$

LED is a crucial parameter that influences the weld pool characteristics, cooling rate, and thermal cycles of the material in the primary solidification scan [39], [40] and subsequent scans. Hence, understanding the effects of laser power and scanning speed on the formation of

manufacturing defects by using LED has become an accepted practice in the literature on LPBF.

When the laser power is low and scanning speed is higher than required, the build is executed in a low-energy-density regime. Within this window, the cooling rates are the highest, and amount of molten metal is the lowest [41]. Such conditions may lead to the LOF defects owing to less material melting and improper fusion with the base metal [21], [42], [43]. The LOF defects are commonly due to unmelted powder, which can further negatively impact successive scans. In general, the materials that have a lower thermal conductivity are more susceptible to the formation of LOF defects since for the same energy density, less metal is melted compared to a metal with higher thermal conductivity. Mukherjee et al. [41] numerically examined this phenomenon, and showed that with the same laser power and scanning speed, 316 SS has gaps within successive scans, while Al Si10Mg shows no gaps.

Another common issue that results from a high scanning speed and lower laser power is balling. Since the onset of balling involves unstable melt pool conditions in which the melt pool becomes substantially longer, it is more prevalent at high scanning speeds. However, the appropriate laser power level for balling varies from material to material. For most engineering materials, balling is more prevalent at low laser power and high scanning speed conditions; however, for noble metals like gold, balling has also been found in high power builds [22], [44].

In builds produced at low scanning speeds and high laser power conditions, there is enhanced weld pool penetration into the base material because of the vapour pressure of the metal which evaporates under the beam [20]. This abnormally deep melt pool is subjected to complex fluid flows and fluctuations. These fluctuations can lead to gas bubbles that are “pinched off” into the molten metal, where fluid forces of buoyancy (which tend to push the bubbles up) and

Marangoni flow forces (which tend to push the bubbles down) compete. If the Marangoni forces dominate, the bubbles are unable to escape, and a large circular defect is retained in the solidified metal [43]. These fluctuations increase when the laser scan path changes abruptly; hence, the laser power and scanning speed, despite being important parameters, cannot be used to describe the formation of keyhole defects [18], [25], [35].

Overall, the role of laser power and scanning speed in the formation of manufacturing defects is summarized in **Figure 2.3**. Low laser power and high scanning speeds leave the build susceptible to LOF defects, which affect the thermal conductivity of the material. High scanning speeds tend to produce long weld pools that are not stable which lead to balling. The effect is more prominent at low laser power, but may also be seen at high laser power. Lastly, when the scanning speed is low and laser power is high, keyhole defects, governed by the fluid flow within the weld pool, become prevalent. These limitations guide research work in determining an optimal range for energy density, which would result in near-zero manufacturing defects. This range can be manipulated by changing other variables, but the optimization of laser power and scanning speed through energy density remains a crucial aspect of reducing manufacturing defects with LPBF-produced materials.

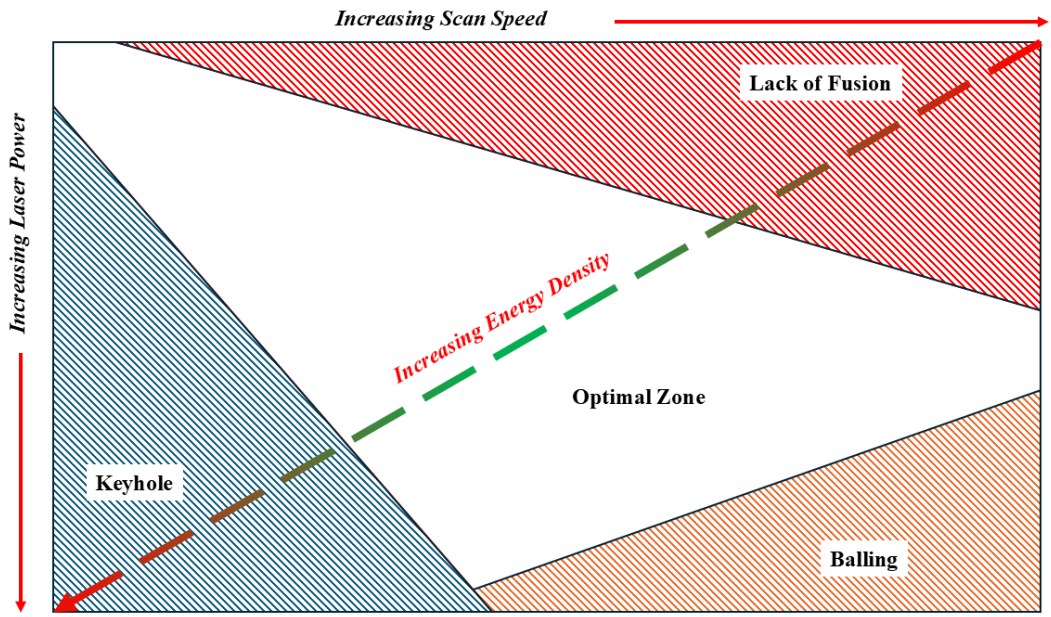



**Figure 2.3** Schematic process map with laser power and scanning speed

### 2.1.2.2 Hatch Distance and Layer Thickness

The hatch distance is defined as the distance between two neighbouring scanning paths during LPBF, while the layer thickness refers to the thickness of the layer of powder particles spread in the scanning of a given shape. Both variables do not influence the primary scan, although they may significantly affect the subsequent thermal cycles, and impose the material to a complex thermal history. Both parameters also have the potential to manipulate the working LED range and change the laser power and scanning speed requirements to obtain good-quality builds. Therefore, an understanding of how the working "LED" range is affected by the hatch distance and layer thickness is crucial.

Mansouri et al.[45] reported that hatch distance does not significantly influence the density of the final build-up up to a certain threshold that is system-dependent. Beyond this threshold, a marked decrease in density has been observed experimentally by Hu et al. [46] and Wang et al. [47]. These experimental findings are further supported by a physics-based 3D transient heat and fluid flow model developed by Mukherjee et al. [41], which was applied to various material

systems. Overall, the literature suggests that materials with higher thermal conductivity, such as AlSi10Mg, are less susceptible to defect formation with increasing hatch distance. In contrast, materials with lower thermal conductivity are more prone to such manufacturing defects, which would require the use of smaller hatch distances to achieve defect-free builds.

The effect of the layer thickness on the defect contents in LPBF shows a monotonic trend. As the layer thickness decreases, the material quality increases. Liu et al. [48] showed that thinner layers enhance fusion with better mechanical performance by mitigating LOF defects, but after a certain point, microstructural aspects dominate, which result in a poor performance. Hyer and Petrie [49] observed that while densification decreases slightly with thicker layers, the printed material remains mostly robust. Both low and high-layer thicknesses can erode mechanical performance, with the latter being more detrimental due to poor fusion and stress concentration in LOF defects [50]. Therefore, there is an optimal layer thickness that balances the defect content and mechanical properties.

#### 2.1.2.3 Laser Scanning Strategy

The laser scanning strategy is the specific path that a laser follows during the layer-by-layer fabrication process in LPBF. This strategy plays a critical role in determining the thermal history of the build, as it directly influences the cooling rate and the number and characteristics of thermal cycles. Variations in scanning patterns can lead to differences in manufacturing defects, microstructural changes, residual stress distribution, and ultimately, the mechanical properties of the final component. For instance, strategies such as unidirectional scanning, using chessboard patterns, or stripe scanning can result in different temperature gradients and solidification dynamics. Some of the most commonly employed scanning strategies are illustrated in **Figure 2.4**, including stripe, chessboard and hexagon scanning strategies.

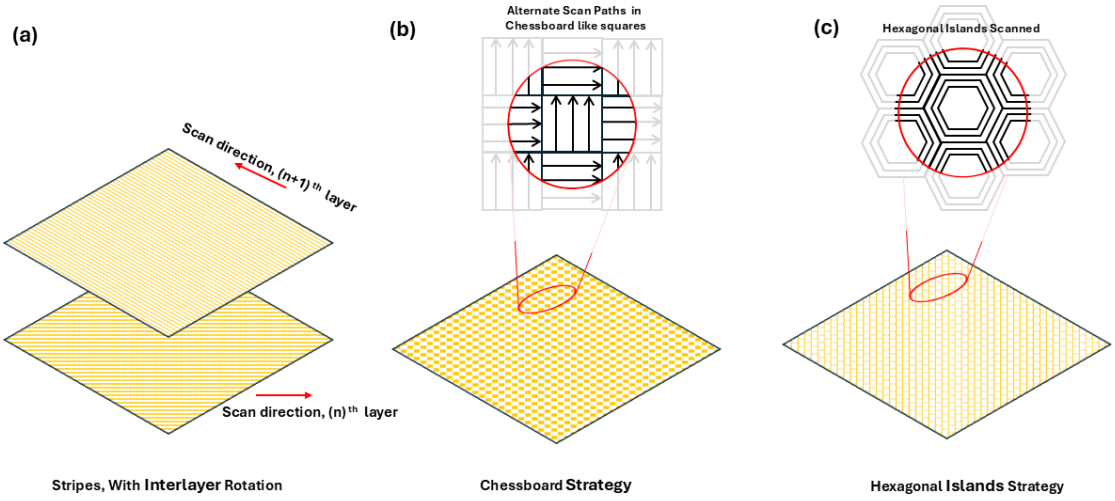



**Figure 2.4** Schematic representation of (a) stripe, (b) chessboard, and (c) hexagonal scanning strategies

It has been reported that increasing the complexity of the scanning strategy can lead to a slight increase in the formation of manufacturing defects. Wu et al. [51] observed that a simple linear scanning strategy results in samples with the highest densification, whereas more complex strategies are associated with higher gas porosity. Similarly, Chen et al. [52] showed that a linear scanning strategy that incorporates alternating scanning directions between adjacent tracks can contribute to the mitigation of balling defects. In contrast, more intricate strategies such as island scanning or chessboard scanning strategies tend to produce a higher fraction of manufacturing defects. Overall, the literature suggests that simpler scanning strategies are generally more effective in minimizing the formation of manufacturing defects during the LPBF process.

### 2.1.2.4 Powder Bed Preheating

Preheating the build plate has been shown to play a crucial role in influencing the melt pool dynamics and defect formation during LPBF across various alloy systems. Qin et al. [53]

showed that higher preheating temperatures of tool steels lower the required energy density, as additional heat from the preheated powder bed contributes to melting the powder. This preheating also enhances thermal conductivity, which results in a smoother temperature gradient and more stable thermal profiles. Similarly, Caprio et al. [54] reported that in titanium (Ti) alloys, preheating is effective in mitigating solidification cracking and porosity; however, this improvement comes at the expense of the mechanical properties, as elevated preheating temperatures can result in significantly softer samples due to changes in other microstructural features. Chen et al. [55] examined IN718 by using single-track experiments, and highlighted how preheating influences different melting regimes—the conduction, transition, and keyhole modes. Enhanced thermal conductivity at higher preheating temperatures leads to smoother gradients, lower cooling rates, and more powder melting in the conduction mode. In the transition mode, a combination of heat conduction and vapor depression yields wider and deeper melt pools. In the keyhole mode which mostly causes vapor depression, preheating leads to abnormally deep penetrations, which shows the complex interplay between thermal and physical phenomena. The findings are summarized schematically in **Figure 2.5**.

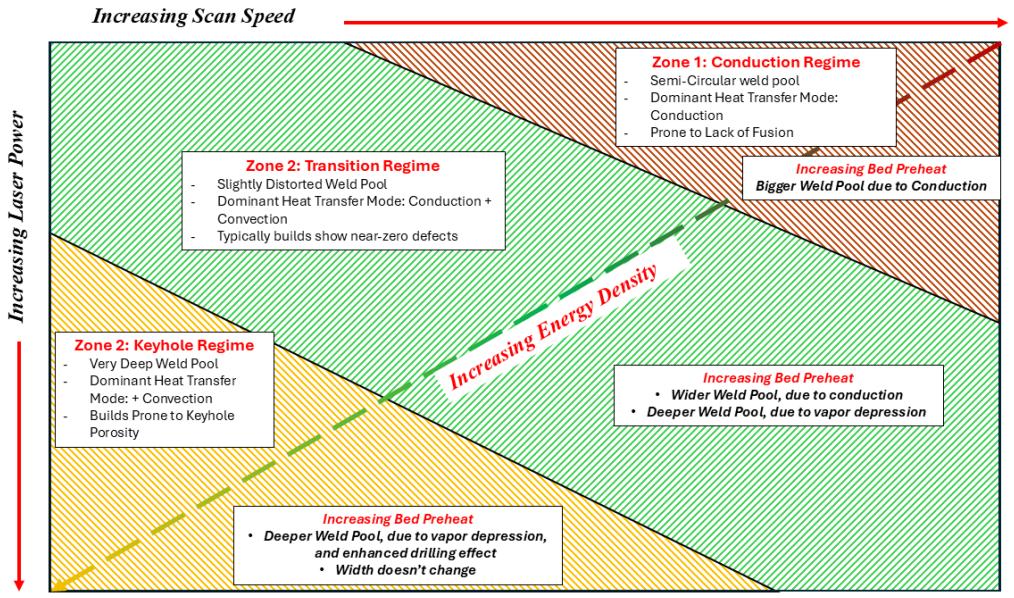



**Figure 2.5** Schematic of effect of powder bed preheating on LPBF process

## 2.2 LPBF of 17-4 PH SS

The 17-4 PH SS is one of the most widely utilized PH SSs since its emergence. Its widespread adoption is attributed to an exceptional combination of mechanical strength and corrosion resistance, which is why it is a preferred material for demanding applications such as aerospace components, biomedical implants, fasteners, and structural parts in the oil and gas industry [56]. The corrosion resistance of 17-4 PH SS primarily stems from its chromium and nickel contents [28], while its high strength and hardness are achieved through a two-step precipitation hardening heat treatment, which facilitates the formation of nano-scale copper precipitates in a martensitic matrix.

The 17-4 PH SS typically has a martensitic microstructure. However, its martensitic finishing temperature ($M_f$; ~ 32°C) is close to room temperature, so that 17-4 PH SS is sensitive to phase changes caused by minor compositional changes [57]. The strength of 17-4 PH SS is further enhanced through PH heat treatment, which relies on the formation of nano-scale copper precipitates in the martensite phase [58]. Hence, before any precipitates form, ageing a solution

treatment of 1050ºC for 30 to 60 mins is necessary. This condition is referred to as "Condition A" and responsible for creating a fully martensitic microstructure. Aging heat treatments slightly differ depending on the application and properties desired, but the heat treatment for H900, i.e. ageing for 1 hr at 482ºC, is by far the most common heating treatment, which provides peak aging [59].

The LPBF process imposes thermal cycles onto a material that is not used with other methods, which could result in highly varying mechanical properties. These thermal cycles can significantly affect the mechanical properties of the as-built component. For a material such as the 17-4 PH SS, even slight variations in its composition and thermal cycles can produce a scattered phase and defect content [6], [60]. Therefore, it is necessary to investigate the process variables that influence these microstructural features. Thus, 17-4 PH SS has received much research attention and is one of the most researched materials for LPBF [2], [4], [6], [8], [12], [53], [61], [62], [63], [64], [65]. The following sections describes some of these efforts.

### 2.2.1 Influence of Various Process Parameters on the As-built Condition

The literature often reports on the scattered mechanical behaviour of 17-4 PH SS. These variations are attributed to microstructural features such as manufacturing defects and phase composition. Some common process variables that affect the microstructure and mechanical behaviour of 17-4 PH SS are discussed below.

#### 2.2.1.1 Powder Characteristics

Two types of powder are commonly used in LPBF applications, namely, water and gas atomized powders. The former has a highly irregular shape, while the latter is spherical. Gas atomized powder is better for achieving full densification within 17-4 PH SS compared to

water-atomized powder [66]. Furthermore, the defect content with the use of gas atomized powder is affected by the powder size distribution. Even though the average powder particle size does not affect the defect content very much [67], the sharpness of the distribution in simulations can affect defect formation, with a sharper distribution corresponding to better characteristics [68]. Another unique problem with the 17-4 PH SS is that when a nitrogen-atomized powder is used, the martensitic finishing temperature might be reduced, as N is an austenite stabilizer in steels [69] and absorbed within the material. This leads to a significant amount of retained austenite, and the as-built material behaves similarly to transformation-induced plasticity (TRIP) steels [70].

#### 2.2.1.2 Effect of Parameters Affecting Energy Density

It is possible to find an optimal energy density window for producing nearly fully dense parts. However, as-built parts may not have a similar microstructure, which results in variations in the mechanical properties. Hsu et al. [71] investigated the effect of varying energy densities on the martensitic fractions in 17-4 PH SS. They found that martensitic fractions in the as-built components increase with increasing energy density, which is attributed to increased residual stresses associated with higher energy densities through finite element simulations. The hatch distance negatively affects the martensitic fraction, thus promoting austenite reversion due to increased overlapping at smaller hatch distances. Hu et al. [46], however, investigated the effect of energy density manipulation (via changing the laser scanning speed and hatch distance) on defect formation. They found an optimal energy density range where good densification is observed, and this change in densification characteristics is attributed to the manipulation of the melt pool geometry. Yasa et al. [72] followed a similar approach to manipulating the laser power, scanning speed, and hatch distance. A wide scatter plot of the mechanical properties based on a static tensile test indicated that some samples even show a “double-yielding” effect

attributed to the strain-induced transformation that occurs due to excessive retained austenite. Makoana et al. [73] investigated how the beam diameter can be used to manipulate the power-speed process map, by manipulating the ideal energy density range. A larger beam diameter promotes stability in the optimal range, which allows for production at higher scanning speeds and thus reduces the build time. However, an overly high scanning speed leads to significant spatter and could be detrimental for the final product [73]. Sarker et al. [74] investigated the influence of pore formation on the tensile properties of samples prepared at various energy densities. The sample printed at a higher energy density shows both better strength and ductility; however, the phase composition is similar in all of the cases, which are fully martensitic. This isolates the effect of manufacturing defects and the resulting variation in mechanical performance is believed to be affected by manufacturing defects only.

Overall, the studies in the literature clearly report that energy density is a critical parameter that affects both the defect content and phase composition in the as-built condition. Printing within an optimal energy density range is crucial for obtaining defect-free builds, but other parameters also influence the workable energy density range to varying extents. The effects of the LED combined with other parameters can lead to inconsistent phase compositions and many manufacturing defects, which result in unpredictable mechanical behaviour in the as-built state. This requires a better understanding of the variables that affect the energy density range in the as-built condition.

#### 2.2.1.3 Laser Scanning Strategy

The scanning strategy is an LPBF process parameter that does not directly affect the cooling rate for the primary solidification scan, but can play a significant role in subsequent temperature-time cycles [75]. Various scanning strategies have shown different effects on the as-built 17-4 PH SS, which influence both the phases and defects that can form. Rashid et al.

[76] investigated the effect of double scanning on a 90-rotation scanning strategy on manufacturing defects and retained austenite in as-built material. Double scanning leads to higher densification, while the amount of retained austenite is unaffected. Asapu et al. [64] compared the hexagonal and chessboard scanning strategies. The former leads to higher densification, while, the latter showed less residual stress. No significant difference in the phases is reported, and the samples successfully responded to the commercial heat treatment by producing copper precipitates. Lashgari et al. [77] revealed that a hexagonal scanning pattern is superior to a concentric scanning pattern with fewer manufacturing defects which is attributed to a wider weld pool due to a slower cooling rate in the as-built state. Even the amount of retained austenite is reported to be less than that in the concentric pattern which results in a harder material. Kartikeya Sarma et al. [78] first compared three scanning strategies, namely the hexagonal, strip, and rectangular scanning strategies, and determined that the hexagonal scanning strategy leads to better results by minimizing the austenite fraction, which is also found in other studies [79], [80]. In their subsequent work, Kartikeya Sarma et al.[81] optimized the size of the "hexagonal islands" used and reported that the as-built hardness varies with austenite fraction in the as-built state, and nearly doubles if a large island size is used.

The studies in the literature have consistently found that scanning strategy can affect both manufacturing defects and the phases by manipulating the thermal cycles to which the material is exposed. The hexagonal scanning strategy has provided the best results for densification, and reduces the retained austenite, yet variables like the island size can still produce samples with a high austenitic fraction. Further work is required to minimize these effects, thus enabling the production of a microstructurally consistent mechanism for the as-built condition.

#### 2.2.1.4 Powder Bed Preheating

Printing at elevated powder bed temperatures has shown potential in controlling the extremely rapid cooling rates of the LPBF process and improving the printability of alloys such as Ti-6Al-4V [40], and high-speed alloy steels, like AISI M50 [61]. However, its impact on 17-4 PH SS remains largely unexplored. Understanding how the powder bed temperature influences the microstructure and mechanical properties of 17-4 PH SS can provide valuable insights into the optimization of the process parameters and enhancement of the reliability of the printed components.

### 2.2.2 Effect of Heat Treatment

The mechanical strength of 17-4 PH SS is derived from a two-stage heat treatment process that involves a solution treatment followed by ageing. This heat treatment induces the formation of nanoscale copper precipitates within the martensitic matrix, which greatly enhances the material strength and hardness. The initial solution treatment, which is commonly referred to as Condition A, results in a predominantly martensitic microstructure along with a supersaturated solid solution of copper. Upon ageing, these copper atoms precipitate out, which contributes to precipitation strengthening.

The standard heat treatment cycles used to produce the different types of properties in 17-4 PH SS are illustrated in **Figure 2.6**. The first step involves solution heat treatment at approximately 1040°C for one hour, during which a single-phase austenitic solid solution is formed, with the copper fully dissolved in the matrix. This austenite is then rapidly quenched, which results in a predominantly martensitic microstructure with supersaturated copper. In this Condition A, the material is relatively soft and machinable, and often supplied in this form for ease of manufacturing. The second step involves ageing, which promotes the formation of copper-rich precipitates that enhance strength; however, the specific ageing temperature and time are

tailored based on the desired application. The most commonly used heat treatment is H900, which is known for achieving peak strength. In this condition, coherent body-centered cubic (BCC) copper clusters form and strengthen the matrix primarily through a shearing mechanism [57]. When more toughness is required, ageing treatments such as H1125 or H1150 are employed. In these cases, the copper precipitates coarsen into face-centered cubic (FCC) structures and become semi-coherent or incoherent with the matrix, which results in slightly lower strength, but higher ductility and toughness than H900.

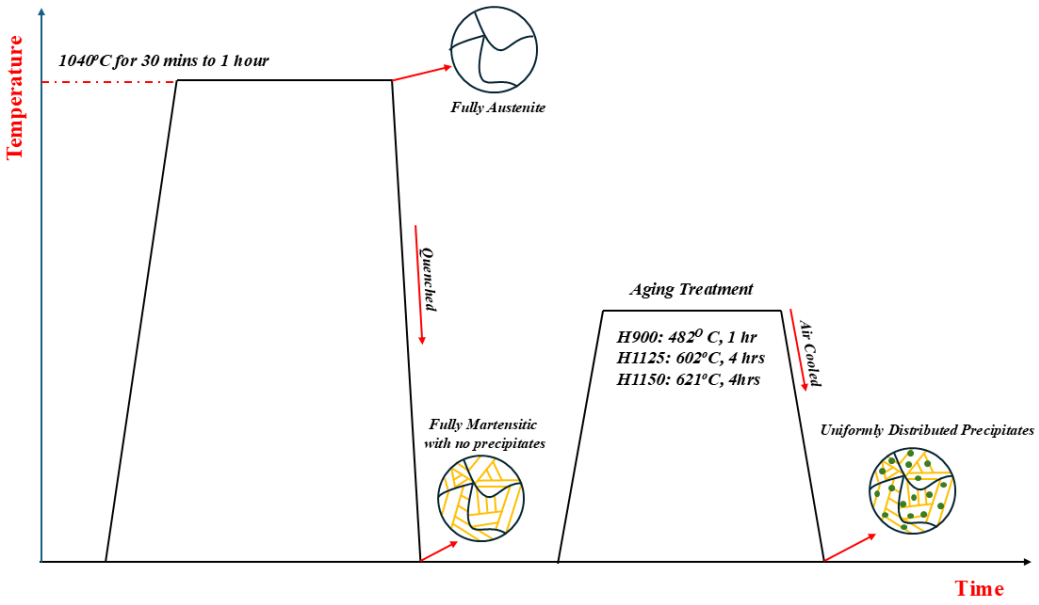



**Figure 2.6** Standard heat treatment cycles for precipitation hardening of 17-4 PH SS

LPBF-processed 17-4 PH SS often has unpredictable responses to standard heat treatment protocols and underperforms relative to the expected properties of the alloy, which make it unsuitable for industrial applications. One of the initially reported concerns is the inadequate strengthening following heat treatment, primarily due to the absence of copper precipitates post-ageing [7]. This deficiency has been linked to an increased N content post-printing, which results from the uptake of N during the process. This significantly lowers the $M_f$ to below room temperature. Consequently, after solution annealing (Condition A), the alloy retains a

substantial fraction of austenite, thereby suppressing the precipitation of copper during the ageing step [8].

In addition to N enrichment, other factors that contribute to the reduction in $M_f$ include variations in powder chemistry [82], [83] and the use of N during powder atomization [65], [84]. To address these challenges and promote the formation of a fully martensitic microstructure before ageing, several strategies have been explored. Shuai et al. [85] carried out cryogenic treatment, which is typically done with liquid nitrogen after Condition A to achieve complete martensitic transformation. Yeon et al. [7] introduced a normalizing heat treatment prior to Condition A, which has been shown to facilitate the subsequent formation of copper precipitates. A widely adopted preventative measure involves the use of Ar instead of N during both powder atomization and the LPBF process, thus effectively minimizing the uptake of N and thereby enhancing the response of the alloy to the heat treatment [5], [65], [86].

Despite these efforts and the successful induction of copper precipitates, LPBF-manufactured 17-4 PH SS still often fails to meet the minimum mechanical property requirements for industrial applications, thus indicating the need for further optimization through both processing and post-processing routes.

**Figure 2.7** presents the tensile properties of 17-4 PH SS samples produced by using an "optimized recipe" of the LPBF process parameters, followed by a conventional heat treatment with Condition A + H900, which are compared to the standard property requirements outlined in ASTM A693-24 [87]. While many studies report achieving the target strength, primarily due to successful copper precipitation, a significant scatter in ductility is observed. In most cases, the values of the ductility fall short of industrial expectations. Notably, analyses of the fractured surface of low-ductility samples often reveal the presence of unmelted powder particles (

**Figure 2.8(c)** and **2.8(d)**), which suggests that processing-induced defects play a dominant role in limiting performance. These observations underscore the need for process optimization strategies that extend beyond the current approach. A more targeted and process-driven approach, which aims to mitigate the formation of manufacturing defects during LPBF, is essential to unlocking the full potential of 17-4 PH SS for critical applications.

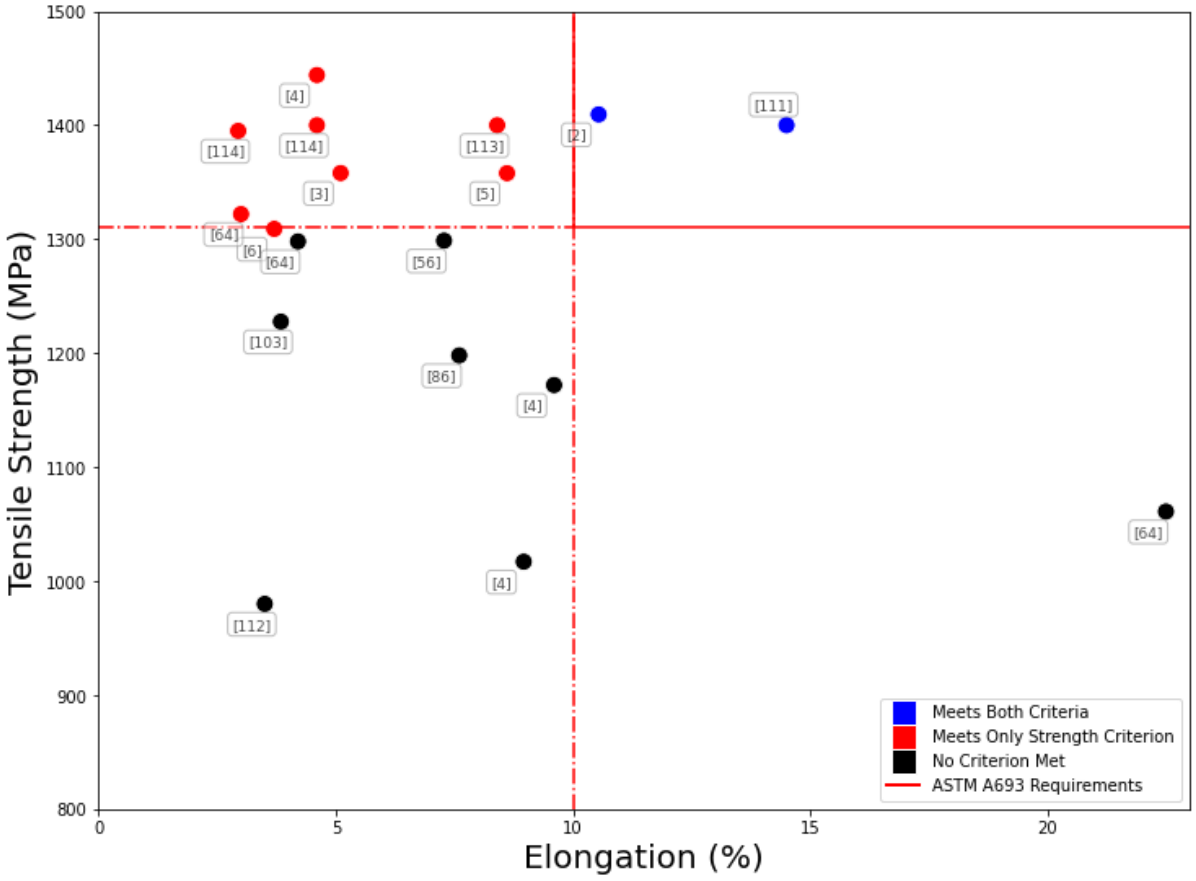



**Figure 2.7** Mechanical properties of 17-4 PH SS produced through LPBF, after heat treatment (Condition A + H900) based on literature compared to ASTM A693 [87]

**Figure not included due to copyright restrictions.**

**See References [6] and [88] for original image.**

**Figure 2.8** Fractured surfaces of tensile test samples produced in optimized window as reported by (a, c) Kovacs et al. [6] , and (b, d) Mahmoudi et al. [88] at lower and higher magnifications which reveal unmelted powder *(image not shown due to copyright restrictions)*

## 2.3 Summary and Research Gap

In recent years, AM has emerged as a viable alternative to conventional manufacturing methods by overcoming geometric constraints and enabling the fabrication of highly complex designs. Among the latest advancements in AM, LPBF is distinct due to its ability to produce components with exceptional resolution and precision. However, the LPBF process subjects materials to rapid thermal cycling and extremely high cooling rates, which can result in unpredictable material behaviour. This is primarily due to the formation of microscopic manufacturing defects and inconsistent phase compositions resultant of the complex thermal history inherent to the process.

The complex thermal cycling inherent to the LPBF process, which governs both defect formation and phase changes, is strongly influenced by key process parameters such as the laser power, scanning speed, hatch spacing, and layer thickness. Among these, the combination of laser power and scanning speed is often optimized through an LED framework, which provides a useful window for achieving consistent melt quality. An LED that is too low typically results in insufficient melting of the powder, which leads to LOF defects and balling. Conversely, excessively high LED values can cause keyhole defects due to instability of the vapor-driven melt pool. Parameters such as hatch spacing can be adjusted to mitigate LOF; for instance, reducing the hatch distance promotes more overlap between the scanning tracks, thereby reducing the likelihood of unmolten regions. However, this improvement often comes at the expense of increased build time and energy consumption. One process parameter that has shown promise in broadening the optimal processing window is build plate preheating. By

increasing the initial substrate temperature, powder bed preheating can effectively control the cooling rates, reduce thermal gradients, and inhibit the formation of manufacturing defects, particularly LOF, thus enhancing the overall quality of the part.

The 17-4 PH SS is a PH alloy widely employed in aerospace, automotive, and biomedical applications due to its excellent combination of corrosion resistance and high mechanical strength following appropriate heat treatment. Its inherent weldability makes it a suitable candidate for LPBF. However, the material exhibits high sensitivity to variations in process parameters, which can lead to the formation of manufacturing defects and phase inconsistencies, thus ultimately resulting in unpredictable mechanical properties. One of the early challenges in the LPBF processing of 17-4 PH SS was the lack of precipitation hardening after heat treatment, which was initially believed to be the result of suppressing copper precipitation due to austenite retention. Recent studies [3], [84][65] have addressed this issue by optimizing the processing conditions, including the use of inert atmospheres such as Ar, which minimize interference with the precipitation process. While these approaches have led to improved strength, the material still frequently fails to meet mechanical property requirements, primarily due to unpredictable ductility. Fractographic analyses have revealed the presence of unmelted powder particles even in samples that exhibit adequate strength post-heat treatment, thus suggesting that persistent manufacturing defects continue to limit performance. Enhanced powder bed preheating has been used successfully to eliminate such manufacturing defects in many tool steels and Ti-alloys, but remains an unexplored avenue for enhancing the performance of LPBF-manufactured 17-4 PH SS.

As can be seen, the LPBF of 17-4 PH SS is complicated, making it difficult to produce components that result in suitable mechanical performance. Therefore, this research conducts a comprehensive investigation into the influence of the process parameters, particularly build plate preheating, on the formation of manufacturing defects and the resulting mechanical

properties of LPBF-manufactured 17-4 PH SS. Additionally, the phase composition is systematically quantified in both the as-built and heat-treated conditions to evaluate how the process parameters influence phase changes and the response of the alloy to heat treatment. The mechanical performance is then evaluated against standard property benchmarks to determine the effectiveness of preheating in enhancing the overall quality and reliability of the material.

# Chapter 3: Materials and Methodology

This chapter outlines the experimental methodology employed in this study. First, the overall experimental workflow is presented, followed by a detailed description of the procedures used to produce the test specimens. The subsequent sections cover the method adopted for quantifying the manufacturing defects, characterizing and quantifying the phases, and mechanical testing.

## 3.1 Experimental Plan

The objective of this study is to investigate the influence of key process parameters on the mechanical properties of LPBF-manufactured 17-4 PH SS, with a focus on the formation of manufacturing defects and phase changes. Additionally, the study evaluates whether the alloy, after appropriate heat treatment, meets the mechanical property requirements for industrial applications. The samples were fabricated by using different combinations of laser power, scanning speed, and build plate preheating temperatures to enable systematic quantification of the manufacturing defects and characterization of the phases. Based on the observed defect levels, the process parameter combinations were then categorized into three groups, namely, best, intermediate, and poor. For recipes classified as “best”, a phase analysis was carried out for both the as-built and heat-treated conditions to evaluate the phase changes. Representative recipes from each category were then selected for fabricating tensile specimens in both conditions. Finally, the mechanical properties obtained were compared against standard specification requirements for 17-4 PH SS.

## 3.2 Production of Test Materials

This section outlines the procedures used to prepare the test materials used in the study. The steps include characterization of the feedstock powder, fabrication of specimens via LPBF, and the subsequent heat treatments applied. The experimental details are provided in the following.

### 3.2.1 Powder Characterization

Commercially available 17-4 PH SS powder was used to produce the specimens. The powder was characterized for particle size distribution and morphology by using scanning electron microscopy (SEM). The measured particle size distribution revealed D10 = 11.4 μm, D50 = 18.07 μm, and D90 = 30.43 μm, as shown in **Figure 3**.1**(a)**. The powder morphology is predominantly spherical in shape with the presence of some satellite particles, as shown in **Figure 3.1(b)**. The chemical composition of the powder is summarized in **Table 3.1**.

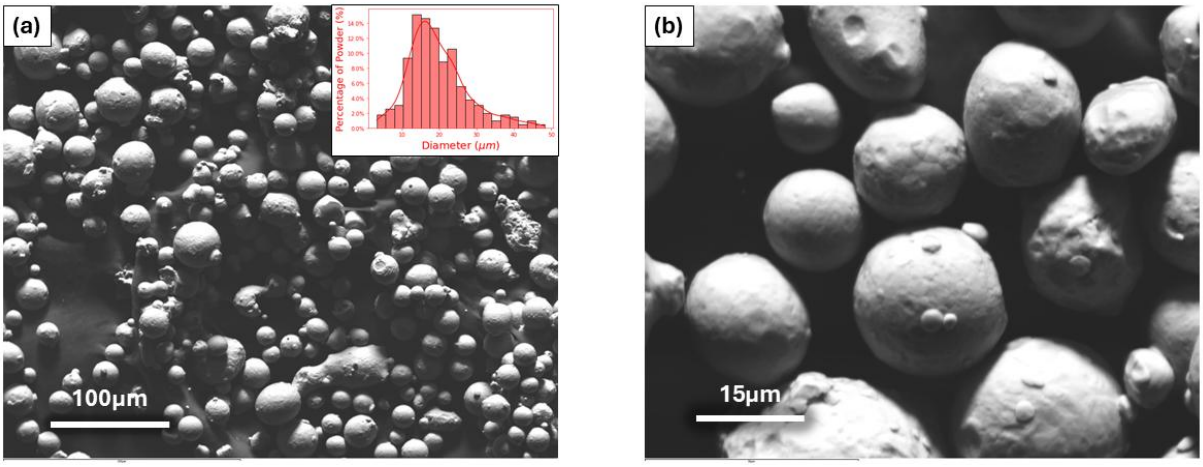



**Figure 3.1** SEM image of 17-4 H SS powder at (a) lower magnification with size distribution, and (b) high magnification showing some satellite particles

**Table 3.1** Chemical composition of powder used for printing 17-4 PH SS

| ***Element*** | **Fe** | **Cr** | **Ni** | **Cu** | **Mn** | **Si** | **C** |
|---|---|---|---|---|---|---|---|
| ***Weight percentage (%)*** | 74.27 | 16.14 | 4.87 | 3.51 | 0.16 | 0.55 | 0.04 |

### 3.2.2 Printing of Specimens

The samples were fabricated by using a TruPrint 5000 3D printing system (Trumpf) equipped with three 500 W fiber lasers and a preheatable tool steel build plate capable of reaching up to 500°C. The system offers an effective build volume of 290 mm in diameter and 400 mm in height. Fabrication was carried out in an inert Ar atmosphere with oxygen levels maintained below 0.01% to prevent oxidation and ensure a high-quality build environment. Following fabrication, the build plate and samples were allowed to cool naturally in the machine. The build plate was then transferred to a depowdering station, where the loose, unmelted powder was removed and collected for recycling through a sieving station. The parts, still attached to the build plate, were subsequently separated by using EDM. **Figure 3.2 (a) to 3.2(c)** show the LPBF setup and described post-processing workflow.

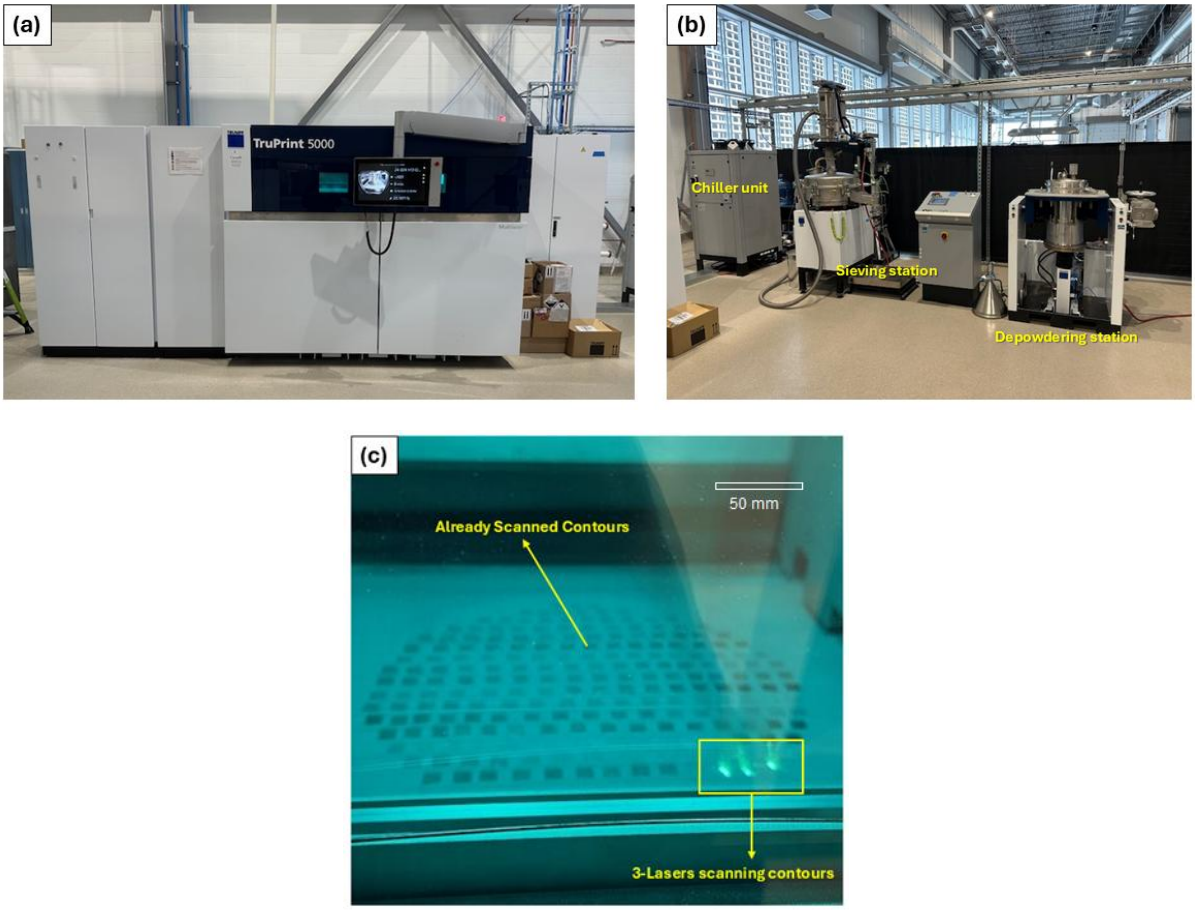



**Figure 3.2** Images of printing setup: (a) main printer, (b) supporting stations, and (c) an in-process image

The process parameters investigated in this study are laser power (150–300 W), laser scanning speed (600–1600 mm/s), and build plate preheating temperature (200–500°C). **Table 3.2** summarizes the complete set of 96 process parameter combinations (referred to as "recipes") explored. All of the other process parameters were held constant throughout the study, which included powder layer thickness of 40 µm, hatch spacing of 80 µm, laser spot size of 80 µm, and a stripe scanning strategy with a 51° rotation between successive layers. For each recipe, five samples were fabricated in the form of cuboids with dimensions of 10 × 10 × 20 mm (see **Figure 3.3(a)**) for all the process recipes listed in **Table 3.2** to enable microstructural characterization and defect quantification. Three of the five samples were used in the as-built condition, while the remaining two were subjected to a heat treatment followed by subsequent microstructural characterization.

**Table 3.2** Recipes used for process parameter investigation of 17-4PH SS

| Sample ID | Laser Power | Laser Scanning Speed | Powder Bed Preheating Temperature |
|---|---|---|---|
| - | *W* | *mm/s* | *Deg. C* |
| 1 to 5 | 150 | 1600 | 200, 300, 400, 500 |
| 11 to 15 | 150 | 1400 | 200, 300, 400, 500 |
| 21 to 25 | 150 | 1200 | 200, 300, 400, 500 |
| 31 to 35 | 150 | 1000 | 200, 300, 400, 500 |
| 41 to 45 | 150 | 800 | 200, 300, 400, 500 |
| 51 to 55 | 150 | 600 | 200, 300, 400, 500 |
| 61 to 65 | 200 | 1600 | 200, 300, 400, 500 |
| 71 to 75 | 200 | 1400 | 200, 300, 400, 500 |
| 81 to 85 | 200 | 1200 | 200, 300, 400, 500 |
| 91 to 95 | 200 | 1000 | 200, 300, 400, 500 |
| 101 to 105 | 200 | 800 | 200, 300, 400, 500 |
| 111 to 115 | 200 | 600 | 200, 300, 400, 500 |
| 121 to 125 | 250 | 1600 | 200, 300, 400, 500 |
| 131 to 135 | 250 | 1400 | 200, 300, 400, 500 |
| 141 to 145 | 250 | 1200 | 200, 300, 400, 500 |
| 151 to 155 | 250 | 1000 | 200, 300, 400, 500 |
| 161 to 165 | 250 | 800 | 200, 300, 400, 500 |
| 171 to 175 | 250 | 600 | 200, 300, 400, 500 |
| 181 to 185 | 300 | 1600 | 200, 300, 400, 500 |
| 191 to 195 | 300 | 1400 | 200, 300, 400, 500 |
| 201 to 205 | 300 | 1200 | 200, 300, 400, 500 |

| | | | |
|---|---|---|---|
| 211 to 215 | 300 | 1000 | 200, 300, 400, 500 |
| 221 to 225 | 300 | 800 | 200, 300, 400, 500 |
| 231 to 235 | 300 | 600 | 200, 300, 400, 500 |

A second iteration of builds was carried out for tensile testing. Based on the results of the defect quantification, the recipes were categorized into three groups: best (<0.5 % defect fraction), intermediate (0.5% to 5% defect fraction), and poor (> 5% defect fraction), and representative recipes from each category were then selected to fabricate larger blocks that measured 78 × 26 × 26 mm (see **Figure 3.3(b)),** which were subsequently machined into tensile specimens. The specific recipes used for tensile testing are summarized in **Table 3**.

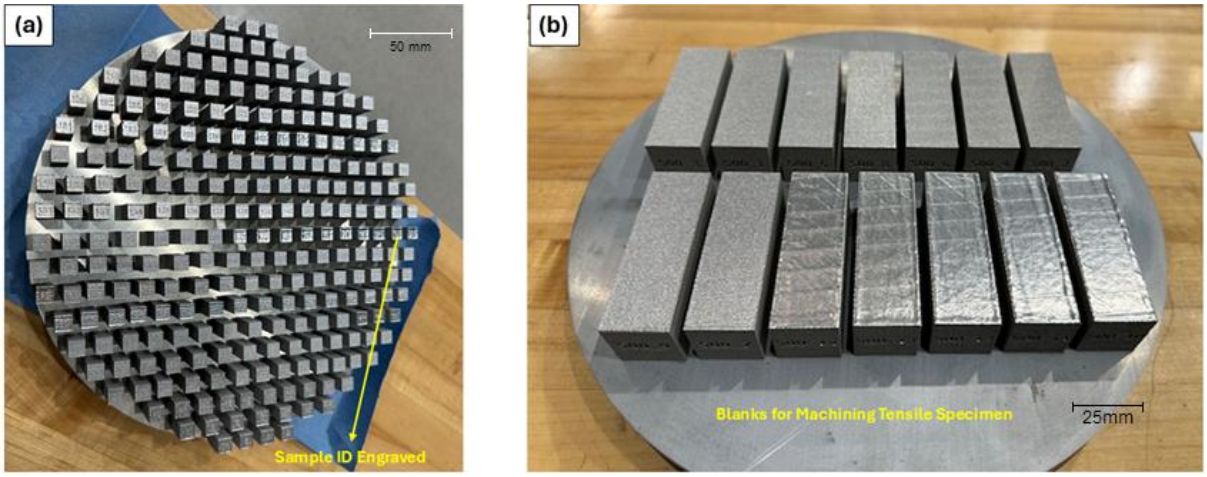



**Figure 3.3** Sample printed for (a) microstructural analysis, and (b) blanks for tensile testing

**Table 3.3** Recipes used for producing blanks for tensile testing and category

| Laser Power | Scanning Speed | Powder Bed Preheating Temperature | Category |
|---|---|---|---|
| *W* | *mm/s* | *Deg. C* | - |
| 150 | 1400 | 200, 300, 400, 500 | Poor |
| 150 | 1600 | 200, 300, 400, 500 | Poor |
| 300 | 600 | 200, 300, 400, 500 | Intermediate |
| 200 | 1400 | 200, 300, 400 | Intermediate |
| 150 | 1200 | 500 | Intermediate |
| 200 | 1000 | 200, 300, 400, 500 | Good |
| 300 | 800 | 200, 300, 400, 500 | Good |

### 3.2.3 Heat Treatment

To evaluate the response of LPBF-manufactured 17-4 PH SS in terms of the microstructural changes (with respect to the grain structure, phases, and precipitates) and mechanical properties, the samples were subjected to a standard two-stage heat treatment. The first stage, which is a solution treatment (Condition A), involved holding the material at 1050°C for 30 minutes, followed by water quenching to rapidly cool the material. This process was conducted in an inert Ar atmosphere to minimize oxidation. The second stage, which is aging (H900 condition), was performed by heating the samples to 482°C for 1 hour, followed by air cooling to room temperature.

## 3.3 Manufacturing Defect Quantification and Analysis

To evaluate the amount of manufacturing defects, and gain insights into the underlying mechanisms of their formation, the samples were prepared for examination by using a light optical microscope (LOM). A custom-developed programming code was employed for image analysis, and some of the samples were examined under a scanning electron microscope. The experimental details for each technique are outlined below.

### 3.3.1 Sample Preparation and Imaging

The samples designated for microstructural characterization were sectioned along the mid-plane parallel to the build direction by using wire EDM to enable the quantification and analysis of manufacturing defects. The sectioned samples were first mounted in Kemet conductive phenolic resin (Bakelite) to aid with grinding and polishing. Grinding was performed by using silica carbide (SiC) papers in ascending grit size from coarse (#400) to fine (#1200) grit, followed by using a polishing cloth with 6 μm and 1 μm diamond suspensions to achieve a

mirror finish. Finally, the polished samples underwent ultrasonic cleaning in ethyl alcohol to remove contaminants and ensure a clean surface for imaging.

A Clemax 2.0 LOM was used for the imaging, which is equipped with a 5× ocular lens and a 10× objective lens to provide a total magnification of 50×. For each sample, 10 images were captured at random locations along the build direction to ensure representative analysis. Each image covered an area of 9 $mm^2$ of the cross-section, which resulted in a total analyzed area of 90 $mm^2$ per sample.

### 3.3.2 Customized Python Script

To quantify the defect fractions from the optical micrographs, a customized Python script was developed to process each image which corresponds to a specific processing condition. Each micrograph was first converted to grayscale, followed by background subtraction with the use of a rolling ball algorithm implemented in the scikit-image library [89] to eliminate noise. Thresholding was then applied by using Yen's algorithm, which was selected for its robustness in handling noisy images and complex backgrounds [90]. Regions with defects were identified by using the regionprops function in the skimage.measure module, thus enabling the extraction of area and morphology data. The total defective area for each image was calculated by summing the pixel areas of all regions with defects, and the area fraction was obtained by a ratio of this value to the total number of pixels in the image. For each sample, the average fraction of the area with defects was reported based on ten micrographs. The overall methodology is shown in **Figure 3.4(a)** to **3.4(e)**.

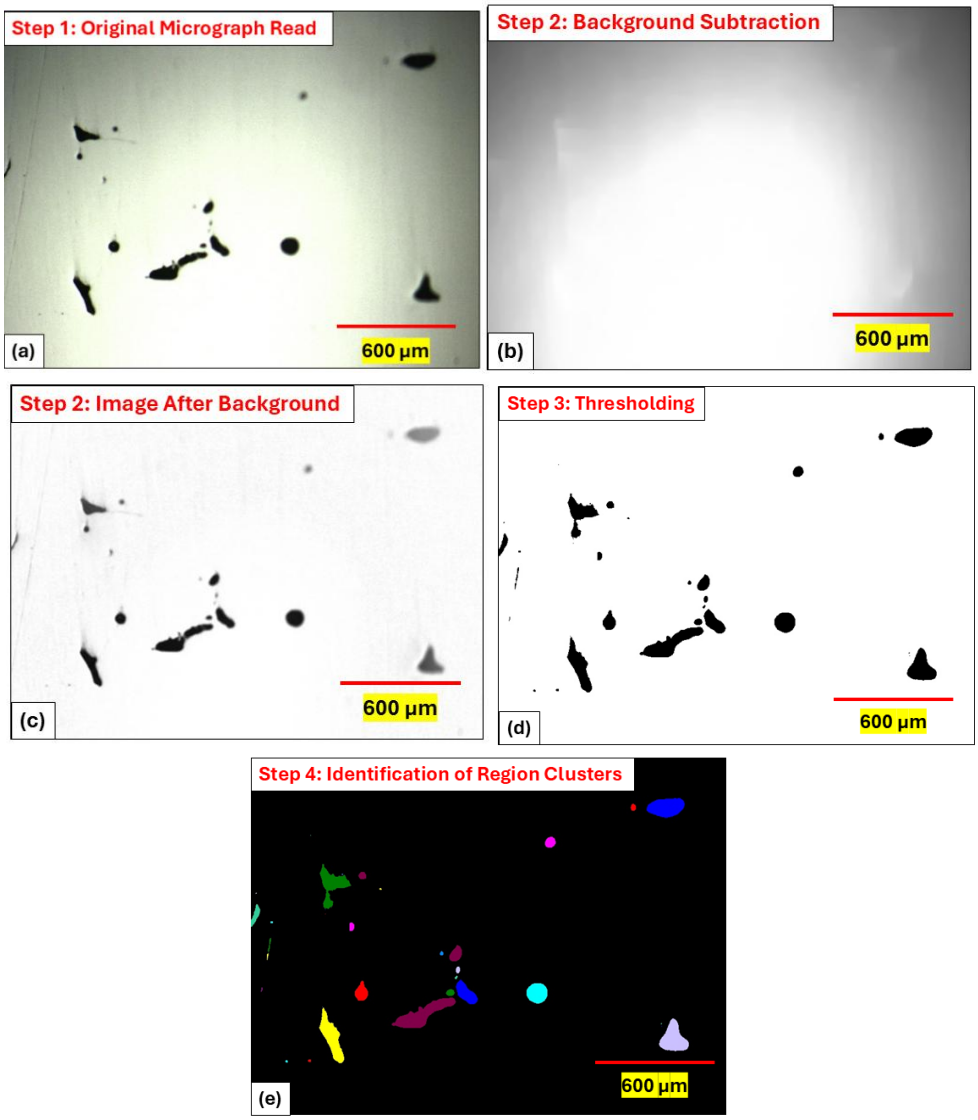



**Figure 3.4** Methodology for calculating fractions of manufacturing defects from optical micrographs

To validate the accuracy of the developed script, fractions of defect from selected samples that exhibited varying degrees of manufacturing defects were independently calculated by using ImageJ software, and followed the same image processing steps as outlined above. A comparison of the results obtained from both methods is presented in **Table 3.4**. The two sets of values are in close agreement, and the statistical t-test shows no significant difference between the results, therefore confirming the reliability and accuracy of the developed Python script.

**Table 3.4** Results for select samples from each category calculated by using traditional image analysis method with Image J software vs. customized Python script compared via paired t-test

| Sample No. | Sample ID | Category | Fraction of Defect (Image J) | | Fraction of Defect (Python Script) | | Validation | |
|---|---|---|---|---|---|---|---|---|
| | - | - | *Average* | *Standard Deviation* | *Average* | *Standard Deviation* | *t-value* | *p-value* |
| **1** | P150V1200T500 | Intermediate | 1.757 | 0.273 | 1.767 | 0.340 | -0.066 | 0.948 |
| **2** | P200V1400T400 | Intermediate | 0.577 | 0.127 | 0.579 | 0.080 | -0.056 | 0.956 |
| **3** | P150V1600T200 | Poor | 22.472 | 1.588 | 22.260 | 1.090 | 0.435 | 0.669 |
| **4** | P150V1400T300 | Poor | 5.633 | 0.771 | 5.800 | 0.784 | -0.476 | 0.639 |
| **5** | P300V800T400 | Good | 0.056 | 0.037 | 0.049 | 0.032 | 0.489 | 0.631 |
| **6** | P200V1000T300 | Good | 0.378 | 0.218 | 0.369 | 0.200 | 0.097 | 0.924 |

### 3.3.3 Scanning Electron Microscopy

A scanning electron microscope utilizes an electron beam rather than visible light to generate high-resolution images. Due to the shorter wavelength of the electrons, SEM enables imaging at higher magnifications, and provides higher resolution and greater depth of focus. In this study, a Philips XL30 scanning electron microscope is employed to examine fine defect features and investigate the formation mechanisms of the manufacturing defects. All of the imaging was performed at an accelerating voltage of 20 kV with a working distance of 10 mm.

## 3.4 Material Characterization

To evaluate the influence of the process parameters on the mechanical properties, both the as-built and heat-treated samples were subjected to microstructural characterization. Their grain structure was analyzed by using standard metallographic techniques, phase identification was performed via x-ray diffraction (XRD), and precipitation behaviour was examined by using transmission electron microscopy (TEM). The specific equipment utilized and the corresponding sample preparation procedures are detailed below.

### 3.4.1 Metallography

To reveal the grain and weld pool structures, the samples were prepared by using a standard metallographic procedure in ASTM E3-11 [91]. The plane sectioned parallel to the build direction was mounted, grinded, and polished similar to the procedure described in Section **3.3.1.** Following the polishing, the samples were etched by swabbing for 20 s by using a waterless Kalling's reagent (6.25 g of cupuric chloride ($CuCl_2$), 125 ml of hydrochloric acid (HCl), and 125 ml of ethanol).

### 3.4.2 X-Ray Diffraction

To identify and quantify the bulk phases found in both the as-built and heat-treated states, an XRD analysis was conducted. A Siemens D5000 X-ray diffractometer, equipped with a Cu Kα radiation source, was employed to acquire diffraction patterns over a 2θ range of 10°–110°, with a step size of 0.02°. The sample preparation involved sectioning the additively manufactured builds by using EDM, followed by sequential grinding with SiC abrasive papers that range from coarse (#240) to fine (#1200) grit. The final polishing was performed by using a 6-µm diamond suspension to achieve the required surface finish for the XRD analysis. The XRD patterns were analyzed with X'pert Highscore software [92] for phase identification and quantification.

### 3.4.3 Transmission Electron Microscopy

The precipitation behaviour of 17-4 PH SS was analyzed by using an FEI Talos F200X transmission electron microscope. Thin foil specimens were prepared through a series of mechanical and electrochemical processing steps. Initially, ~1 mm-thick plates were extracted from the additively manufactured samples by using EDM. These plates were mechanically grinded to a final thickness of 90–100 µm by using #600 grit SiC abrasive paper. Discs of 3

mm in diameter were subsequently punched from the plates. To achieve electron transparency, the discs underwent dimple grinding with a 3-μm diamond paste. The final thinning was performed via electro-polishing by using a twin-jet polisher at 233 K in an electrolyte solution that comprised 10 vol% perchloric acid and 90 vol% methanol.

## 3.5 Mechanical Testing

To evaluate the mechanical performance of the material, both hardness measurements and tensile testing were carried out. The following section outlines the equipment used and the sample preparation procedures employed for each test.

### 3.5.1 Hardness Testing

Macrohardness testing was conducted by using a Vickers hardness tester with an applied load of 10 kg. Measurements were taken at 1 mm intervals along the build direction, from the bottom to the top, to maximize the sample area, which provided a total of 20 measurements for each specimen. Before indentation, the specimens were sectioned along the build direction, mounted, grinded, and polished following the procedure outlined in Section **3.3.1**.

### 3.5.2 Tensile Testing

Uniaxial and quasi-static tensile tests were conducted to evaluate the tensile properties of the material in both the as-built and heat-treated conditions. The testing protocol followed the ASTM E8/E8M standard [93], with a strain rate of $0.5 \times 10^{-3}$ $s^{-1}$ applied up to a strain of 1.5%, and increased to $1.5 \times 10^{-3}$ $s^{-1}$ beyond that point. For each condition, the mechanical properties were determined by taking the average results of three tests.

The specimens were prepared from a cuboidal blank that measured 78 × 26 × 26 mm, which was fabricated by using LPBF. The tensile profile, which conforms to the subsize specimen geometry prescribed in ASTM E8/E8M, was machined by using EDM. Subsequently, the specimens were sectioned into a uniform thickness of 6 mm (see **Figure .5(a) and 3.5(b)**).

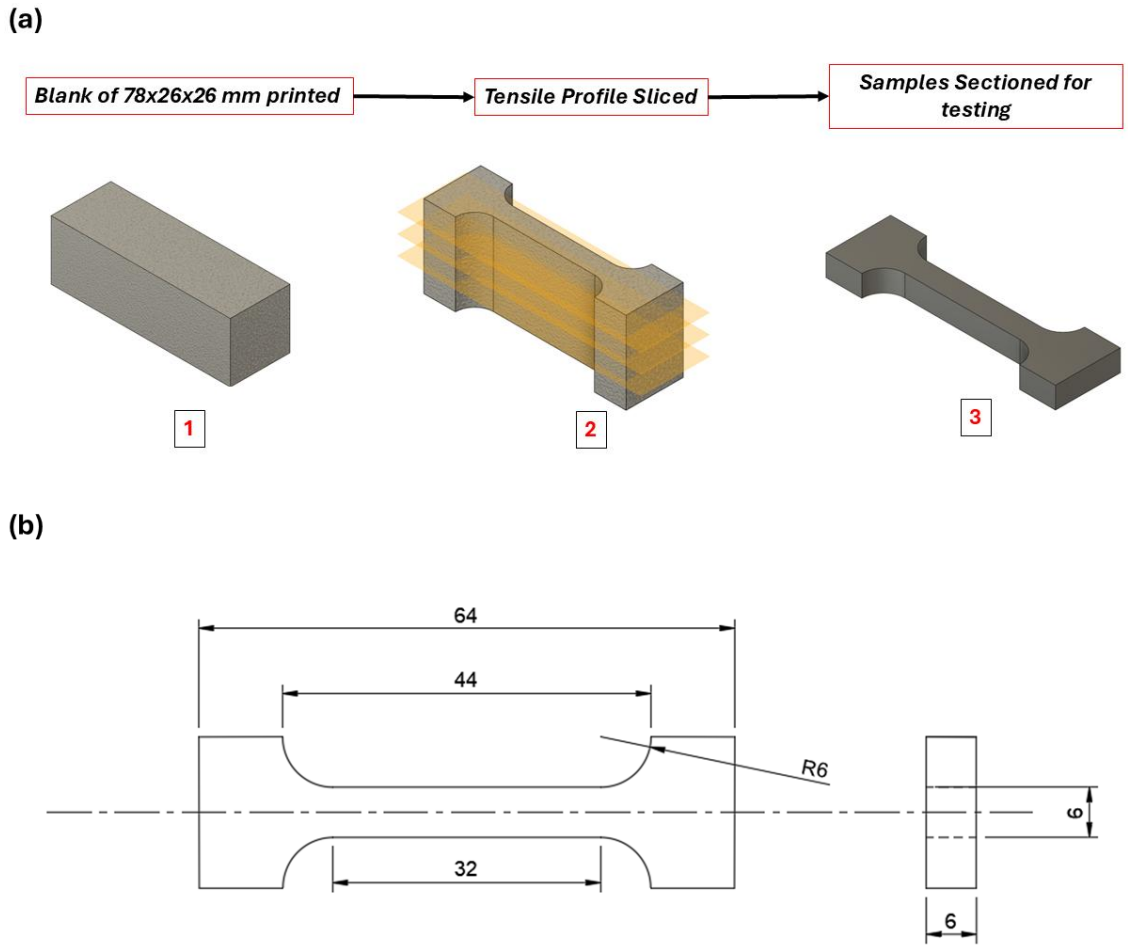



**Figure 3.5** Method used to obtain samples for (a) tensile testing from additively manufactured material, along with (b) detailed dimensions

# Chapter 4: Results and Discussion

This chapter presents the study results. First, the relationship between the process parameters and defect formation is established. Based on the defect levels, the best, intermediate, and poorest representative samples are selected and tested in the as-built condition to evaluate the correlation between manufacturing defects and mechanical behaviour. The samples with the best performance, which are largely free of manufacturing defects, are subjected to further microstructural characterisation to investigate the influence of other microstructure variables on the mechanical properties in the absence of manufacturing defects. Finally, all of the samples are subjected to a heat treatment, and the resulting phase changes and mechanical behaviour are evaluated.

## 4.1 Effect of Process Parameters on Manufacturing Defects

This section investigates the influence of the process parameters on the formation of manufacturing defects, identifies the processing conditions that produce defect-free samples in the form of an optimal processing window, and examines the underlying mechanisms that are responsible for the formation of manufacturing defects.

### 4.1.1 Effect of Laser Scanning Speed

To investigate the effect of the scanning speed on the formation of manufacturing defects in LPBF-produced 17-4 PH SS, builds were carried out at four distinct laser powers, namely 150 W, 200 W, 250 W, and 300 W. These power levels are chosen so that a wide array of recipes can be investigated, which allows for builds to take place under different “modes” of printing

[87, [88]. A wide range of energy densities were explored, which vary from 11.72 to 62.50 J/mm$^3$. The effects of the scanning speed on the number of manufacturing defects and morphology were analyzed both qualitatively, by using optical micrographs, and quantitatively, by using the data from 10 such micrographs. The builds were classified into 3 regimes based on the energy density: low, moderate, and high-energy density regimes. Metallographic and SEM investigations were done on the representative samples across all three regimes, and the reason for the formation of detects was subsequently identified.

**Figure 4.1(a)** and **4.1(b)** present the optical micrographs and corresponding defect fractions for the samples produced by using different combinations of laser power and scanning speeds. The micrographs are color-coded to represent the three categories based on defect content: best (green), intermediate (yellow), and poor (red). These images, taken along the build direction, reveal the qualitative influence of scanning speed on both the number of manufacturing defects and morphology. Based on the observed cross-sectional features, the builds can be broadly classified into three regimes: (i) low LED, which typically results from the use of low laser power and high scanning speed; (ii) moderate LED, which arises from using the same level of laser power and scanning speed; and (iii) high LED, which is produced by using a high laser power and low scanning speed.

As shown in **Figure 4.1(c),** samples fabricated in the low LED regime exhibit a significant increase in defect fraction with increased scanning speed. Conversely, in the high LED regime (**Figure 4.1(e)**), excessive energy input at low scanning speeds also results in a high defect content. Notably, the samples processed within the moderate LED (**Figure 4.1(d)**) show a U-shaped trend in the defect fraction, with an optimal range that yields nearly defect-free builds. This highlights the critical role of carefully finetuning laser power and scanning speed to minimize the formation of manufacturing defects and optimize the build quality.

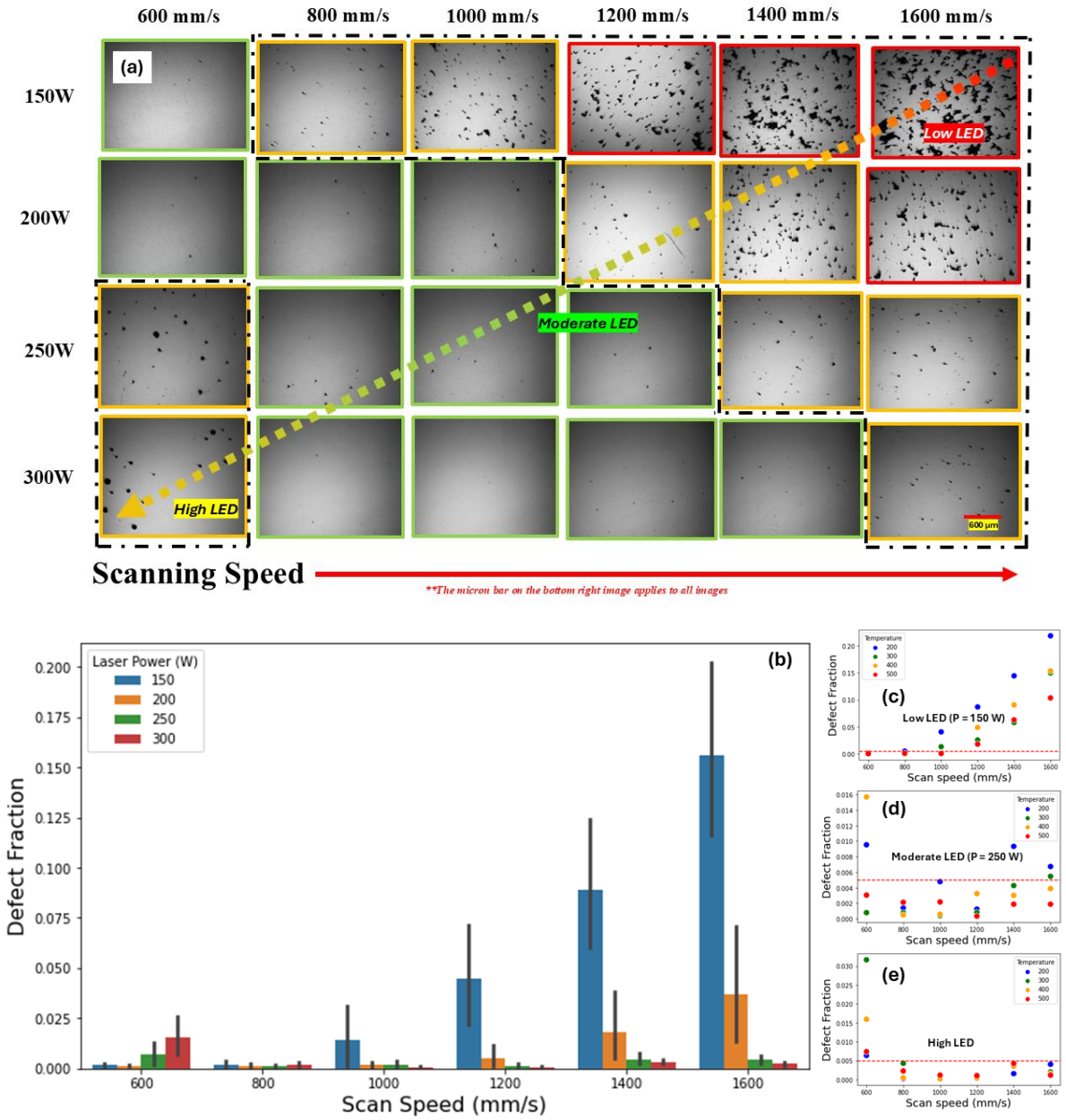



**Figure 4.1** Effect of scanning speed on manufacturing defect formation shown through (a) optical micrographs, and (b) data across all laser powers, with trends of (c) low energy density, (d) moderate energy density, and (e) high energy density regimes.

**Figure 4.2** presents the effect of the scanning speed on defect size distribution for samples built in the identified regimes. The distributions are categorized by morphology: near-circular (circularity > 0.9) and irregular manufacturing defects (circularity < 0.9), to obtain insights into the effect on defect morphology. The low energy density regime, represented by **Figure 4.2(a)**,

produces samples that show a defect size distribution that is dominated by "irregular" types of manufacturing defects. Not only is the number fraction but also the size of these manufacturing defects significantly larger than the "near-circular" type of manufacturing defects. The samples built in the moderate energy density regime (**Figure 4.24(b)**) show a similar partition based on number fractions. However, the defect size of both types of manufacturing defects is small. The samples printed in the high energy density regime (**Figure 4.24(c)**), show a different defect size distribution compared to the low and moderate energy density regimes. The segregated defect size distributions nearly overlap for the third case, thus producing large near-circular manufacturing defects.

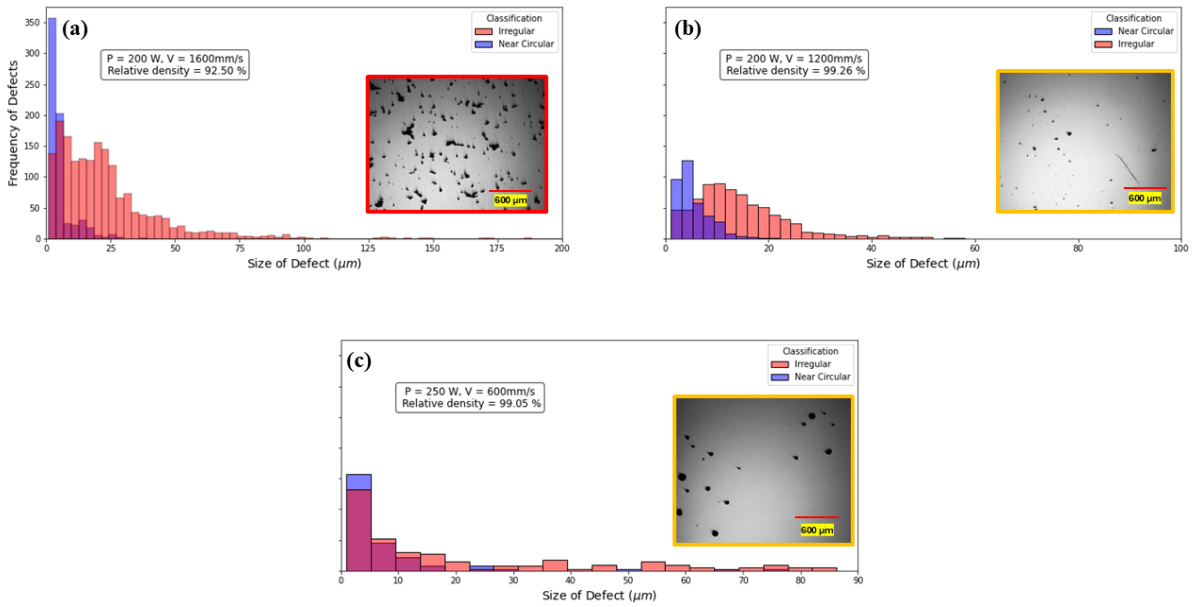



**Figure 4.2** Effect of laser scanning speed on manufacturing defect size distribution, for samples printed at 200 W and (a) 1600 mm/s, (b) 1200 mm/s, (c) 1000 mm/s and (d) 250 W, 600 mm/s

To identify the underlying mechanism that leads to the formation of manufacturing defects due to scanning speed variations, micrographs of the defective samples from each regime are presented in **Figure 4.3**. **Figure 4.3(a)** presents one such micrograph from a sample built in the low LED regime which is classified as poor. The manufacturing defects are large and irregular, with a corresponding SEM image that reveals unmelted powder within them, thus indicating

that LOF is the mechanism that contributes to the formation of manufacturing defects. **Figure 4.3(b)** presents an etched micrograph taken from a sample built in a low-LED regime with a moderate level of manufacturing defects, thus revealing partial overlapping of the melt pool, which is also indicative of the LOF. Both of these samples were printed in the low-LED regime, thus indicating that an increased scanning speed for a given laser power leads to insufficient powder melting, which leaves the builds susceptible to the formation of LOF defects. The manufacturing defects shown in **Figure 4.3(c),** however, are near-circular manufacturing defects with complete overlapping of the melt pool. Such manufacturing defects are termed keyhole defects [15], [17], [18], [96] and may form because of fluctuations in the fluid flow at high energy densities where a deep keyhole-shaped melt pool that is unstable forms. The gas within the build chamber may be entrapped if the keyhole-shaped melt pool collapses, thus creating gas bubbles in the liquid metal. The gas bubbles are then essentially subjected to two types of forces: the Marangoni force, which pushes the gas bubbles down, and a buoyancy force, which pushes the gas bubbles up [17]. If the former dominates, the gas bubbles are trapped in the liquid metal, which creates a near-circular defect. Some recent in-situ studies [97], [98] show that discontinuities in the laser scan path significantly contribute to bubble retention, thus indicating that the energy input, driven by the scanning speed, may not be the only reason for such manufacturing defects.

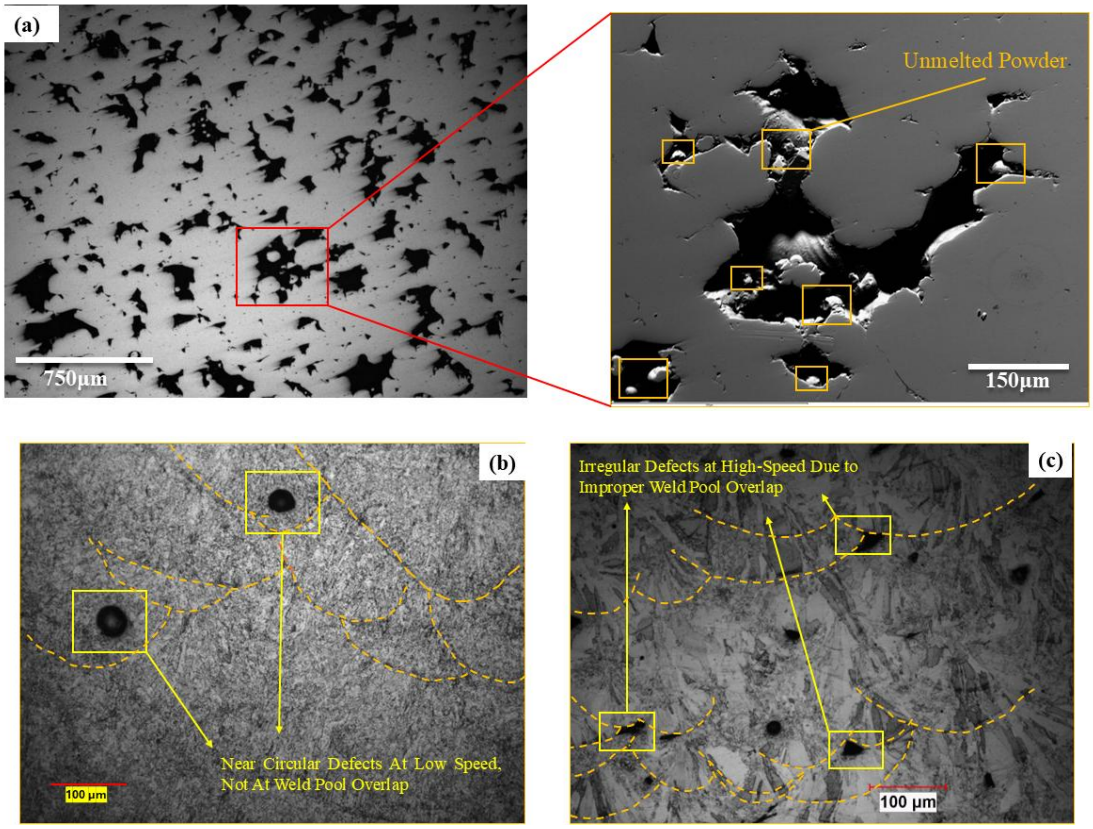
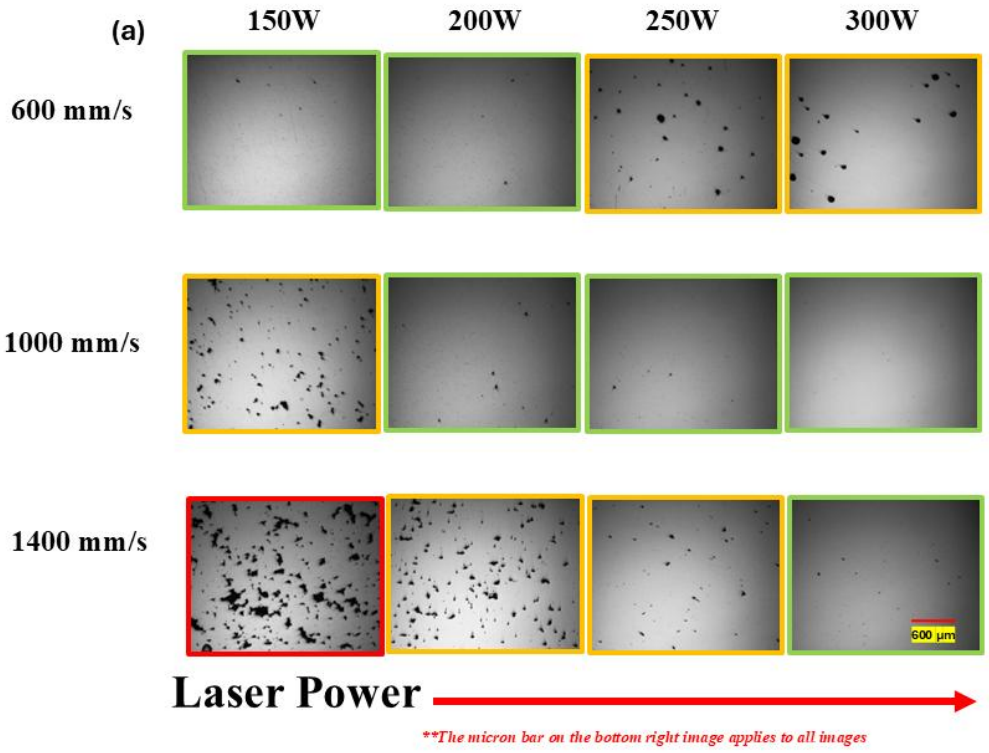



**Figure 4.3** (a) Optical micrograph and corresponding SEM image of sample built in low LED regime which shows unmelted powder particles. Etched optical micrographs reveal (b) insufficient overlap of melt pool in the low LED sample and (c) large circular (keyhole) manufacturing defects in the high LED sample.

### 4.1.2 Effect of Laser Power

The effect of the laser power was studied by using samples built at different scanning speed rates, namely low (600 and 800 mm/s), intermediate (1000 and 1200 mm/s), and high (1400 and 1600 mm/s) scanning rates. The effect of the laser power was first analyzed by using the optical micrographs of sections cut along the build direction and then, quantitatively, by examining the defect levels. Insights into the defect morphology were also made. Finally, the etched micrographs were used to identify the mechanism behind the formation of manufacturing defects in the energy density regimes.

**Figure 4.4(a)** and **4.4(b)** show the effect of the laser power through optical micrographs and defect fraction of the sample cross-sections along the build direction at three different scanning speeds, with different colors of the image borders denoting the defect level. The micrographs reveal that at intermediate and high scanning speeds, the defect fraction decreases with increases in laser power. In contrast, at low scanning speeds, the opposite pattern is observed, in which the defect fraction increases with increases in laser power. This is further supported by a quantitative analysis, which shows a consistent decrease in defect content with increases in laser power at intermediate and higher scanning speeds, and an increase in defect content with increases in laser power at a low scanning speed (**Figure 4.4(c)** to **4.4(e)**). The overall defect levels are the highest with low laser power-high scanning speed. Notably, nearly circular manufacturing defects are observed when a high laser power and low scanning speed is used, which suggests that a mechanism such as keyholing governs these builds.



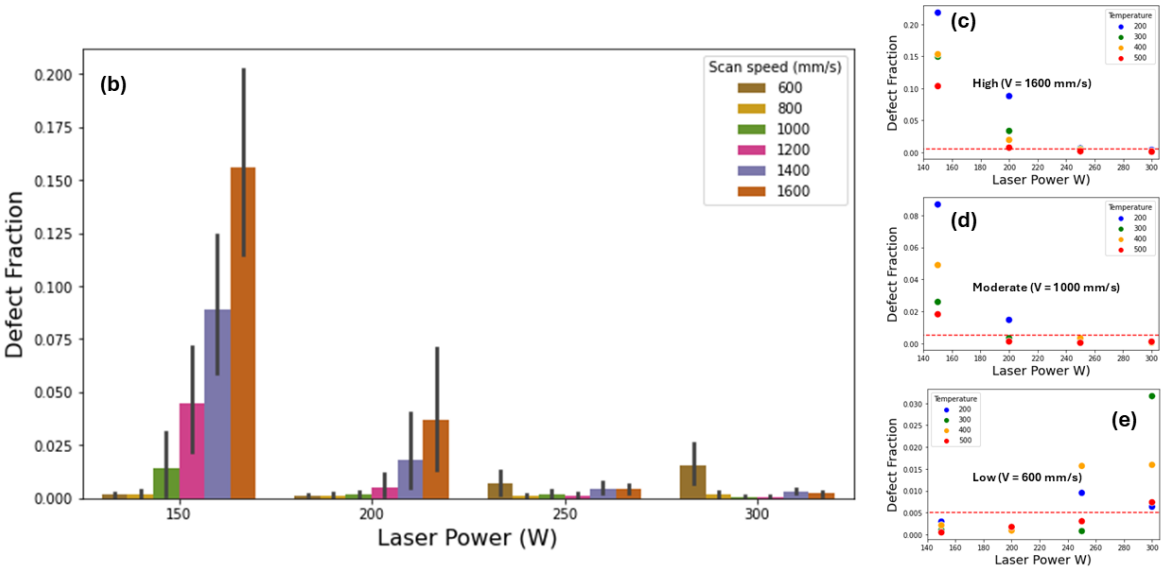
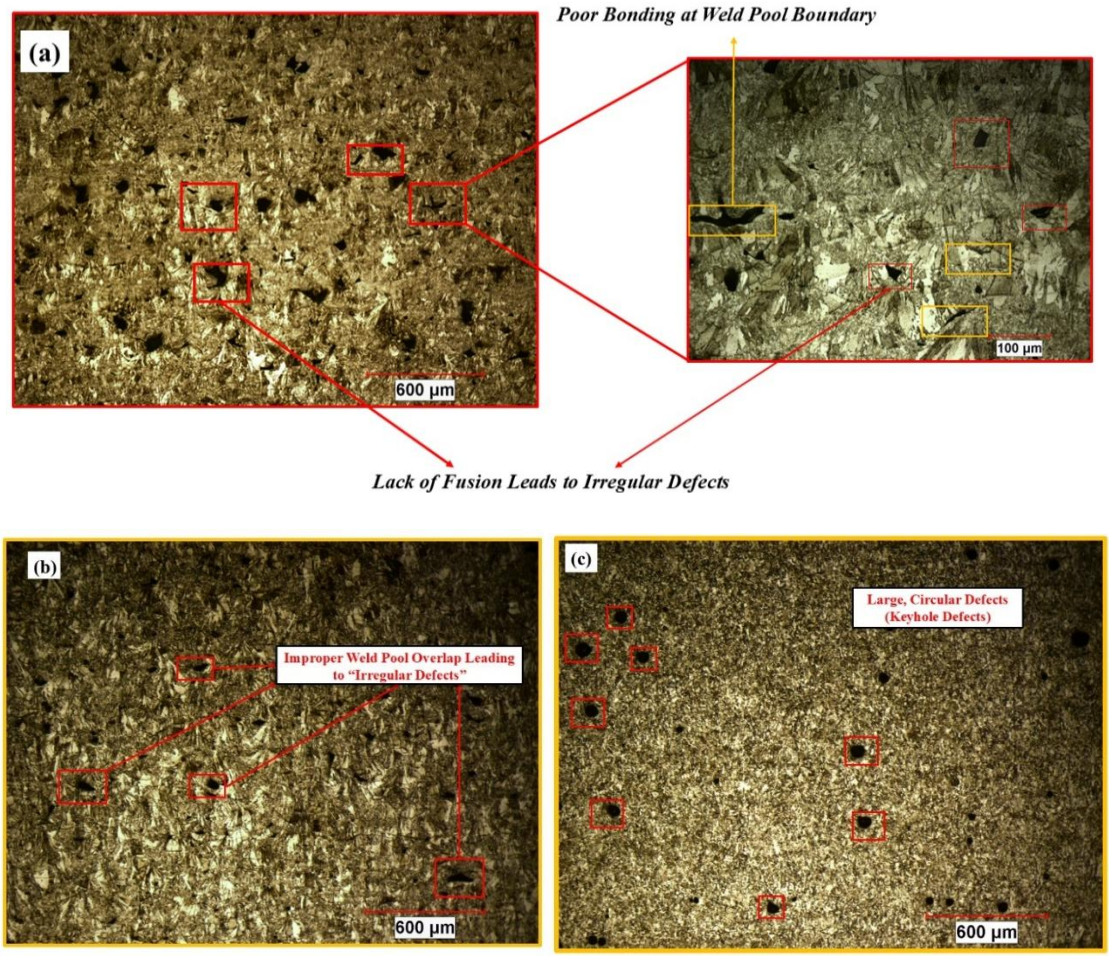



**Figure 4.4** Effect of laser power on manufacturing defect formation: (a) optical micrographs, and (b) data across all scanning speeds, with patterns show for (c) low energy density, (d) moderate energy density, and (e) high energy density regimes.

**Figure 4.5** shows the etched micrographs of the samples built in each energy density regime. **Figure 4.5(a)** and **4.5(b)** show the sample built in the low LED regime. Manufacturing defects form at the edges of the weld pools, specifically due to partial overlapping of the weld tracks. These samples also show unmelted powder within the manufacturing defects as revealed by the SEM micrograph in **Figure 4.5(d).** These are LOF defects and originate as the laser power is insufficient to allow adequate powder to melt for a given scanning speed. **Figure 4.5(c)** presents the samples built in the high LED regime. The weld pools completely overlap; however, manufacturing defects still form in the form of keyhole-induced porosity. Hence, similar to the scanning speed, an optimal laser power is required to produce good-quality, defect-free builds. A low laser power can leave the build susceptible to LOF defects, which can be extremely large manufacturing defects with entrapped unmelted powder when coupled with high scanning speeds. On the other hand, builds made with high laser power are susceptible to keyhole defects when coupled with a

lower scanning speed. Hence, choosing an optimal laser power-scanning speed combination is crucial to reduce manufacturing defects in LPBF-manufactured 17-4 PH SS.



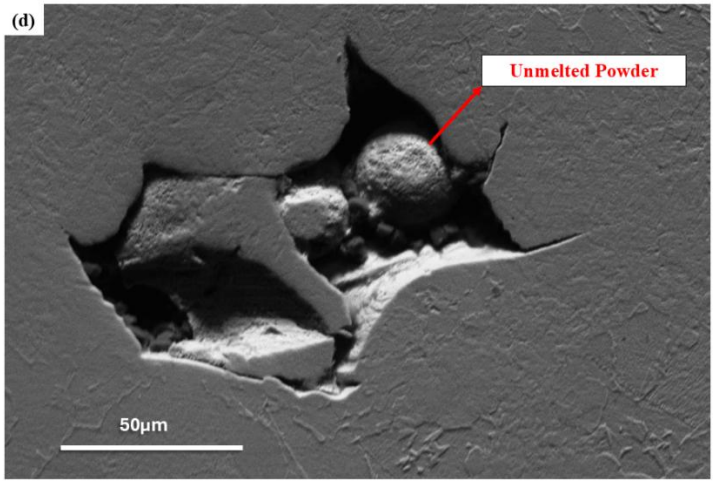



**Figure 4.5** Optical micrographs of samples produced at (a) 150 W (poor), (b) 200 W (Intermediate-low LED), and (c)300 W (Intermediate-high LED) that show manufacturing defect formation mechanism of each case

### 4.1.3 Effect of Powder Bed Preheating Temperature

Samples built in each of the identified regimes were used to determine the effect of the powder bed temperature on the formation of manufacturing defects. This includes the effect of powder bed preheating on different energy densities that have been used to build the samples. First, the effect on each regime is visualized by using optical micrographs from cross-sections of the samples, then quantitatively examined by analyzing the defect fractions.

**Figure 4.6** presents the optical micrographs of the samples produced at 4 different laser power-scanning speeds, along with the powder bed temperature for each combination, and arranged in order of increasing energy density. The build produced at a laser power of 150 W and scanning speed of 1400 mm/s (LED regime) shows reduced defect fraction; however, the sample does not approach the threshold where it would not be considered poor. The build produced in the low-moderate energy density regime represented by a laser power of 250 W and scanning speed of 1200 mm/s shows improvement as the powder bed temperature increases, and thus acceptable defect levels at 400°C and 500°C. The samples built in the optimal combination of laser power of 300 W at a scanning speed of 800 mm/s, and high energy

density range with a laser power of 300 W at a scanning speed of 600 mm/s show nearly no variation with an increase in the powder bed temperature.

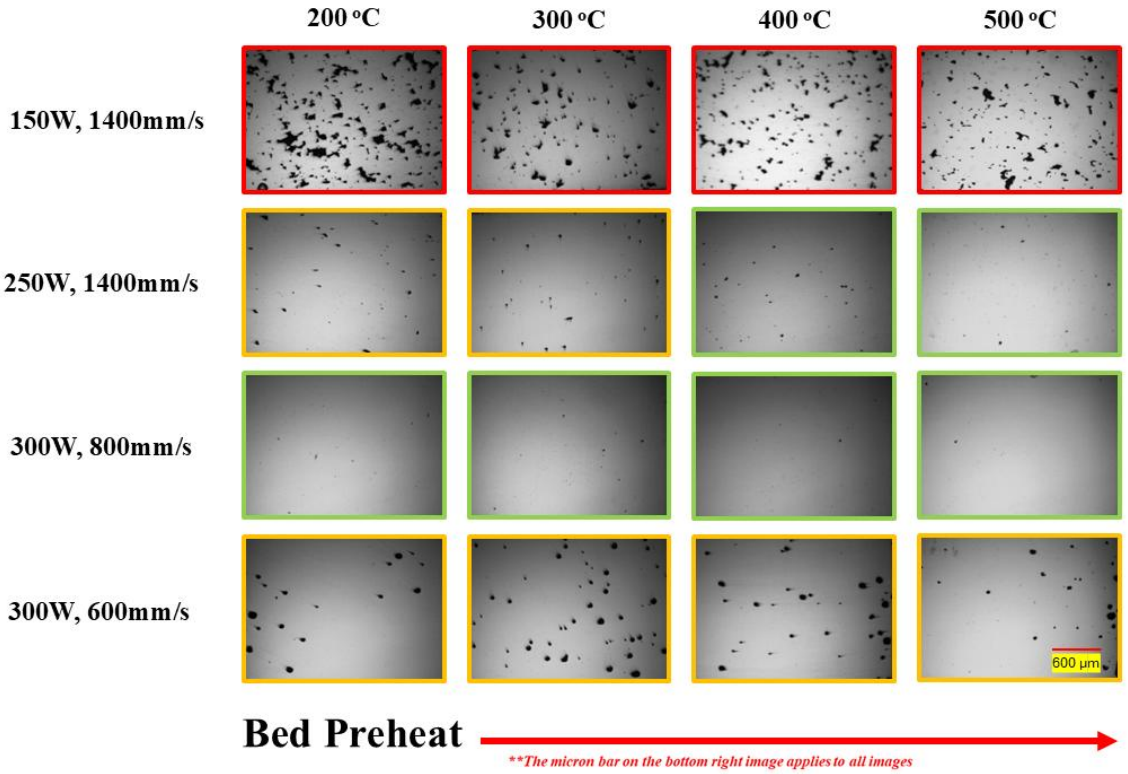



**Figure 4.6** Optical micrographs that show effect of powder bed preheating on manufacturing defects for samples produced at different laser power and scanning speeds

**Figure 4.7(a)** presents the calculated defect fractions for samples built across different powder bed temperatures, with the laser power and scanning speed represented by the x- and y-axes, and the defect fraction by the z-axis. The results show that samples produced in the low LED regime exhibit a marked reduction in defect content as the powder bed temperature increases. In contrast, samples built under a moderate or high-LED condition remain largely unaffected by changes in the powder bed temperature. This leads to a notable enhancement of the optimal processing window from 200°C to 500°C, which is primarily driven by improved relative density at lower energy inputs. The overall effect of increasing the powder bed temperature is

a flattening of the defect surface, which stabilizes the process and makes it easier to achieve builds with a defect fraction below 0.5%.

This enhanced process stability is further illustrated in the energy density plotted in **Figure 4.7(b)** and **4.7(c)**. The former shows the relationship between the defect fraction and LED across different powder bed temperatures, where a consistent trend is observed and a clear improvement is seen as preheating temperature rises. Specifically, the lower energy density region exhibits a reduced sensitivity to the effects of LED, thus contributing to the broader optimal window. **Figure 4.7(c)** quantifies this window by showing the minimum, maximum, and range of LEDs that yield builds with a densification of over 99.5%. As the powder bed temperature increases, the acceptable working range expands, which increases from approximately 0.187 J/mm to 0.273 J/mm, primarily due to a reduction in the minimum energy required for producing fully dense parts.

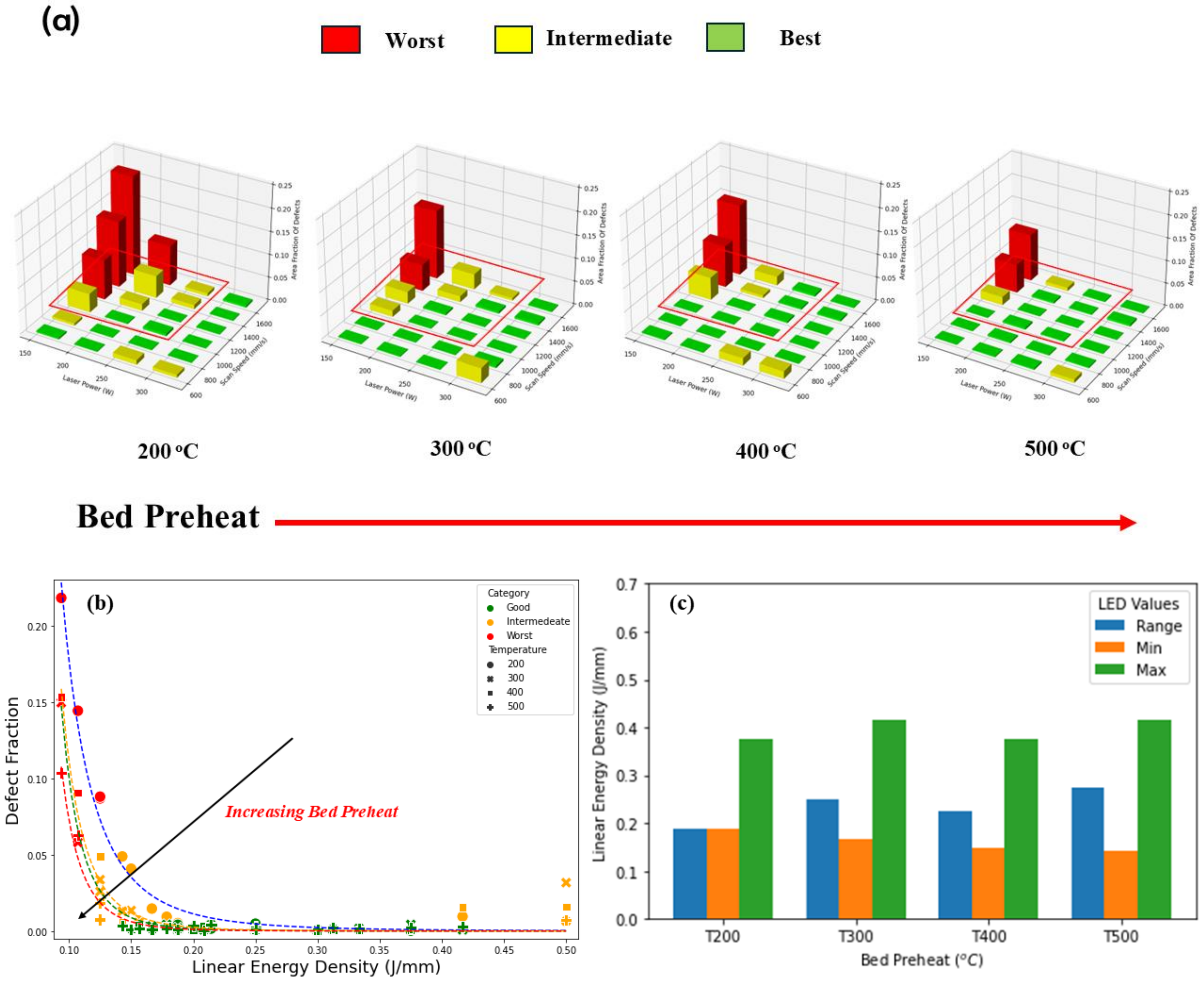
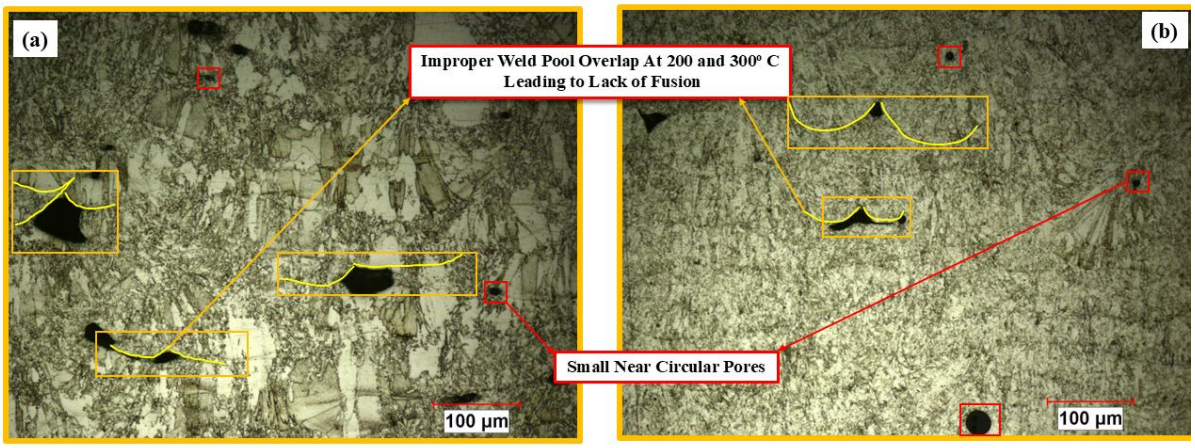



**Figure 4.7** Manufacturing defect fraction with (a) process map across increasing powder bed preheating temperatures, (b) energy density dependence, and (c) enhanced working ranges

As the powder bed temperature increases, some of the samples produced in the low-LED regime shift from intermediate to the best category. This can be attributed to a reduction in the number of LOF defects that form within the samples. **Figure 4.8** provides evidence for the same by presenting etched micrographs of the sample produced at a laser power of 250 W, and scanning speed of 1400 mm/s for all of the investigated powder bed temperatures. At lower temperatures (200°C and 300°C), there is partial overlap but when the powder bed temperature increases, the melt pool overlap is more complete, and nearly no LOF defect is seen in the build at 500°C. Researchers have predicted such a phenomenon for other systems, such as Inconel

718 [99], and Ti alloys [41] by using analytical models. Some researchers, like Chen et al. [55] also reported single-track experiments on weld pool expansion at higher powder bed temperatures. The builds that show this increase in relative density lie on the lower energy end of the process map, where the dominant mode of heat transfer is conduction [11], [20], [94]. At elevated powder bed temperatures, more material melts at a given LED owing to the enhancement in thermal conductivity of the material, which produces a reduced temperature gradient. Hence, the improvement in the relative density at elevated powder bed temperatures may be explained by a reduction in the LOF through more material melting owing to the enhancement in thermal conductivity of the material, which results in a larger weld pool with a smoother temperature gradient.



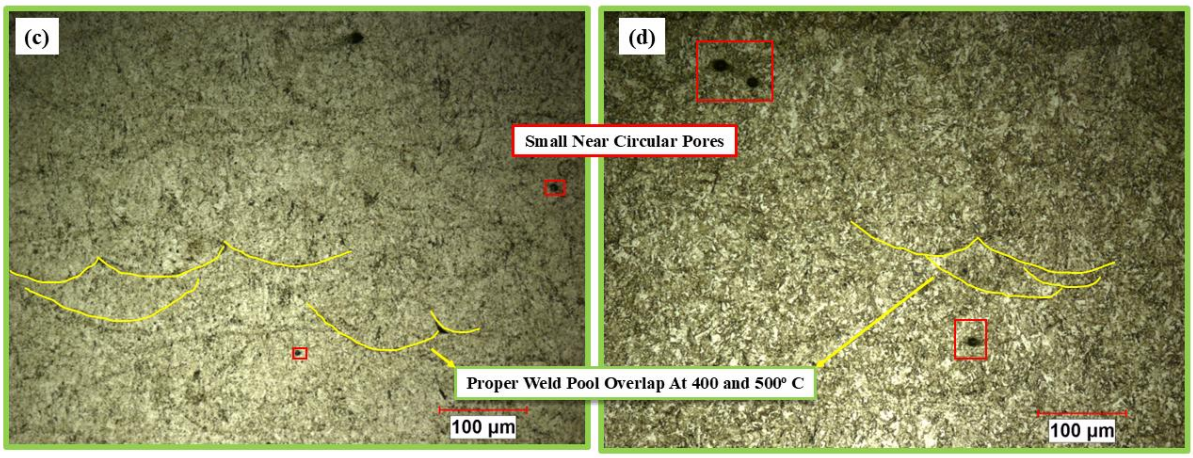



**Figure 4.8** Etched micrographs that show partial melt pool overlap at (a) 200°C, and (b) 300°C, and complete melt pool overlap at (c) 400°C, and (d) 500°C

### 4.1.4 Summary of Process Parameters and Defect Formation

A systematic investigation of the influence of the process parameters on the formation of manufacturing defects has been conducted in this study. The amount of manufacturing defects and morphology are both monitored with the use of different laser powers, scanning speeds, and powder bed temperatures to understand the effect of each parameter and identify the underlying mechanism for the formation of manufacturing defects in a wide range of processing conditions. Based on the analysis, an optimal process window, which consistently achieves > 99.5% relative density, has been identified.

The interplay of laser power and scanning speed plays a crucial role in formation of manufacturing defects. Low laser power-high scanning speed conditions are the most problematic as they lead to extremely large and highly irregular manufacturing defects with entrapped unmelted powder. These are LOF defects that occur due to insufficient energy input, characterized by low LED. These form due to partial melt pool overlapping of successive scan paths, and their formation is governed by the thermal conductivity of the material. On the other hand, high laser power-low scanning speed conditions can also lead to formation of

manufacturing defects. However, the manufacturing defects are large and circular in morphology. These are keyhole defects that form due to fluid flow fluctuations in the keyhole-shaped weld pool, which leads to entrapped gas that are trapped before solidification occurs. When the laser power and scanning speed are both moderate, it is possible to produce samples that are fully dense and show near-zero defects. This shows that there is an optimal LED range, where the energy input is adequate for complete melt pool overlap, as well as a stable fluid flow, thus preventing the formation of manufacturing defects.

An increase in the preheating temperature contributes to achieving a fully dense build by enhancing the thermal conductivity of the material. Owing to a higher thermal conductivity, builds at elevated preheating temperatures allow for more material to melt in the low LED regime, thereby expanding the workable LED range. However, preheating does not significantly affect the manufacturing defects that occur due to excessive energy input, which are keyhole defects independent of the thermal conductivity of the material. Such effects have been reported and predicted for various materials through computational studies, such as computational fluid dynamics (CFD) studies [99] and numerical modelling [41], [100], as well as single-track experiments [55]. However, these have not been done for a full build, especially 17-4 PH SS. The current findings suggest that printing at an higher preheating temperature can make the LPBF process more stable and controllable for 17-4 PH SS, thus leading to improved consistency and build quality.

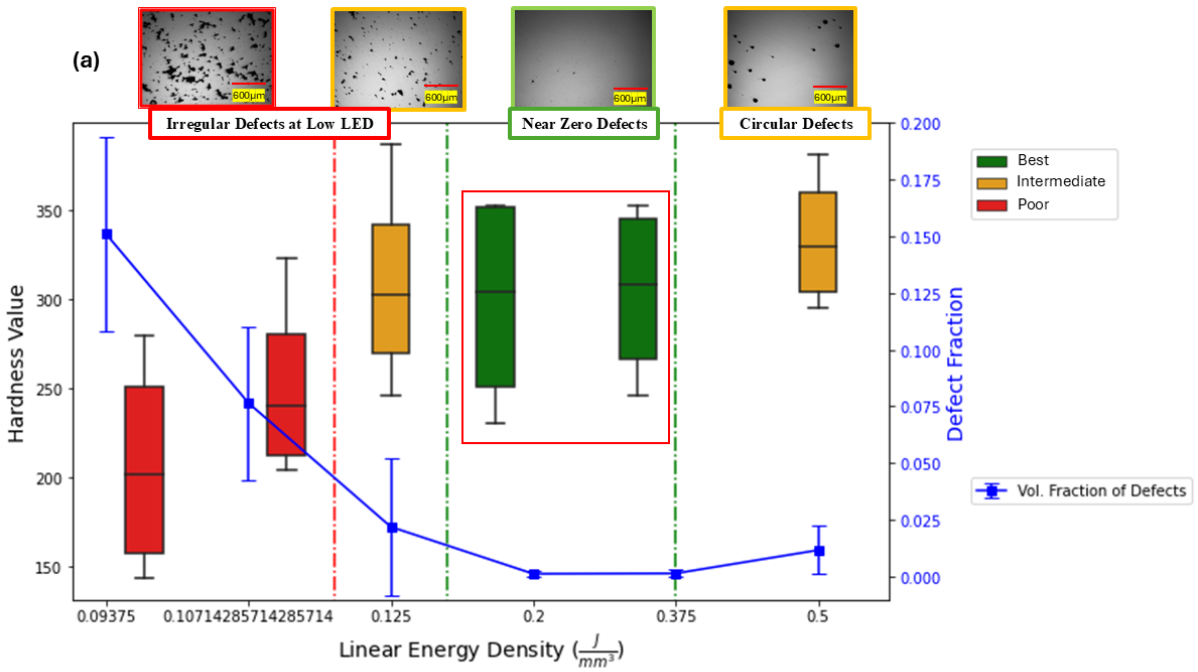
## 4.2 Mechanical Performance of the As-built Material

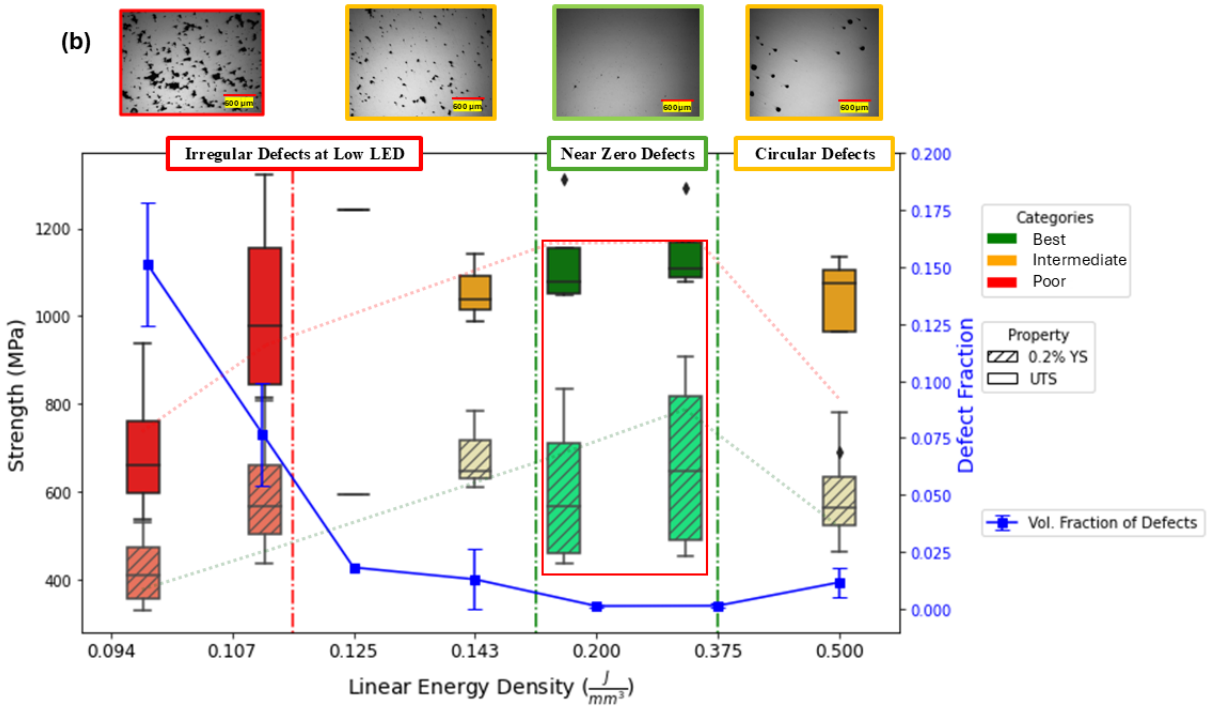
To understand the influence of the process parameters on mechanical properties, as-built samples were subjected to both hardness and tensile testing. A few samples from each group were chosen as representative samples to capture the variability of the mechanical properties.

Here, the effect of manufacturing defects is first discussed in terms of defect content and morphology on the mechanical properties and relates them to the process parameters. The tensile properties from each group of samples are also compared to the standard expectation of the alloy. Then, the discussion shifts to samples that show near zero manufacturing defects, where the phases are quantified to understand how phase variations influence the mechanical properties within the optimal working window.

### 4.2.1 Effect of Manufacturing Defects on Mechanical Behavior

**Figure 4.9(a) – 4.9(c)** show the correlation of the mechanical properties with the defect fraction and LED. The mechanical properties are presented in the form of box plots of samples tested at each LED across all of the powder bed temperatures. Additionally, the blue line plot shows the average defect fraction and associated error under the same conditions to highlight the variations in manufacturing defects with LED. It can be observed that all of the properties, namely, hardness (**Figure 4.9(a)**), yield and ultimate tensile strengths (**Figure 4.9(b)**), and elongation percentage (**Figure 4.9(c)**) show a good correlation with the defect fraction and LED. The samples printed within the optimal energy density range perform the best and show the fewest manufacturing defects. Similarly, the samples with low and intermediate levels of manufacturing defects are in agreement with the results of the defect fractions. While the properties are in agreement well with the defect fraction, the defect morphology seems to have minimal effect on the mechanical performance. The mechanical performance is similar for all of the samples with intermediate levels of manufacturing defects, irrespective of the defect morphology, which may be highly irregular if the sample is printed in the lower LED regime, or nearly circular if the sample is printed in the high LED regime. Overall, this indicates that minimizing the defect content is crucial for optimizing the mechanical performance of 17-4 PH SS.


(a)
Irregular Defects at Low LED
Near Zero Defects
Circular Defects
Hardness Value
Defect Fraction
Linear Energy Density ($\frac{J}{mm^3}$)
0.09375
0.10714285714285714
0.125
0.2
0.375
0.5
Best
Intermediate
Poor
Vol. Fraction of Defects


(b)
Irregular Defects at Low LED
Near Zero Defects
Circular Defects
Strength (MPa)
Defect Fraction
Linear Energy Density ($\frac{J}{mm^3}$)
0.094
0.107
0.125
0.143
0.200
0.375
0.500
Categories
Best
Intermediate
Poor
Property
0.2% YS
UTS
Vol. Fraction of Defects

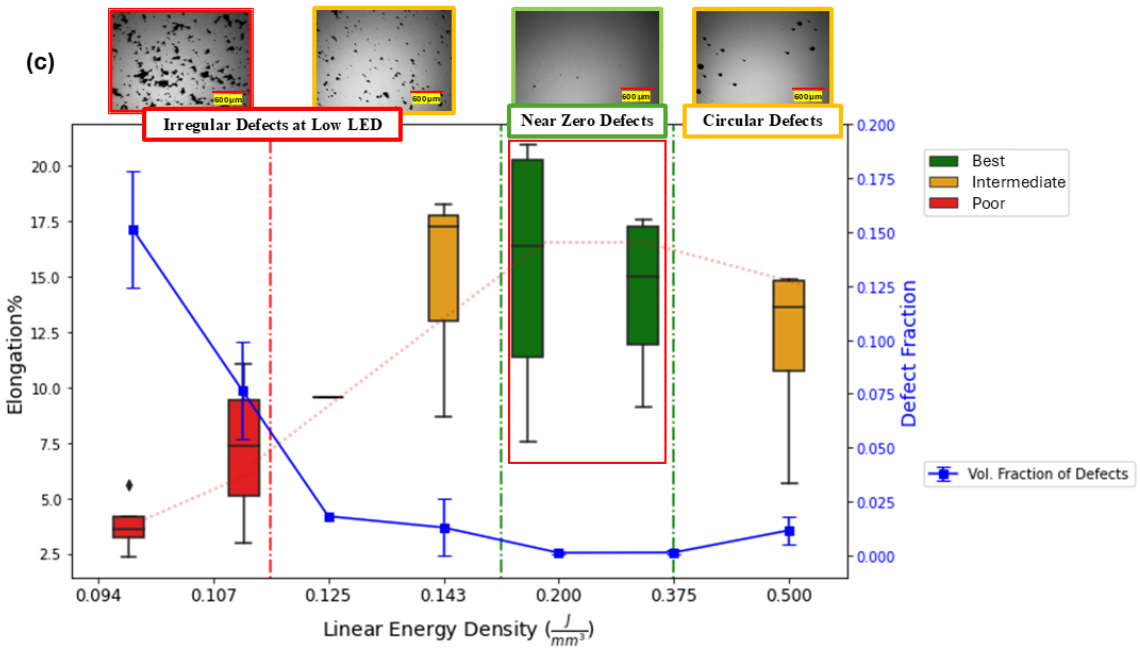



**Figure 4.9** Correlation of (a) hardness, (b) strength, and (c) ductility with manufacturing defect fraction and LED

**Figure 4.10(a) and 4.10(b)** show the tensile properties, along with the corresponding error, of all the samples compared to the standard expectation for the alloy, as defined by ASTM A693-24. The samples with near-zero manufacturing defects outperform those of the other categories. However, these samples fail to meet the yield and tensile strength requirements for the use of the alloy in the industry (see **Figure 4.10(a)**). On the other hand, ductility requirements are met by both the samples that are classified as intermediate and the best (**Figure 4.10(b)**).

It is interesting that despite a near zero defect, the properties of the samples that perform the best vary the most out of the those in the three categories (see red box in **Figure 4.9(a)-4.9(c)**), thus indicating that another microstructural variable controls its performance. Additionally, a

post-deposition heat treatment is conducted to increase the strength of the material to make it usable.

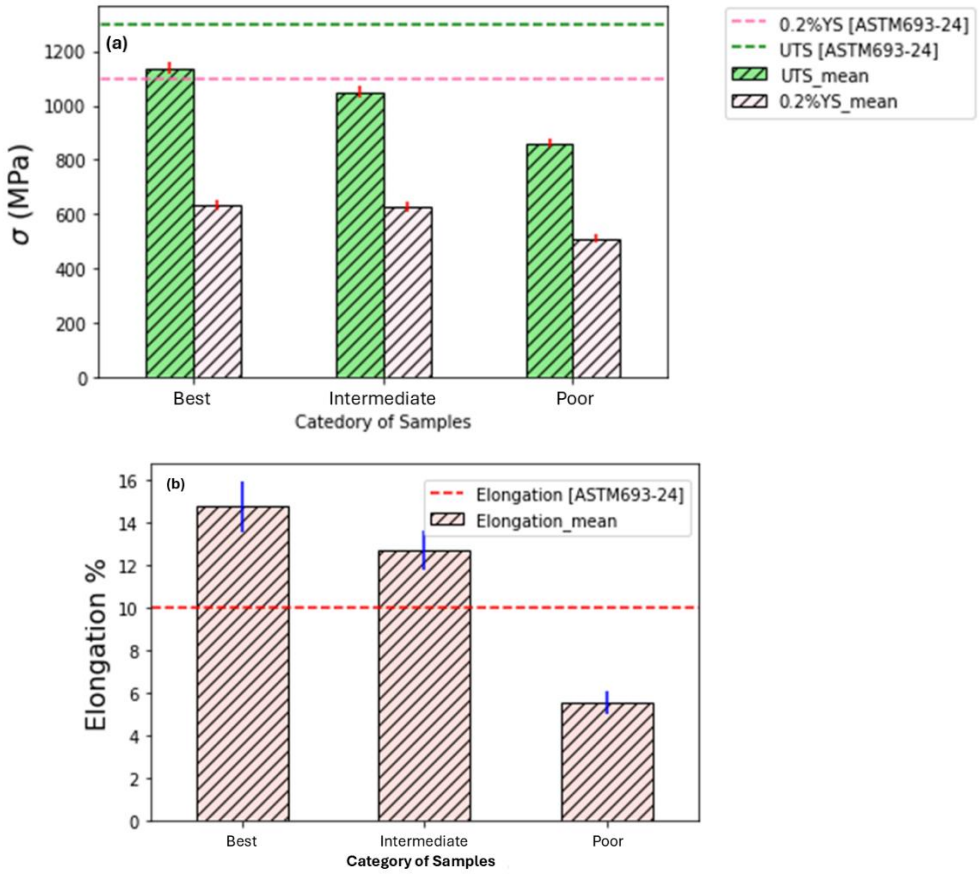



**Figure 4.10** Tensile properties of samples in as-built condition, compared to samples that follow ASTM A693-24 in terms of (a) strength, and (b) ductility

### 4.2.2 Samples with Near-zero Manufacturing Defects

A significant variation in strength and ductility is observed in the absence of manufacturing defects, which suggests that the mechanical behaviour of the components is governed by the underlying microstructural features. To investigate this relationship, a comprehensive quantification of the phases was conducted and correlated with the measured mechanical properties and process parameters in this section.

#### 4.2.2.1 Variation in Mechanical Behavior with Process Parameters

**Figure 4.11** presents the hardness of the samples produced by using different process recipes within the optimal working window, where near-zero manufacturing defects are observed. Despite the absence of manufacturing defects, a considerable variation in hardness is evident. While the samples fabricated at similar LED values exhibit comparable hardness, increasing the powder bed temperature leads to more variability. Furthermore, the samples built at 200°C and 300°C are significantly less hard, whereas those built at 400°C and 500°C are more hard.

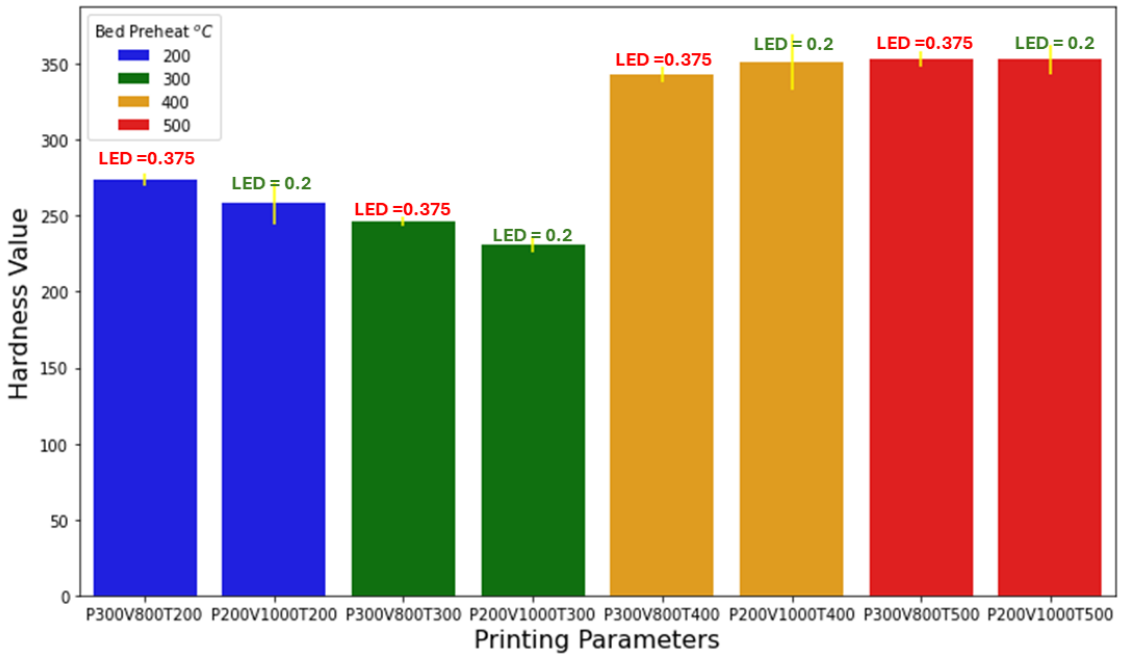



**Figure 4.11** Hardness of samples within optimal processing window that show near zero manufacturing defects

**Figure 4.12(a)** plots the quasi-static stress-strain curves of samples with near-zero manufacturing defects. Similar to the hardness results, the samples printed at the same temperature exhibit comparable tensile behavior, while a significant variation emerges as the temperature is increased. Specifically, samples printed at 200°C and 300°C show lower yield and ultimate tensile strengths with extreme ductility, whereas those produced at 400°C and 500°C exhibit higher (**Figure 4.12(b)**) strength but reduced ductility (**Figure 4.12(c)**).

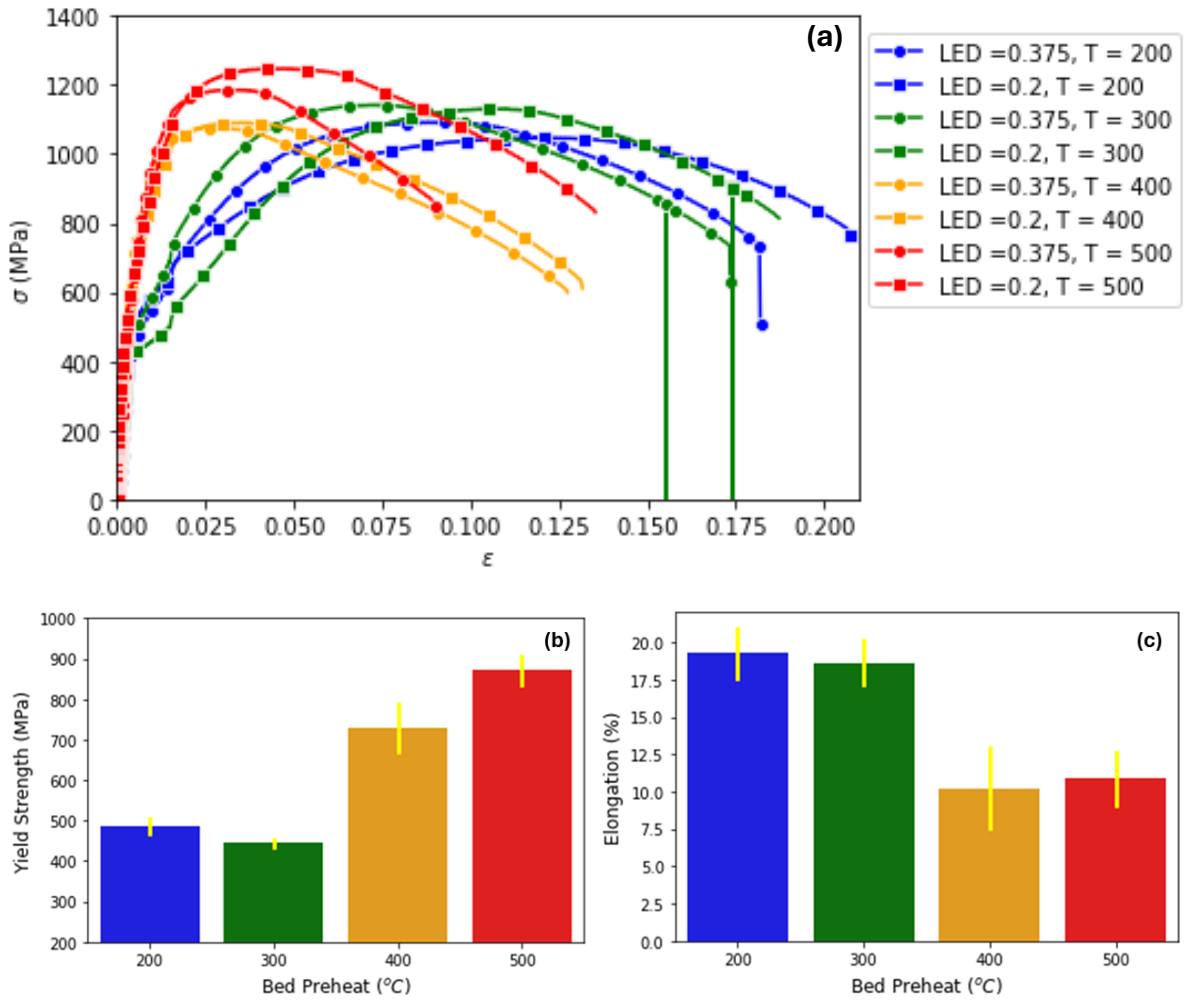



**Figure 4.12** Samples with near-zero manufacturing defects that show varying (a) tensile curves, (b) yield strength, and (c) ductility

Overall, the builds exhibit variation in mechanical performance, even in the absence of manufacturing defects. While changes in laser power and scanning speed have a minimal effect, the powder bed temperature plays a significant role in influencing the mechanical properties.

#### 4.2.2.2 Variation in Phase Composition with Process Parameters

To explain the variation in the mechanical properties despite the absence of manufacturing defects, the grain structure and phases found in the samples are analyzed. First, the optical micrographs of the etched samples are examined to evaluate the grain structure, followed by an XRD analysis to identify the bulk phases. Finally, TEM is employed to investigate any in-situ precipitation that may have contributed to the observed variation.

**Figure 4.13** presents the optical micrographs of samples built within the optimal processing window but with different processing recipes. The laser power and scanning speed are 200 W and 1000 mm/s respectively, while the powder bed temperature varies from 200°C to 500°C; see **Figures 4.13(a) to 4.13(d)**. The micrographs show the weld pool mesostructure in all of the samples, which is characteristic of the LPBF process. However, within the mesostructures, the grain morphology varies significantly. The samples that correspond to lower powder bed temperatures (200°C and 300°C) show a mix of columnar and fine-grained structures; however, only the fine-grained structure is obvious at a higher temperature. The columnar grain shows an epitaxial growth, which is not found in the fine-grained structure. Researchers have observed this mixed grain structure in the as-built 17-4 PH SS, which is attributed to the presence of δ-ferrite within the material [71], [82], [101], [102]. For 17-4 PH SS, the primary solidification mode is ferritic, and phase transformations follow the sequence of δ-ferrite → γ-austenite → α'-martensite. If the cooling rate is high enough, the first step from δ to γ may not be completed, which locks in the δ-ferrite.

To further investigate this phase variation, XRD is utilized as shown in **Figure 4.14**. For all the samples, XRD reveals a mix of FCC-austenite and BCT/BCC-martensite/ferrite. The samples built at lower temperatures show a significant amount of austenite, that is, 40% and 35% at 200°C and 300°C, respectively. In contrast, the austenite fraction at higher temperatures is lower, or close to 10% at 400°C and 500°C.

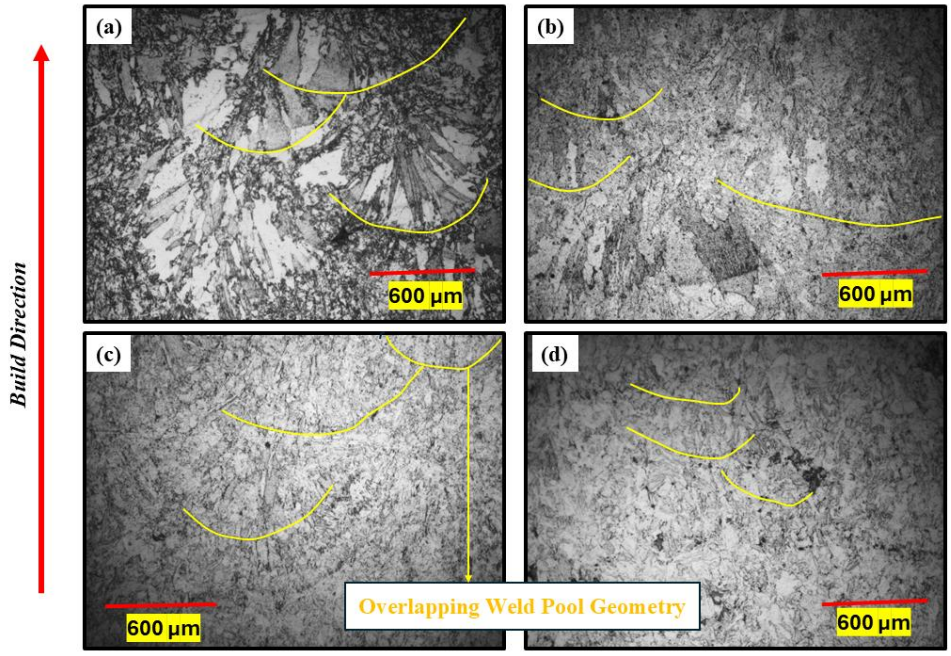



**Figure 4.13** Optical micrograph that show dual grain structure of fully dense samples built at (a) 200°C, (b) 300°C, (c) 400°C, and (d) 500°C

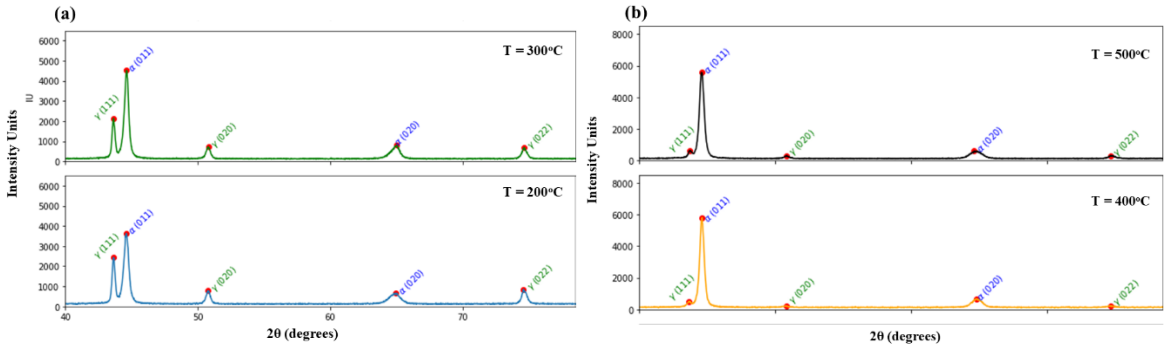



**Figure 4.14** XRD patterns for the samples built at (a) lower (200°C, and 300°C), and (b) higher (400°C and 500°C) powder bed temperatures

The nano-scale copper clusters are the primary strengthening phase within 17-4 PH SS. To investigate this phase in the as-built condition, scanning transmission electron microscopy (STEM) and EDS are utilized (**Figure 4.15**). However, no copper clustering is observed for the as-built state. The STEM investigation only reveals nano-scale oxides that are rich in Si and Mn. These phases are the spinel and rhodonite phases, known to be undesirable within the build

[103]. The absence of copper clusters and the existence of spinel/rhodonite phases can together lead to a worse mechanical performance [103].

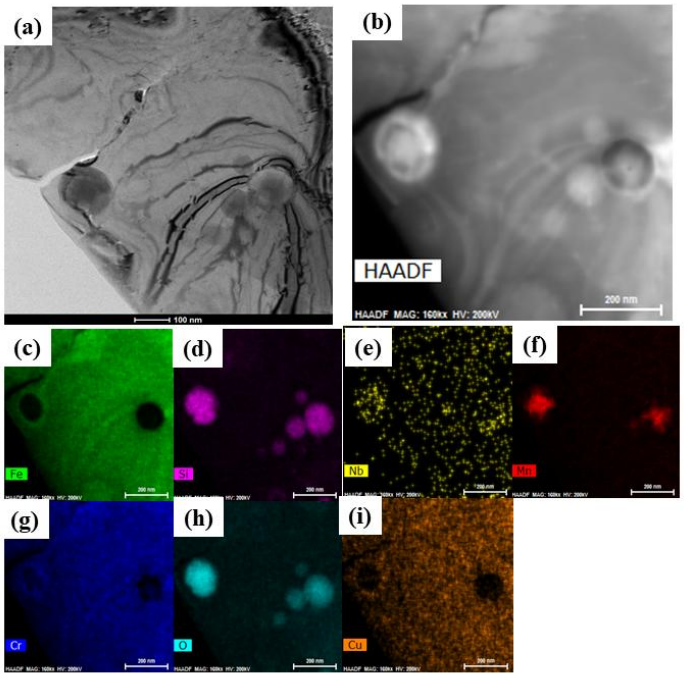



**Figure 4.15** (a) TEM image and corresponding selected area diffraction pattern (SADP), (b) corresponding high-angle annular dark-field (HAADF) image, and (c)-(i) EDS mapping which reveals nano-scale oxides without any copper clustering in as-built condition

To understand such phase composition variation with powder bed preheating, a schematic continuous cooling transformation (CCT) curve as shown in **Figure 4.16** is used. The cooling occurs in two steps. The first is the thermal cycling of the primary build at an elevated powder bed temperature, followed by cooling of the build to room temperature. For 17-4 PH SS, the primary mode of solidification is ferritic [63], [82], [104]. The δ-ferrite subsequently transforms into a mixture of ferrite and austenite during the initial build [104]. However, as the martensite start temperature (Ms) of the alloy is lower than that of the preheating temperature (approximately 130–143 °C)[105], martensite formation does not occur during these primary build scans. As the temperature is increased, the resulting slower cooling rates promote a more complete δ→γ (ferrite to austenite) transformation. This is supported by the optical micrographs, which reveal a significantly more columnar grain structure at low preheating

temperatures, and as such, is indicative of δ-ferrite retention. This retained δ-ferrite is supersaturated with C and N, as the alloy C and N content (typically 0.07% and 0.04%) is higher than what is soluble in δ-ferrite (<0.01%).

During the second cooling, during which the elevated preheating temperature is reduced to room temperature, martensitic transformation is expected. However, samples built at lower temperatures exhibit a large amount of retained austenite. Similar behaviour has been observed in the printing of certain tool steels at a certain preheating temperature [53] and has been attributed to austenite stabilization via C diffusion. In the case of 17-4 PH, retained austenite is typically found at the ferrite grain boundaries and solidification cell boundaries [82], [101]. This phenomenon can be attributed to the subsequent thermal cycles induced by successive scan paths, during which austenite nucleates at ferrite crystal defects (like grain boundaries and solidification cell boundaries). Additionally, δ-ferrite, which is in a supersaturated state, rejects carbon and N into adjacent austenitic regions [106]. This stabilizes the austenite phase, so that it is still found at room temperature. At higher bed preheating temperatures, more retained austenite and longer thermal exposure allows uniform distribution of the carbon and N throughout the material, thereby facilitating a more complete transformation to martensite during the final cooling cycle. Furthermore, since martensite is never aged during the process, and only forms during the secondary cooling, no copper precipitation can be observed in the samples.

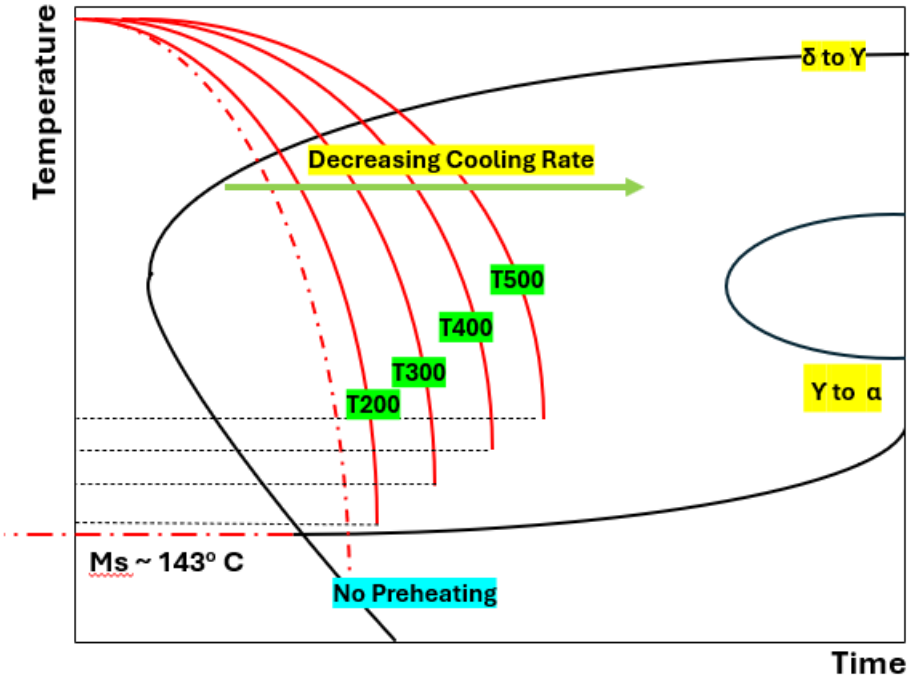



**Figure 4.16** Schematic CCT curves for LPBF produced 17-4 PH SS to explain variation with powder bed preheating temperature

#### 4.2.2.3 Correlation of Phases and Mechanical Properties

**Figure 4.17(a) – 4.17(c)** are bar graphs and scatter plots that show the correlation between the mechanical properties (hardness, strength, and ductility) and phase composition variations with powder bed temperature. Samples built at lower temperatures retain more austenite content, thus resulting in significant softening, reduced strength, and higher ductility. In contrast, samples processed at higher temperatures are harder, stronger, but less ductile. Notably, the strength is always significantly lower than the standard expectations of the alloy due to a lack of copper precipitation, which is also attributed to building at a higher temperature.

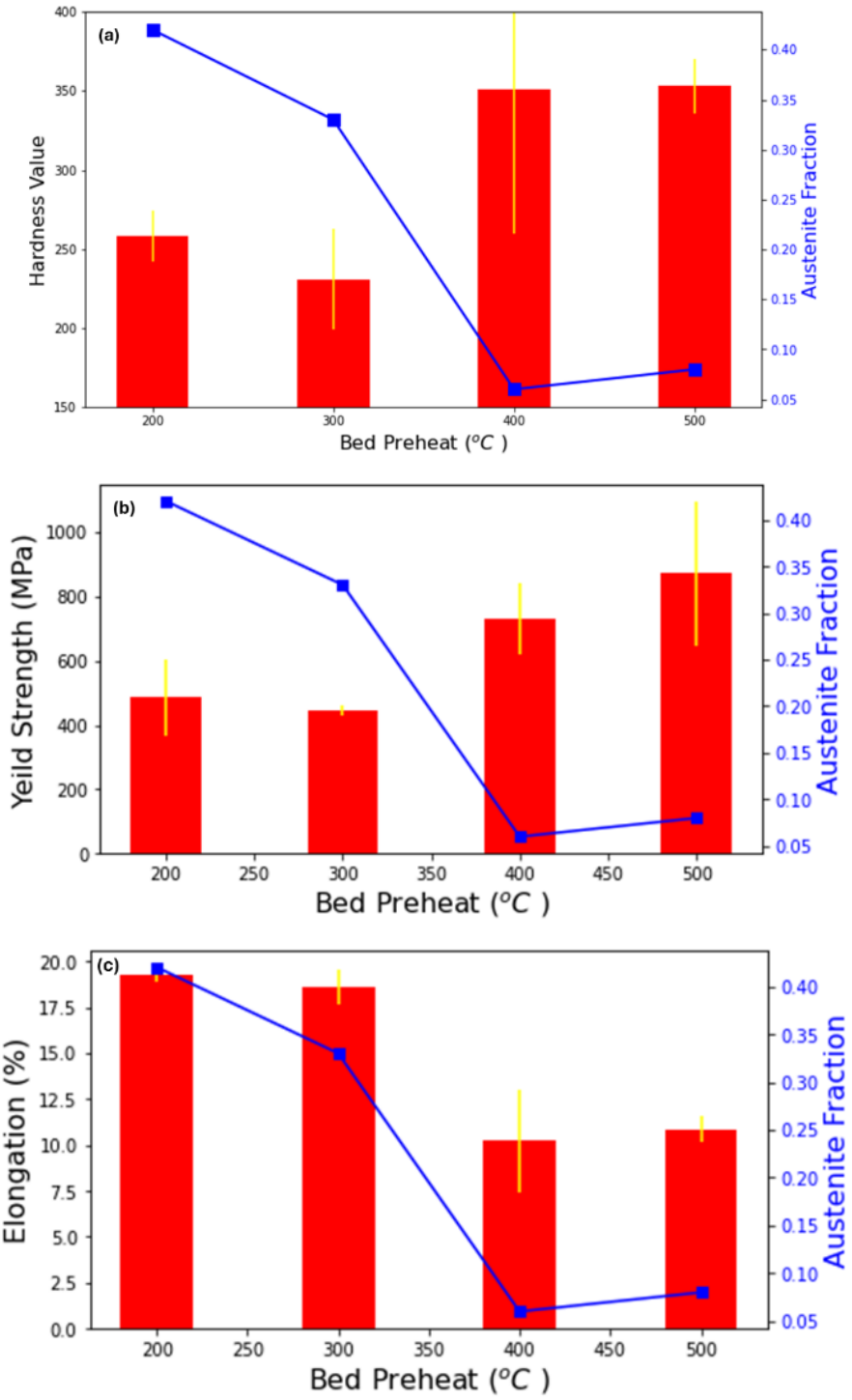



**Figure 4.17**Correlating preheating temperature with amount of retained austenite, and (a) hardness, (b) strength, and (c) ductility

Additionally, **Figure 4.18(a)- 4.18(d)** present the work hardening rate as a function of true strain for the defect-free samples built at different temperatures. While samples fabricated at the same temperature exhibit similar work hardening behavior, differences are observed in the

samples fabricated at different temperatures. Samples produced at lower temperatures, which contain a large amount of retained austenite, show an abnormal plastic deformation behavior that comprises three stages, which is similar to the TRIP steels. The increasing work hardening rate is indicative of a strain-induced γ → α' transformation that precedes the martensite yielding. Although such behavior has been previously reported for 17-4 PH SS, it has been primarily attributed to the powder chemical composition, specifically the powders with a low Creq/Nieq ratio or nitrogen atomized powders, which are conditions that also promote austenite stabilization [82], [101].

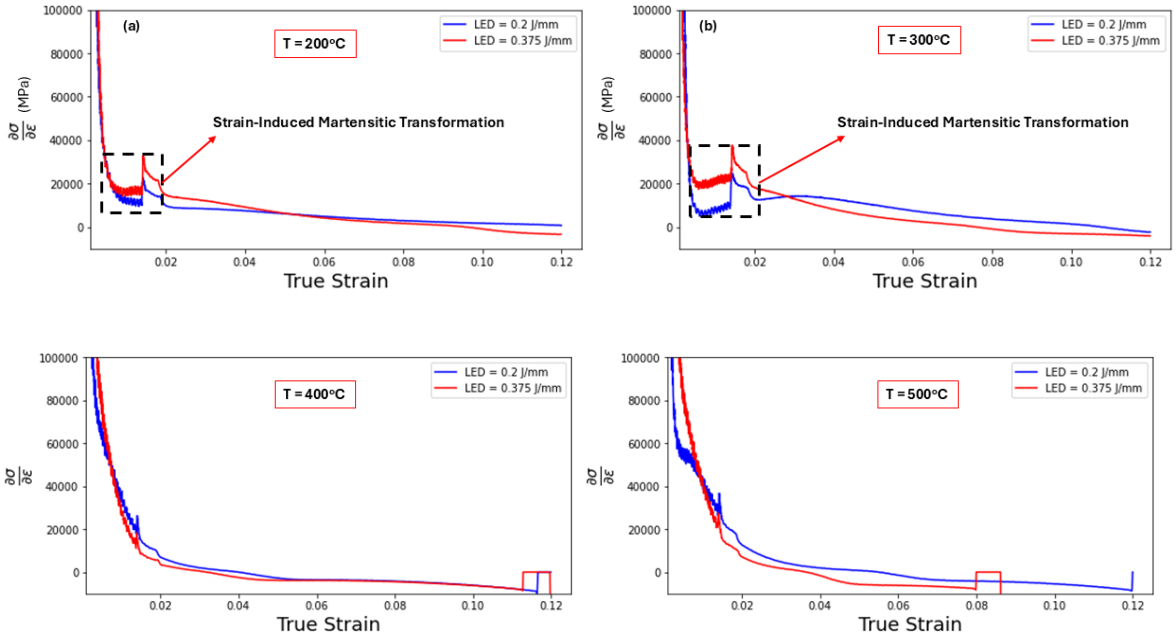



**Figure 4.18** Work hardening behaviour of the samples built at (a) 200°C, (b) 300°C, (c) 400°C, and 500°C

The results from the phase characterization provide a clear explanation for the observed variation in the mechanical properties. The samples lack copper precipitates, which explain for the lack of strength even in the samples that have the best performance. Furthermore, samples with a large amount of retained austenite exhibit additional reduction in strength and an increase in ductility, which are characteristics that directly correlate with the powder bed

preheating temperatures. Some samples also show an plastic deformation behaviour that comprises three stages, which is similar to that of TRIP steels. This suggests that, in the absence of manufacturing defects, the amount of retained austenite drives the variations in the mechanical properties. Since conditions that lead to higher cooling rates lead to more retained austenite, it is suggested that preheating the powder bed can minimize the austenite content, thus controlling the phase composition of the LPBF-manufactured 17-4 PH SS.

### 4.2.3 Summary of Mechanical Properties in As-built Condition

Hardness and tensile tests were conducted to investigate the influence of process parameters on the mechanical behaviour through the microstructure. When the effect of the manufacturing defects was analyzed, an unexpected variation in properties was observed even in the defect-free samples. To understand this variation, the phase composition was quantified and examined, which showed the key microstructural factors that drive the variation in mechanical performance.

The correlation between defect content and mechanical properties is evident, as the best-performing samples exhibit superior strength and ductility across all of the tested parameters. However, defect morphology alone does not appear to influence strength. Samples classified as having intermediate level of manufacturing defects exhibit distinct defect morphologies yet also show comparable strength. This observation aligns with previous findings in Ti-6Al-4V [107], [108] where the defect shape was found to be less critical than the number of manufacturing defects.

Interestingly, a large variation in the mechanical properties is observed in the absence of manufacturing defects. While the samples produced at a preheating temperature showed similar

performance, a large variation across the powder bed preheating temperature can be observed. This indicates that another microstructural variable affected by the temperature controls the mechanical response in the as-built state.

Microstructural characterisation across the powder bed preheating temperatures reveals a trend of excessive retention of δ-ferrite and austenite at lower temperatures, with the characteristics minimized as the temperature increases. This is attributed to a high cooling rate which leads to an incomplete ferrite-to-austenite phase, and austenite growth and stabilization via C/N enrichment during successive scans. Higher temperatures allows for the completion of the δ to γ phase transformation and uniform distribution of C/N, thus leading to a more complete austenite to martensite transformation when the build is cooled post-printing.

Additionally, the STEM investigation reveals no copper precipitation in the as-built state. This is once again attributed to the build plate preheating, which is done with a temperature higher than the Ms of the alloy. Since the martensitic phase is never subjected to thermal aging during the process, copper precipitates do not form, thus leading to a loss of strength.

Overall, the absence of copper precipitation and retention of austenite contribute to reduced strength and variability in the mechanical properties of the as-built material. These microstructural characteristics are directly influenced by the higher powder bed preheating temperature used during the printing process. The findings suggest that 17-4 PH SS in the as-built condition, particularly when fabricated with a higher temperature, is not suitable for direct industrial applications. Therefore, a post-build heat treatment tailored to achieve the desired phase composition is essential to ensure consistent and reliable mechanical performance.

## 4.3 Effect of Heat Treatment

In this study, an optimal process parameter range has been identified, which can produce samples with near-zero manufacturing defects. Mechanical testing confirms that samples printed within this optimal range have the best properties. However, while the ductility requirements are met, the strength falls significantly short of the levels required for industrial applications and exhibits a large variation. This deficiency is attributed to the absence of copper precipitates and presence of a large amount of retained austenite. Therefore, heat treatment is essential to enhance the mechanical performance of the printed material for use in the industry.

This section examines the impact of a standard heat treatment (Cond. A + H900) on LPBF-manufactured 17-4 PH SS. First, the phase changes that follow heat treatment is analyzed and compared to those in the as-built condition. Next, the mechanical properties of the heat-treated samples are evaluated, with comparisons drawn between the as-built state and standard performance expectations for the alloy.

### 4.3.1 Effect on Phases

**Figure 4.19** shows optical micrographs of samples built in the optimal window, along the build direction, after the full heat treatment. The samples show a similar grain structure that is indicative of tempered martensite. The structure was similar for all the samples built in the optimal window, thus indicating that the variations in grain structure induced by the process parameters are eliminated by a heat treatment.

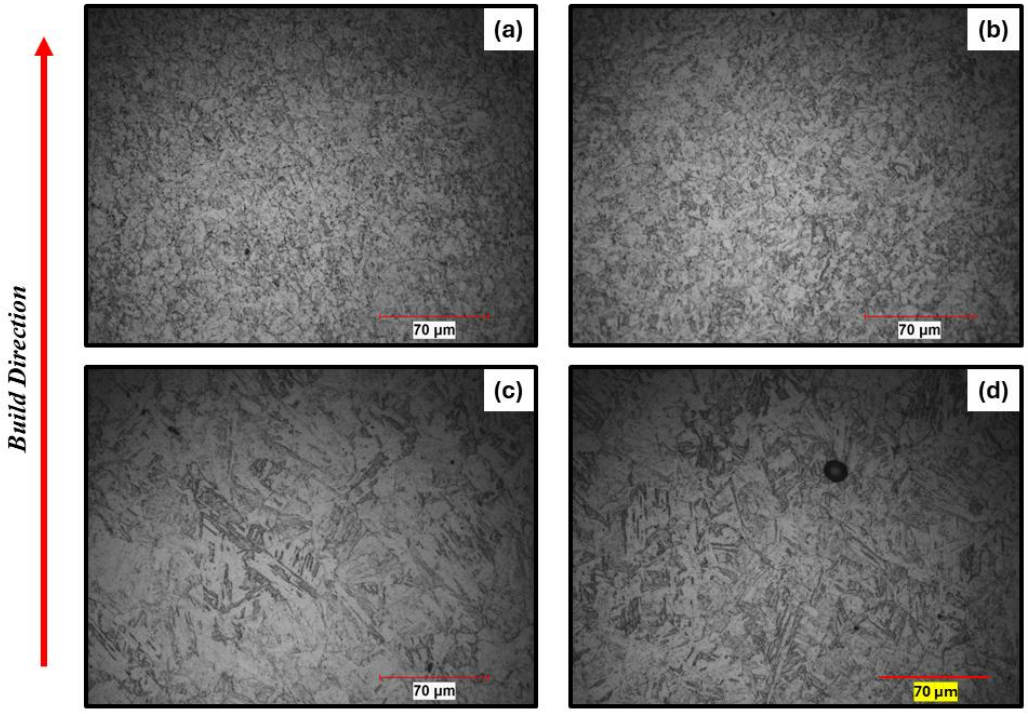



**Figure 4.19** Optical micrographs of heat-treated samples with different combinations of process parameters

The XRD patterns of the samples built at different temperatures are presented in **Figure 4.20 (a) – 4.20(d)** reveal a consistent phase transformation following the heat treatment. Across all of the samples, only a single dominant phase is observed, which corresponds to the BCC/BCT structure, and characteristic of conventionally produced and heat-treated treated 17-4 PH SS. This finding suggests that, regardless of the specific process parameters used during fabrication, the full heat treatment results in a nearly fully martensitic microstructure, thus ensuring uniformity across all builds.

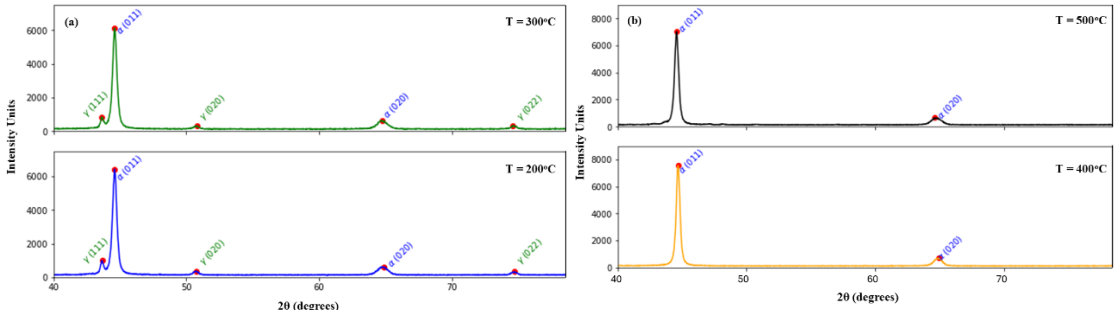



**Figure 4.20** X-ray diffraction patterns of samples built at (a) 200°C, 300°C, and (b) 400°C, 500°C in the fully heat-treated condition

To characterize the copper precipitation in the material post-heat treatment, STEM is utilized as shown in **Figure 4.21**. A uniform copper-rich cluster with an average size of 6.503 nm, i.e. smaller than the critical size of the system [109], is seen. Larger niobium (Nb)-rich precipitates are also observed. The identified copper-rich precipitates is the main strengthening phase for the 17-4 PH SS system and known to enhance the strength of the material through a shearing mechanism [57], [58], [110]. The Nb-rich cluster is a secondary strengthening phase that also contributes to the strengthening [110]. Overall, the phases are known to significantly enhance the strength of the material; however, these phases lead to a loss in ductility.

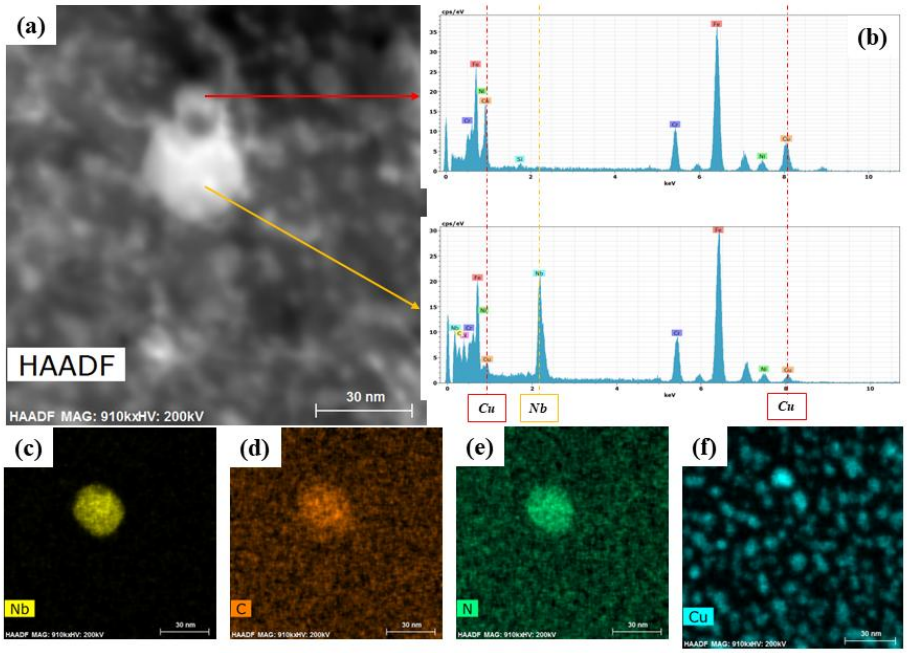



**Figure 4.21** STEM image of (a) heat-treated condition that shows spherical precipitates of two kinds (b) fine Cu-rich and Nb-rich precipitates, and the corresponding EDS maps (c) - (f)

### 4.3.2 Effect on Mechanical Properties

**Figure 4.22 (a)** presents the hardness of the samples built by using different process recipes within the optimal working range to show how heat treatment influences the mechanical properties through phase changes. The results show negligible variation in hardness among the samples, thus indicating that the phase composition differences, which govern the variations in the mechanical properties in the as-built samples with near-zero manufacturing defects, have been eliminated. **Figure 4.22 (b)** further compares the average hardness values, along with the error margins, of the heat-treated samples to the as-built samples. A significant increase in hardness is observed, with little variation across the samples. This suggests that heat treatment not only homogenizes the phase composition by eliminating the retained austenite but also induces the copper precipitates, irrespective of the recipe used for printing within the optimal range.

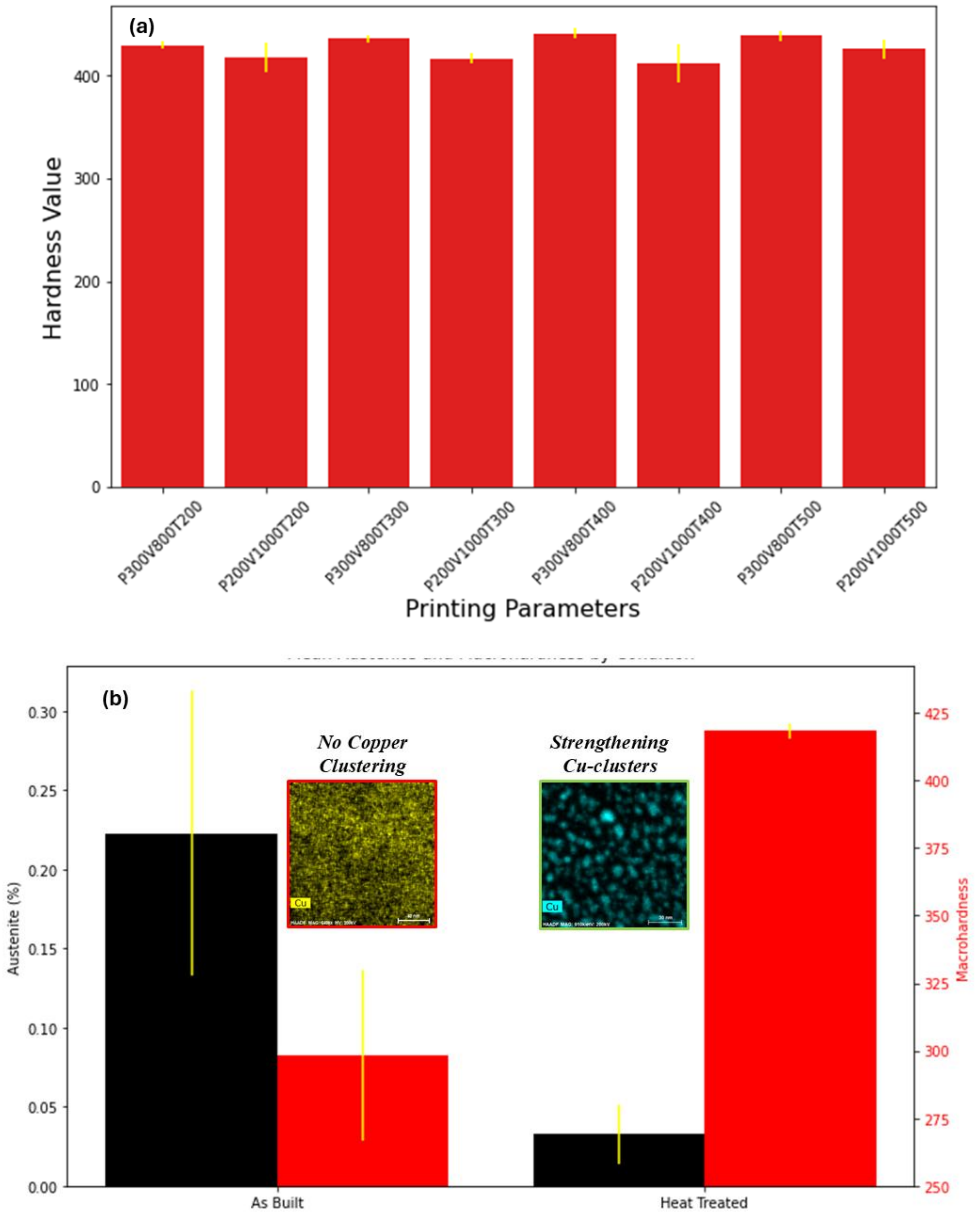



**Figure 4.22** Hardness of manufacturing defect free-samples built with (a) different processing conditions, after heat treatment and comparison with (b) as-built samples

**Figure 4.23** presents the results obtained from tensile testing after heat treatment. As expected, the ductility of all of the samples is reduced due to the formation of copper precipitates (**Figure 4.23(a)**). Despite the loss of ductility, the samples with the best performance still have an acceptable degree of ductility, while the samples that have an intermediate and poor performance fall short of the required threshold. Strength, on the other hand, is significantly enhanced for all samples, with samples that have both an intermediate and best performance meeting the standard strength requirements (**Figure 4.23(b)** and **4.23(c)**). Notably, the samples

with the best performance consistently outperform those in the other categories and achieve all of the expected tensile properties of 17-4 PH SS.

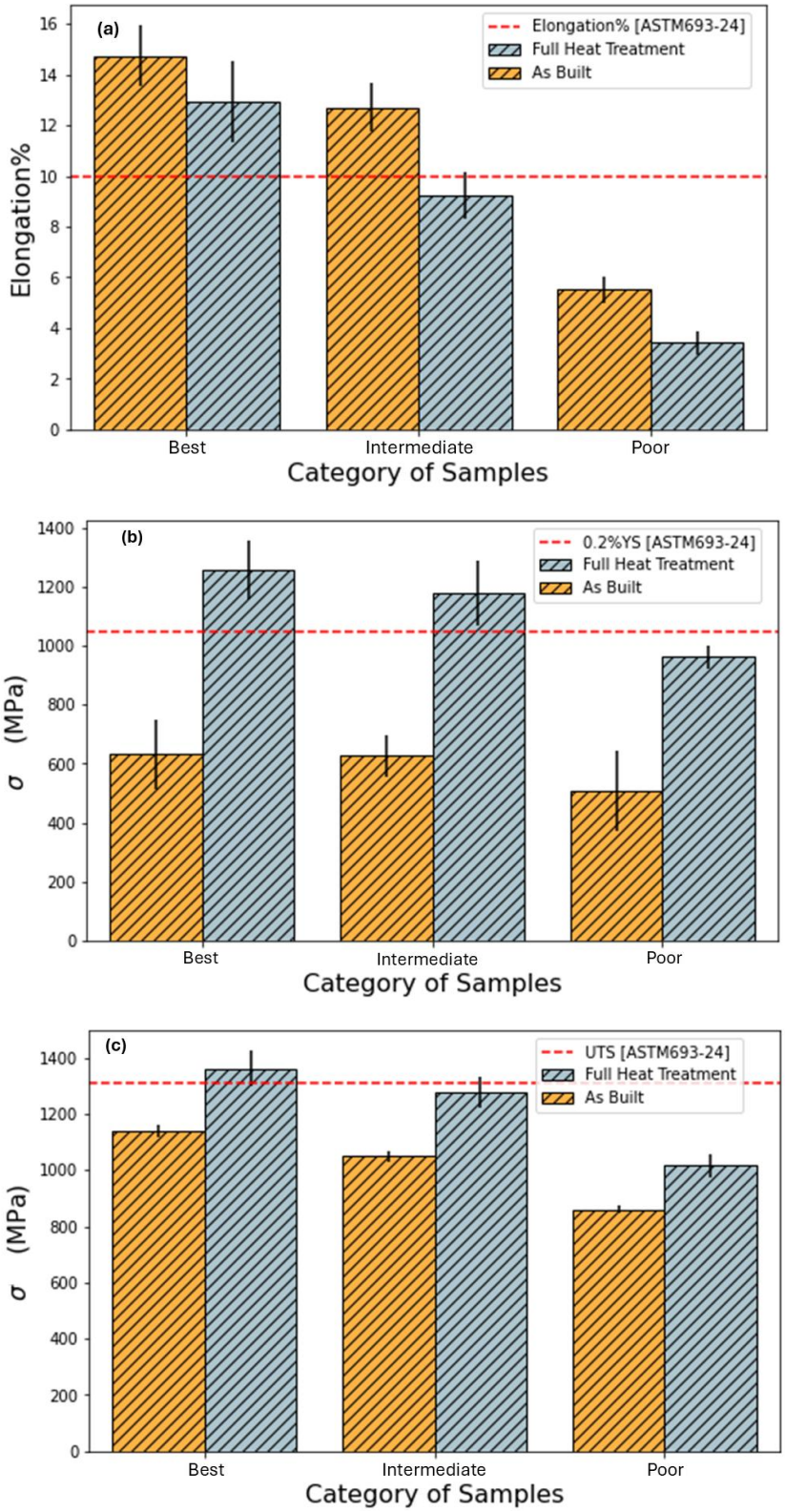



**Figure 4.23** Comparison of (a) elongation, (b) yield strength, and (c) UTS, of heat-treated samples, with the as-built samples and the standard expectations of the alloy

**Figure 4.24** presents the tensile properties after heat treatment for the samples which are compared with recent data in the literature [2], [3], [4], [5], [6], [64], [86], [103], [111], [112], [113], [114]. The data points are color-coded based on defect level and benchmarked against ASTM standard requirements for 17-4 PH SS. As evident, the samples produced within the identified optimal processing window, which have >99.5% density, consistently meet both the strength and ductility requirements specified by ASTM-A693-24. Some studies in the literature also report >99.5% density and meet the mechanical property criteria, however, these are relatively few and do not show the same consistency observed in the current work. The majority of previously reported samples exhibit intermediate defect levels and typically meet only the strength requirement, falling short of meeting the ductility requirements. This shows the ongoing challenge in producing defect-free 17-4 PH SS components via LPBF. The current work overcomes this challenge, primarily through the implementation of using powder bed preheating, which enhances process stability and microstructural control. Therefore, it is recommended that the fabrication of 17-4 PH SS via LPBF be carried out with powder bed preheating to reliably achieve high-quality and high-performance components.

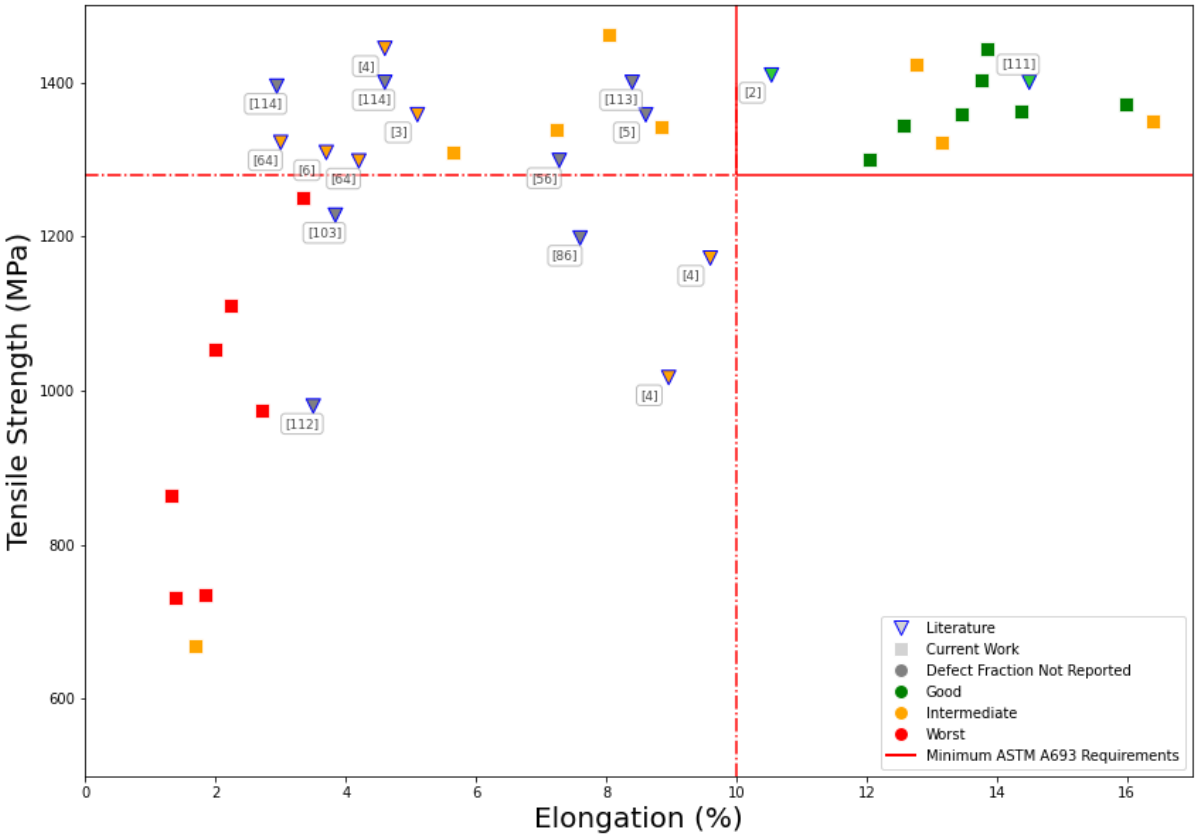



**Figure 4.24** Tensile properties of LPBF manufactured samples, following heat treatment procedures in literature, and current study, compared to ASTM standard requirements

### 4.3.3 Summary of Effect of Heat Treatment

To investigate the effect of heat treatment of LPBF-manufactured 17-4 PH SS, the samples were subjected to a standard heat treatment (Cond. A + H900). While all the samples were subjected to tensile and hardness testing after a heat treatment, the defect-free samples were also subjected to phase characterization. Heat treatment effectively eliminates excessive retained austenite, promotes copper clustering, and results in consistent hardness in defect-free samples. This indicates that, regardless of the initial processing conditions, the final mechanical properties are predominantly governed by the defect content, thus underscoring the critical influence of build quality on material performance.

Following heat treatment, all of the samples exhibit increased strength at the expense of ductility owing to copper precipitation. Under these conditions, only the highest-quality

samples, characterized by few manufacturing defects, consistently meet all the required mechanical property benchmarks, thus reinforcing the critical role of defect minimization in achieving acceptable performance for LPBF-manufactured 17-4 PH SS.

These findings represent a notable advancement in the LPBF processing of 17-4 PH SS, which overcomes the limitation of previous studies, which cannot achieve application-ready properties. The ability to meet strength and ductility requirements through optimized processing and heat treatment underscores the low defect tolerance of the material and the need for precise process control, which is enabled by preheating the build plate prior to printing in this work.

## 4.4 Summary of Results

This study sets out to systematically investigate the process-structure-property relationships in LPBF-manufactured 17-4 PH SS by focusing on three key aspects. First, the influence of the process parameters on formation of manufacturing defects is examined to identify an optimal processing window that minimizes manufacturing defects. Second, the mechanical properties of the as-built samples are analyzed by considering both the role of manufacturing defects and influence of phase composition. Finally, the effect of a standard heat treatment (Condition A + H900) is evaluated as it is widely reported in the literature that achieving the standard strength and ductility requirements for 17-4 PH SS through LPBF and subsequent heat treatment remains a challenge.

Optimizing process parameters is crucial for achieving defect-free builds with LPBF manufactured 17-4 PH SS. Both high laser power and low scanning speed, and low laser power and high scanning speed combinations lead to the formation of manufacturing defects. However, a moderate power-speed combination results in a near-zero defect condition,

characterized by a workable LED range. Additionally, preheating the build plate significantly expands this workable range, thus promoting a more stable process. This improvement is attributed to smoother thermal gradients, which result from the enhanced thermal conductivity of the material at higher preheating temperatures.

The results from the tensile and hardness testing show that the defect fraction is the primary factor that affects the mechanical properties; the morphology of these manufacturing defects appears to have less impact. Interestingly, even in the absence of manufacturing defects, there is still a large variation in mechanical performance, with an underwhelming strength and higher ductility. This is attributed to increased austenite retention in some of the samples and the absence of copper-rich precipitates, which are essential for strengthening. Both of these factors are driven by preheating the build plate. Owing to these, none of the samples meet the required strength criteria for industrial applications in their as-built state, thus highlighting the need for a post-build heat treatment.

Heat treatment promotes the formation of copper-rich precipitates and eliminates phase variations, thus resulting in uniform hardness with the absence of manufacturing defects. The treatment significantly enhances the strength of the samples; however, it comes at the cost of reduced ductility. In this condition, only the samples built within the identified optimal range meet both strength and ductility benchmarks, while samples with an intermediate performance achieve the required strength but fall short of the ductility due to a higher defect content.

This study shows that additively manufactured 17-4 PH SS can achieve application-compliant mechanical properties when processed within an optimized parameter range and subjected to a standard heat treatment, thus addressing a key challenge reported in the literature. The findings highlight the low defect tolerance of the material, thus emphasizing the need for precise process control. In this work, precise control is established by build-plate preheating, which serves as

a crucial factor in defect reduction, with higher preheating temperatures expanding the workable LED window for creating defect-free builds. These insights contribute to the broader understanding of process-structure-property relationships in the LPBF of 17-4 PH SS, thus offering a strategic pathway for optimizing mechanical performance in high-reliability applications.

# Chapter 5: Conclusions

The major conclusions drawn from this work are as follows.

## 5.1 Effect of Process Parameters on Formation of Manufacturing Defects

1. The formation of manufacturing defects in additively manufactured 17-4 PH SS is very dependent on the laser power and scanning speed combination. Both high scanning speed and low laser power and low scanning speed and high laser power conditions result in the formation of manufacturing defects, thus emphasizing the need for printing in a defined process window. This window can be quantitatively characterized by a specific range of LEDs, which serves as a key parameter for minimizing manufacturing defects and ensuring consistent integrity of builds.
2. A low laser power, high scanning speed processing regime leads to insufficient powder melting, thus resulting in irregularly shaped manufacturing defects that predominantly form in regions with partial melt pool overlap. In contrast, a low scanning speed, high laser power combination induces fluid flow instabilities, thus leading to the formation of large, circular manufacturing defects that negatively impact the structural integrity of the build.
3. Higher powder bed preheating temperatures enhance the workable LED range by increasing the thermal conductivity of the material. This leads to a smoother thermal gradient and complete weld pool overlap. While previously predicted through numerical simulations and single-track experiments, this study provides the first full-build experimental validation, thus showing the effectiveness of preheating in process stabilization and defect mitigation in LPBF of 17-4 PH SS.

## 5.2 Mechanical Behaviour of As-built Samples

1. The mechanical behaviour of the as-built 17-4 PH SS is primarily governed by the defect content, with higher-quality samples exhibiting superior performance, followed by the intermediate and lower-quality samples. In contrast, defect morphology has a minimal influence on mechanical properties, thus indicating that the number of manufacturing defects is the dominant factor in determining material performance.
2. Even in the absence of manufacturing defects, significant variations in mechanical behaviour persist, primarily driven by enhanced austenite retention, which is largely influenced by powder bed preheating.
3. Despite achieving near-zero defect content and superior mechanical performance, the strength of the as-built samples remains significantly lower than the expected values for 17-4 PH SS. This deficiency is primarily attributed to the absence of copper-rich precipitates in the as-built condition, further exacerbated by austenite retention, both of which inhibit the potential of the alloy to reach full-strength.

## 5.3 Effect of Heat Treatment

1. A standard heat treatment (Condition A + H900) effectively eliminates excessive retained austenite while promoting the formation of nano-scale copper-rich precipitates. This results in significantly enhanced and uniform hardness in samples with near-zero manufacturing defects.
2. All of the samples exhibit increased strength and less ductility following heat treatment, which is attributed to copper precipitation. However, only those with near-zero manufacturing defects show acceptable levels of strength and ductility, thus highlighting the critical role of defect minimization in achieving the required mechanical properties.

3. All of the samples processed within the identified optimal working range meet the requirements specified by ASTM A-693-24 for industrial applications. This represents a significant advancement over the results in the existing literature, where previous studies have not been able to produce 17-4 PH SS components via LPBF that meet the necessary performance standards.

# Chapter 6: Recommendations for Future Work

The results of this study show that, for LPBF, optimizing the process parameters to achieve < 0.5% defect content, followed by a conventional heat treatment, results in a consistent and favourable mechanical performance of 17-4 PH SS. However, further research is needed to address the limitations of this study, which are outlined as follows:

- Tensile testing is conducted only in the perpendicular direction to the build orientation.
- Only a single powder lot is utilized for the fabrication of the components.
- All of the samples are built in an Ar atmosphere
- The focus is only on quasi-static tensile tests, without considering other loading conditions.

It is well-established that LPBF-manufactured 17-4 PH SS exhibits anisotropy, potentially leading to varying performance across different testing directions, even after heat treatment. Even though some studies have tested 17-4 PH SS in multiple directions, these studies generally involve defect tolerances that exceed 1%, with the material failing to meet the desired performance criteria in any orientation. Consequently, a comprehensive study is needed to investigate the impact of near-zero defect content on the material performance across various testing orientations.

17-4 PH SS is an SS with a martensitic finishing temperature that is fairly close to room temperature (~32$^{o}$C), and any changes in the powder chemical composition can have a significant impact in determining the final phase composition in both the as-built and heat-treated conditions. Therefore, studies that investigate the validity of the current findings over powders with different chemical compositions, quantified by the $Cr_{eq}/Ni_{eq}$ ratio, are required.

Another factor that may influence the response of 17-4 PH SS to commercial heat treatment is the build atmosphere. In this study, all builds are conducted in an Ar atmosphere, while N atmospheres are also commonly used in LPBF processes. For 17-4 PH SS, builds performed in an N atmosphere may enhance austenite stability, thus potentially inhibiting the precipitation of copper during heat treatment. Therefore, further investigation is needed to evaluate the impact of the build atmosphere on the properties and performance of the material, especially when the samples are printed at a higher powder bed preheating temperature.

Finally, the mode of loading, including torsion, shear, high strain rate, and fatigue, may result in different material responses depending on the defect levels. Therefore, further studies need to investigate the applicability of the current findings under these diverse loading conditions.

# References


[1] S. Yan *et al.*, “In Situ Characterization of 17-4PH Stainless Steel by Small-Angle Neutron Scattering,” *Materials*, vol. 16, no. 16, p. 5583, Aug. 2023, doi: 10.3390/ma16165583.

[2] A. Yadollahi, N. Shamsaei, S. M. Thompson, A. Elwany, and L. Bian, “Effects of building orientation and heat treatment on fatigue behavior of selective laser melted 17-4 PH stainless steel,” *Int. J. Fatigue*, vol. 94, pp. 218–235, Jan. 2017, doi: 10.1016/j.ijfatigue.2016.03.014.

[3] S. Pasebani, M. Ghayoor, S. Badwe, H. Irrinki, and S. V. Atre, “Effects of atomizing media and post processing on mechanical properties of 17-4 PH stainless steel manufactured via selective laser melting,” *Addit. Manuf.*, vol. 22, pp. 127–137, 2018.

[4] T. LeBrun, T. Nakamoto, K. Horikawa, and H. Kobayashi, “Effect of retained austenite on subsequent thermal processing and resultant mechanical properties of selective laser melted 17–4 PH stainless steel,” *Mater. Des.*, vol. 81, pp. 44–53, Sep. 2015, doi: 10.1016/j.matdes.2015.05.026.

[5] D. J. Shaffer, A. E. Wilson-Heid, J. S. Keist, A. M. Beese, and T. A. Palmer, “Impact of retained austenite on the aging response of additively manufactured 17-4 PH grade stainless steel,” *Mater. Sci. Eng. A*, vol. 817, p. 141363, Jun. 2021, doi: 10.1016/j.msea.2021.141363.

[6] S. E. Kovacs *et al.*, “Additive Manufacturing of 17-4PH Alloy: Tailoring the Printing Orientation for Enhanced Aerospace Application Performance,” *Aerospace*, vol. 10, no. 7, p. 619, 2023.

[7] S.-M. Yeon *et al.*, “Normalizing Effect of Heat Treatment Processing on 17-4 PH Stainless Steel Manufactured by Powder Bed Fusion,” *Metals*, vol. 12, no. 5, Art. no. 5, May 2022, doi: 10.3390/met12050704.

[8] M. S. Moyle *et al.*, “Effect of compositional variations on the heat treatment response in 17-4 PH stainless steel fabricated by laser powder bed fusion,” *Mater. Charact.*, p. 113768, 2024.

[9] ASTM International, *ASTM F2792-12- Standard Terminology for Additive Manufacturing Technologies*, F2792-12, West Conshohocken, PA, United States., Mar. 21, 2012. doi: 10.1520/F2792-12.

[10] A. Vafadar, F. Guzzomi, A. Rassau, and K. Hayward, “Advances in Metal Additive Manufacturing: A Review of Common Processes, Industrial Applications, and Current Challenges,” *Appl. Sci.*, vol. 11, no. 3, Art. no. 3, Jan. 2021, doi: 10.3390/app11031213.

[11] S. Chowdhury *et al.*, “Laser powder bed fusion: a state-of-the-art review of the technology, materials, properties & defects, and numerical modelling,” *J. Mater. Res. Technol.*, vol. 20, pp. 2109–2172, 2022.

[12] S. R. Narasimharaju *et al.*, “A comprehensive review on laser powder bed fusion of steels: Processing, microstructure, defects and control methods, mechanical properties, current challenges and future trends,” *J. Manuf. Process.*, vol. 75, pp. 375–414, Mar. 2022, doi: 10.1016/j.jmapro.2021.12.033.

[13] T. Mukherjee, J. S. Zuback, A. De, and T. DebRoy, “Printability of alloys for additive manufacturing,” *Sci. Rep.*, vol. 6, no. 1, p. 19717, Jan. 2016, doi: 10.1038/srep19717.

[14] J. Wang *et al.*, “Improvement of densification and microstructure of ASTM A131 EH36 steel samples additively manufactured via selective laser melting with varying laser scanning speed and hatch spacing,” *Mater. Sci. Eng. A*, vol. 746, pp. 300–313, Feb. 2019, doi: 10.1016/j.msea.2019.01.019.

[15] S. Shrestha and K. Chou, “Formation of keyhole and lack of fusion pores during the laser powder bed fusion process,” *Manuf. Lett.*, vol. 32, pp. 19–23, Apr. 2022, doi: 10.1016/j.mfglet.2022.01.005.
[16] Y. Kaynak and O. Kitay, “Porosity, Surface Quality, Microhardness and Microstructure of Selective Laser Melted 316L Stainless Steel Resulting from Finish Machining,” *J. Manuf. Mater. Process.*, vol. 2, no. 2, Art. no. 2, Jun. 2018, doi: 10.3390/jmmp2020036.
[17] L. Guo *et al.*, “Understanding keyhole induced-porosities in laser powder bed fusion of aluminum and elimination strategy,” *Int. J. Mach. Tools Manuf.*, vol. 184, p. 103977, Jan. 2023, doi: 10.1016/j.ijmachtools.2022.103977.
[18] A. M. Kiss *et al.*, “Laser-Induced Keyhole Defect Dynamics during Metal Additive Manufacturing,” *Adv. Eng. Mater.*, vol. 21, no. 10, p. 1900455, 2019, doi: 10.1002/adem.201900455.
[19] Q. Guo *et al.*, “Revealing melt flow instabilities in laser powder bed fusion additive manufacturing of aluminum alloy via in-situ high-speed X-ray imaging,” *Int. J. Mach. Tools Manuf.*, vol. 175, p. 103861, Apr. 2022, doi: 10.1016/j.ijmachtools.2022.103861.
[20] S. Bergmueller, L. Gerhold, L. Fuchs, L. Kaserer, and G. Leichtfried, “Systematic approach to process parameter optimization for laser powder bed fusion of low-alloy steel based on melting modes,” *Int. J. Adv. Manuf. Technol.*, vol. 126, no. 9, pp. 4385–4398, Jun. 2023, doi: 10.1007/s00170-023-11377-2.
[21] P. Ferro, R. Meneghello, G. Savio, and F. Berto, “A modified volumetric energy density–based approach for porosity assessment in additive manufacturing process design,” *Int. J. Adv. Manuf. Technol.*, vol. 110, no. 7–8, pp. 1911–1921, Sep. 2020, doi: 10.1007/s00170-020-05949-9.
[22] V. Lindström, G. Lupo, J. Yang, V. Turlo, and C. Leinenbach, “A simple scaling model for balling defect formation during laser powder bed fusion,” *Addit. Manuf.*, vol. 63, p. 103431, Feb. 2023, doi: 10.1016/j.addma.2023.103431.
[23] D. Gu and Y. Shen, “Balling phenomena during direct laser sintering of multi-component Cu-based metal powder,” *J. Alloys Compd.*, vol. 432, no. 1–2, pp. 163–166, 2007.
[24] R. Li, J. Liu, Y. Shi, L. Wang, and W. Jiang, “Balling behavior of stainless steel and nickel powder during selective laser melting process,” *Int. J. Adv. Manuf. Technol.*, vol. 59, no. 9–12, pp. 1025–1035, Apr. 2012, doi: 10.1007/s00170-011-3566-1.
[25] W. King, A. T. Anderson, R. M. Ferencz, N. E. Hodge, C. Kamath, and S. A. Khairallah, “Overview of modelling and simulation of metal powder bed fusion process at Lawrence Livermore National Laboratory,” *Mater. Sci. Technol.*, vol. 31, no. 8, pp. 957–968, Jun. 2015, doi: 10.1179/1743284714Y.0000000728.
[26] F. Klocke and C. Wagner, “Coalescence behaviour of two metallic particles as base mechanism of selective laser sintering,” *CIRP Ann.*, vol. 52, no. 1, pp. 177–180, 2003.
[27] J. Li, X. Zhang, F. Ma, S. Wang, and Y. Huang, “Simultaneous Pore Detection and Morphological Features Extraction in Laser Powder Bed Fusion with Image Processing,” *Materials*, vol. 17, no. 6, Art. no. 6, Jan. 2024, doi: 10.3390/ma17061373.
[28] S. D. Dobson and T. L. Starr, “Powder characterization and part density for powder bed fusion of 17-4 PH stainless steel,” *Rapid Prototyp. J.*, vol. 27, no. 1, pp. 53–58, 2021, doi: 10.1108/RPJ-01-2020-0023.
[29] S. Sinha and T. Mukherjee, “Mitigation of Gas Porosity in Additive Manufacturing Using Experimental Data Analysis and Mechanistic Modeling,” *Materials*, vol. 17, no. 7, Art. no. 7, Jan. 2024, doi: 10.3390/ma17071569.
[30] J. Jakumeit, C. Huang, R. Laqua, J. Zielinski, and J. H. Schleifenbaum, “Effect of evaporated gas flow on porosity and microstructure of IN718 parts produced by LPBF-processes,” *IOP Conf. Ser. Mater. Sci. Eng.*, vol. 861, no. 1, p. 012011, May 2020, doi: 10.1088/1757-899X/861/1/012011.

[31] Q. Jia and D. Gu, “Selective laser melting additive manufactured Inconel 718 superalloy parts: High-temperature oxidation property and its mechanisms,” *Opt. Laser Technol.*, vol. 62, pp. 161–171, 2014.
[32] J. Krell, A. Röttger, K. Geenen, and W. Theisen, “General investigations on processing tool steel X40CrMoV5-1 with selective laser melting,” *J. Mater. Process. Technol.*, vol. 255, pp. 679–688, 2018.
[33] M. Simonelli *et al.*, “A Study on the Laser Spatter and the Oxidation Reactions During Selective Laser Melting of 316L Stainless Steel, Al-Si10-Mg, and Ti-6Al-4V,” *Metall. Mater. Trans. A*, vol. 46, no. 9, pp. 3842–3851, Sep. 2015, doi: 10.1007/s11661-015-2882-8.
[34] M. Yakout, M. A. Elbestawi, and S. C. Veldhuis, “A study of thermal expansion coefficients and microstructure during selective laser melting of Invar 36 and stainless steel 316L,” *Addit. Manuf.*, vol. 24, pp. 405–418, 2018.
[35] Q. Guo *et al.*, “Transient dynamics of powder spattering in laser powder bed fusion additive manufacturing process revealed by in-situ high-speed high-energy x-ray imaging,” *Acta Mater.*, vol. 151, pp. 169–180, 2018.
[36] X. Zhang, H. Zheng, and W. Yu, “A review on solidification cracks in high-strength aluminum alloys via laser powder bed fusion,” *Mater. Today Proc.*, vol. 70, pp. 465–469, Jan. 2022, doi: 10.1016/j.matpr.2022.09.366.
[37] M. Hafezi *et al.*, “Investigating crack formation in IN738LC Ni-based superalloy fabricated by laser powder-bed fusion process,” *J. Mater. Res. Technol.*, vol. 29, pp. 1983–2002, Mar. 2024, doi: 10.1016/j.jmrt.2024.01.264.
[38] M. Vilanova, M. C. Taboada, A. Martinez-Amesti, A. Niklas, M. San Sebastian, and T. Guraya, “Influence of Minor Alloying Element Additions on the Crack Susceptibility of a Nickel Based Superalloy Manufactured by LPBF,” *Materials*, vol. 14, no. 19, Art. no. 19, Jan. 2021, doi: 10.3390/ma14195702.
[39] D. Rosenthal, “The theory of moving sources of heat and its application to metal treatments,” *Trans. Am. Soc. Mech. Eng.*, vol. 68, no. 8, pp. 849–865, 1946.
[40] M. F. Ashby and K. E. Easterling, “A first report on diagrams for grain growth in welds,” *Acta Metall.*, vol. 30, no. 11, pp. 1969–1978, Nov. 1982, doi: 10.1016/0001-6160(82)90100-6.
[41] T. Mukherjee, H. L. Wei, A. De, and T. DebRoy, “Heat and fluid flow in additive manufacturing – Part II: Powder bed fusion of stainless steel, and titanium, nickel and aluminum base alloys,” *Comput. Mater. Sci.*, vol. 150, pp. 369–380, Jul. 2018, doi: 10.1016/j.commatsci.2018.04.027.
[42] S. Karna *et al.*, “Microstructural analysis and defect characterization of additively manufactured AA6061 aluminum alloy via laser powder bed fusion,” *J. Mater. Sci. Technol.*, Sep. 2024, doi: 10.1016/j.jmst.2024.08.056.
[43] J. V. Gordon *et al.*, “Defect structure process maps for laser powder bed fusion additive manufacturing,” *Addit. Manuf.*, vol. 36, p. 101552, Dec. 2020, doi: 10.1016/j.addma.2020.101552.
[44] J. A. Cherry, H. M. Davies, S. Mehmood, N. P. Lavery, S. G. R. Brown, and J. Sienz, “Investigation into the effect of process parameters on microstructural and physical properties of 316L stainless steel parts by selective laser melting,” *Int. J. Adv. Manuf. Technol.*, vol. 76, no. 5, pp. 869–879, Feb. 2015, doi: 10.1007/s00170-014-6297-2.
[45] M. Mansouri, M. M. Fallah, and A. Kazerooni, “The influence of hatch distance on the surface roughness, microhardness, residual stress, and density of inconel 625 specimens in the laser powder bed fusion process,” *Adv. Mater. Process. Technol.*, vol. 11, no. 2, pp. 641–655, Apr. 2025, doi: 10.1080/2374068x.2024.2313280.

[46] Z. Hu, H. Zhu, H. Zhang, and X. Zeng, “Experimental investigation on selective laser melting of 17-4PH stainless steel,” *Opt. Laser Technol.*, vol. 87, pp. 17–25, 2017.
[47] W. Wang *et al.*, “Processing defect, microstructure evolution and mechanical properties of laser powder bed fusion Al-12Si alloys,” *J. Mater. Res. Technol.*, vol. 26, pp. 681–696, Sep. 2023, doi: 10.1016/j.jmrt.2023.07.231.
[48] M. Liu, K. Wei, and X. Zeng, “High power laser powder bed fusion of AlSi10Mg alloy: Effect of layer thickness on defect, microstructure and mechanical property,” *Mater. Sci. Eng. A*, vol. 842, p. 143107, May 2022, doi: 10.1016/j.msea.2022.143107.
[49] H. C. Hyer and C. M. Petrie, “Effect of powder layer thickness on the microstructural development of additively manufactured SS316,” *J. Manuf. Process.*, vol. 76, pp. 666–674, Apr. 2022, doi: 10.1016/j.jmapro.2022.02.047.
[50] M. Badrossamay, A. Rezaei, E. Foroozmehr, A. Maleki, and A. Foroozmehr, “Effects of increasing powder layer thickness on the microstructure, mechanical properties, and failure mechanism of IN718 superalloy fabricated by laser powder bed fusion,” *Int. J. Adv. Manuf. Technol.*, vol. 118, no. 5, pp. 1703–1717, Jan. 2022, doi: 10.1007/s00170-021-07719-7.
[51] J. Wu *et al.*, “Influence of scanning strategies on microstructure and mechanical properties of laser powder bed fusion 2195 Al-Li alloy,” *J. Alloys Compd.*, vol. 1004, p. 175841, 2024.
[52] H. Chen *et al.*, “Role of laser scan strategies in defect control, microstructural evolution and mechanical properties of steel matrix composites prepared by laser additive manufacturing,” *Int. J. Miner. Metall. Mater.*, vol. 28, no. 3, pp. 462–474, Mar. 2021, doi: 10.1007/s12613-020-2133-x.
[53] S. Qin *et al.*, “Influence of Preheating Temperature on Microstructure Evolution and Hardness of High-Speed Steel AISI M50 Processed by Laser Powder Bed Fusion,” *Steel Res. Int.*, vol. 94, no. 6, p. 2200784, Jun. 2023, doi: 10.1002/srin.202200784.
[54] L. Caprio, A. G. Demir, G. Chiari, and B. Previtali, “Defect-free laser powder bed fusion of Ti–48Al–2Cr–2Nb with a high temperature inductive preheating system,” *J. Phys. Photonics*, vol. 2, no. 2, p. 024001, Feb. 2020, doi: 10.1088/2515-7647/ab7080.
[55] Q. Chen *et al.*, “Elucidating the effect of preheating temperature on melt pool morphology variation in Inconel 718 laser powder bed fusion via simulation and experiment,” *Addit. Manuf.*, vol. 37, no. C, Nov. 2020, doi: 10.1016/j.addma.2020.101642.
[56] S. Sabooni *et al.*, “Laser powder bed fusion of 17–4 PH stainless steel: A comparative study on the effect of heat treatment on the microstructure evolution and mechanical properties,” *Addit. Manuf.*, vol. 46, p. 102176, 2021.
[57] M. Murayama, K. Hono, and Y. Katayama, “Microstructural evolution in a 17-4 PH stainless steel after aging at 400 °C,” *Metall. Mater. Trans. A*, vol. 30, pp. 345–353, Feb. 1999, doi: 10.1007/s11661-999-0323-2.
[58] R. Monzen, M. L. Jenkins, and A. P. Sutton, “The bcc-to-9R martensitic transformation of Cu precipitates and the relaxation process of elastic strains in an Fe-Cu alloy,” *Philos. Mag. A*, vol. 80, no. 3, pp. 711–723, Mar. 2000, doi: 10.1080/01418610008212077.
[59] W. Jun, Z. Hong, C. Li, P. Yanhua, Q. Shaoyu, and S. Baoluo, “The microstructure evolution of type 17-4PH stainless steel during long-term aging at 350 deg. C,” *Nucl. Eng. Des.*, vol. 236, 2006, Accessed: Feb. 20, 2025. [Online]. Available: https://www.osti.gov/etdeweb/biblio/20845583
[60] S. A. Habib, S. P. Mates, F. Zhang, M. R. Stoudt, J. S. Zuback, and O. Borkiewicz, “Effect of austenite fraction and stability on strength-hardening-ductility in additively manufactured 17-4 PH stainless steel containing nitrogen,” *Mater. Sci. Eng. A*, vol. 878, p. 145180, 2023.

[61] P. Bajaj, A. Hariharan, A. Kini, P. Kürnsteiner, D. Raabe, and E. A. Jägle, “Steels in additive manufacturing: A review of their microstructure and properties,” *Mater. Sci. Eng. A*, vol. 772, p. 138633, Jan. 2020, doi: 10.1016/j.msea.2019.138633.
[62] T. DebRoy *et al.*, “Additive manufacturing of metallic components–process, structure and properties,” *Prog. Mater. Sci.*, vol. 92, pp. 112–224, 2018.
[63] A. A. Adeyemi, E. T. Akinlabi, R. M. Mahamood, K. O. Sanusi, S. Pityana, and M. Tlotleng, “Influence of laser power on microstructure of laser metal deposited 17-4 ph stainless steel,” in *IOP Conference Series: Materials Science and Engineering*, IOP Publishing, 2017, p. 012028. Accessed: Feb. 18, 2025. [Online]. Available: https://iopscience.iop.org/article/10.1088/1757-899X/225/1/012028/meta
[64] S. Asapu, R. K. Y, A. Gupta, and S. K. Jha, “Microstructural and Mechanical Characterization of Selective Laser Melted 17-4 PH Stainless Steel: Effect of Laser Scan Strategy and Heat Treatment,” *J. Mater. Eng. Perform.*, Apr. 2024, doi: 10.1007/s11665-024-09470-y.
[65] K. K. Singh and A. Moridi, “Metastability mediated grain size control in PH 17-4 stainless steel fabricated using Laser-Powder Bed Fusion (LPBF),” *Materialia*, vol. 30, p. 101857, 2023.
[66] H. Irrinki *et al.*, “Effects of powder characteristics and processing conditions on the corrosion performance of 17-4 PH stainless steel fabricated by laser-powder bed fusion,” *Prog. Addit. Manuf.*, vol. 3, no. 1, pp. 39–49, Jun. 2018, doi: 10.1007/s40964-018-0048-0.
[67] J. S. Weaver *et al.*, “The effects of particle size distribution on the rheological properties of the powder and the mechanical properties of additively manufactured 17-4 PH stainless steel,” *Addit. Manuf.*, vol. 39, p. 101851, 2021.
[68] F. Qin *et al.*, “Influence of powder particle size distribution on microstructure and mechanical properties of 17-4 PH stainless steel fabricated by selective laser melting,” *J. Mater. Res. Technol.*, 2023.
[69] J. W. Simmons, “Overview: high-nitrogen alloying of stainless steels,” *Mater. Sci. Eng. A*, vol. 207, no. 2, pp. 159–169, 1996.
[70] B. Brown, J. Newkirk, and F. Liou, “Absorption of Nitrogen during Pulsed Wave L-PBF of 17-4 PH Steel,” *Materials*, vol. 14, no. 3, p. 560, 2021.
[71] T.-H. Hsu *et al.*, “Effect of processing parameters on the fractions of martensite in 17-4 PH stainless steel fabricated by selective laser melting,” *J. Alloys Compd.*, vol. 859, p. 157758, Apr. 2021, doi: 10.1016/j.jallcom.2020.157758.
[72] E. Yasa, İ. Atik, and İ. Kandemir, “Material-specific phenomena and developing higher yield process parameters in laser powder bed fusion of 17-4 PH stainless steel,” *J. Braz. Soc. Mech. Sci. Eng.*, vol. 45, no. 1, p. 38, Dec. 2022, doi: 10.1007/s40430-022-03946-5.
[73] N. W. Makoana, I. Yadroitsava, H. Möller, and I. Yadroitsev, “Characterization of 17-4PH Single Tracks Produced at Different Parametric Conditions towards Increased Productivity of LPBF Systems—The Effect of Laser Power and Spot Size Upscaling,” *Metals*, vol. 8, no. 7, Art. no. 7, Jul. 2018, doi: 10.3390/met8070475.
[74] D. Sarker *et al.*, “Influence of Pore Formation and Its Role on the Tensile Properties of 17-4 PH Stainless Steel Fabricated by Laser Powder Bed Fusion,” in *TMS 2021 150th Annual Meeting & Exhibition Supplemental Proceedings*, in The Minerals, Metals & Materials Series. Cham: Springer International Publishing, 2021, pp. 131–141. doi: 10.1007/978-3-030-65261-6_12.
[75] X. Wang and K. Chou, “Effects of thermal cycles on the microstructure evolution of Inconel 718 during selective laser melting process,” *Addit. Manuf.*, vol. 18, pp. 1–14, Dec. 2017, doi: 10.1016/j.addma.2017.08.016.

[76] R. Rashid, S. H. Masood, D. Ruan, S. Palanisamy, R. A. Rahman Rashid, and M. Brandt, "Effect of scan strategy on density and metallurgical properties of 17-4PH parts printed by Selective Laser Melting (SLM)," *J. Mater. Process. Technol.*, vol. 249, pp. 502–511, Nov. 2017, doi: 10.1016/j.jmatprotec.2017.06.023.

[77] H. R. Lashgari, C. Kong, E. Adabifiroozjaei, and S. Li, "Microstructure, post thermal treatment response, and tribological properties of 3D printed 17-4 PH stainless steel," *Wear*, vol. 456–457, p. 203367, Sep. 2020, doi: 10.1016/j.wear.2020.203367.

[78] "Influence of scanning strategies on microstructure, residual stress, and corrosion behavior of 17-4 PH stainless steel fabricated by selective laser melting." Accessed: Mar. 25, 2024. [Online]. Available: https://journals.sagepub.com/doi/epub/10.1177/09544089221106263

[79] L. Zai *et al.*, "Laser Powder Bed Fusion of Precipitation-Hardened Martensitic Stainless Steels: A Review," *Met. - Open Access Metall. J.*, vol. 10, p. 255, Feb. 2020, doi: 10.3390/met10020255.

[80] S. Giganto, S. Martínez-Pellitero, J. Barreiro, and P. Zapico, "Influence of 17-4 PH stainless steel powder recycling on properties of SLM additive manufactured parts," *J. Mater. Res. Technol.*, vol. 16, pp. 1647–1658, 2022.

[81] I. K. Sarma, N. Selvaraj, and A. Kumar, "Influence of hexagonal scanning strategy island size on microstructure, residual stress, and corrosion behavior of 17-4 PH SS made by L-PBF," *Proc. Inst. Mech. Eng. Part J. Mater. Des. Appl.*, vol. 237, no. 5, pp. 1093–1108, May 2023, doi: 10.1177/14644207221136237.

[82] S. Vunnam, A. Saboo, C. Sudbrack, and T. L. Starr, "Effect of powder chemical composition on the as-built microstructure of 17-4 PH stainless steel processed by selective laser melting," *Addit. Manuf.*, vol. 30, p. 100876, 2019.

[83] D. Zhao *et al.*, "Abnormal three-stage plastic deformation in a 17-4 PH stainless steel fabricated by laser powder bed fusion," *Mater. Sci. Eng. A*, vol. 858, p. 144160, Nov. 2022, doi: 10.1016/j.msea.2022.144160.

[84] E. A. Lass, F. Zhang, and C. E. Campbell, "Nitrogen Effects in Additively Manufactured Martensitic Stainless Steels: Conventional Thermal Processing and Comparison with Wrought," *Metall. Mater. Trans. A*, vol. 51, no. 5, pp. 2318–2332, May 2020, doi: 10.1007/s11661-020-05703-6.

[85] W. Shuai, L. U. Zhijiang, Y. Chunguang, S. Minggang, and Y. Ke, "Antibacterial performance of 17-4PH stainless steel," *Chin. J. Mater. Res.*, vol. 28, no. 1, pp. 15–22, 2014.

[86] H. K. Rafi, D. Pal, N. Patil, T. L. Starr, and B. E. Stucker, "Microstructure and Mechanical Behavior of 17-4 Precipitation Hardenable Steel Processed by Selective Laser Melting," *J. Mater. Eng. Perform.*, vol. 23, no. 12, pp. 4421–4428, Dec. 2014, doi: 10.1007/s11665-014-1226-y.

[87] ASTM International, *Standard Specification for Precipitation-Hardening Stainless and Heat-Resisting Steel Plate, Sheet, and Strip*, A693-16, West Conshohocken, PA., Oct. 04, 2022. doi: 10.1520/A0693-16R22.

[88] M. Mahmoudi, A. Elwany, A. Yadollahi, S. M. Thompson, L. Bian, and N. Shamsaei, "Mechanical properties and microstructural characterization of selective laser melted 17-4 PH stainless steel," *Rapid Prototyp. J.*, vol. 23, no. 2, pp. 280–294, Mar. 2017, doi: 10.1108/RPJ-12-2015-0192.

[89] S. van der Walt *et al.*, "The scikit-image contributors," *Scikit-Image Image Process. Python PeerJ*, vol. 2, p. e453, 2014.

[90] J. C. Yen, F. J. Chang, and S. Chang, "A new criterion for automatic multilevel thresholding," *IEEE Trans. Image Process.*, vol. 4, no. 3, pp. 370–378, 1995, doi: 10.1109/83.366472.

[91] ASTM International, *ASTM E3: Standard Guide for Preparation of Metallographic Specimens*, Standard E3, West Conshohocken, PA., Jun. 12, 2017. doi: 10.1520/E0003-11.
[92] T. Degen, M. Sadki, E. Bron, U. König, and G. Nénert, *The HighScore suite*. (Dec. 2014).
[93] ASTM International, *ASTM E8/E8M – Standard Test Methods for Tension Testing of Metallic Materials*, Standard E8/E8M, West Conshohocken, PA, United States., Mar. 2024. doi: 10.1520/E0008_E0008M-24.
[94] H. Abdulla, H. An, I. Barsoum, and M. Maalouf, "Mathematical Modeling of Multi-Performance Metrics and Process Parameter Optimization in Laser Powder Bed Fusion," *Metals*, vol. 12, no. 12, p. 2098, 2022.
[95] A. Chniouel *et al.*, "Influence of substrate temperature on microstructural and mechanical properties of 316L stainless steel consolidated by laser powder bed fusion," *Int. J. Adv. Manuf. Technol.*, vol. 111, no. 11, pp. 3489–3503, Dec. 2020, doi: 10.1007/s00170-020-06316-4.
[96] W. E. King *et al.*, "Observation of keyhole-mode laser melting in laser powder-bed fusion additive manufacturing," *J. Mater. Process. Technol.*, vol. 214, no. 12, pp. 2915–2925, Dec. 2014, doi: 10.1016/j.jmatprotec.2014.06.005.
[97] S. M. H. Hojjatzadeh *et al.*, "Direct observation of pore formation mechanisms during LPBF additive manufacturing process and high energy density laser welding," *Int. J. Mach. Tools Manuf.*, vol. 153, p. 103555, Jun. 2020, doi: 10.1016/j.ijmachtools.2020.103555.
[98] L. Englert, V. Schulze, and S. Dietrich, "Concentric Scanning Strategies for Laser Powder Bed Fusion: Porosity Distribution in Practical Geometries," *Mater. Basel Switz.*, vol. 15, no. 3, p. 1105, Jan. 2022, doi: 10.3390/ma15031105.
[99] A. Ur Rehman, F. Pitir, and M. U. Salamci, "Laser Powder Bed Fusion (LPBF) of In718 and the Impact of Pre-Heating at 500 and 1000 °C: Operando Study," *Materials*, vol. 14, no. 21, Art. no. 21, Jan. 2021, doi: 10.3390/ma14216683.
[100] T. Mukherjee, H. L. Wei, A. De, and T. DebRoy, "Heat and fluid flow in additive manufacturing—Part I: Modeling of powder bed fusion," *Comput. Mater. Sci.*, vol. 150, pp. 304–313, Jul. 2018, doi: 10.1016/j.commatsci.2018.04.022.
[101] S. An, D.-R. Eo, H. Lim, I. Sohn, and K. Choi, "Prediction of martensitic transformation and residual stress field on 17–4 PH stainless steel fabricated by laser powder bed fusion," *Addit. Manuf.*, vol. 91, p. 104339, Jul. 2024, doi: 10.1016/j.addma.2024.104339.
[102] M. Alnajjar *et al.*, "Influence of microstructure and manganese sulfides on corrosion resistance of selective laser melted 17-4 PH stainless steel in acidic chloride medium," *Corros. Sci.*, vol. 168, p. 108585, May 2020, doi: 10.1016/j.corsci.2020.108585.
[103] K. Li *et al.*, "Homogenization timing effect on microstructure and precipitation strengthening of 17–4PH stainless steel fabricated by laser powder bed fusion," *Addit. Manuf.*, vol. 52, p. 102672, Apr. 2022, doi: 10.1016/j.addma.2022.102672.
[104] F. Villaret, X. Boulnat, P. Aubry, J. Zollinger, D. Fabrègue, and Y. de Carlan, "Modelling of delta ferrite to austenite phase transformation kinetics in martensitic steels: Application to rapid cooling in additive manufacturing," *Materialia*, vol. 18, p. 101157, Aug. 2021, doi: 10.1016/j.mtla.2021.101157.
[105] M. Villa *et al.*, "Aging 17-4 PH martensitic stainless steel prior to hardening: effects on martensitic transformation, microstructure and properties," *Materialia*, vol. 32, p. 101882, Dec. 2023, doi: 10.1016/j.mtla.2023.101882.
[106] F. Mas *et al.*, "Metallurgical characterization of coupled carbon diffusion and precipitation in dissimilar steel welds," *J. Mater. Sci.*, vol. 51, no. 10, pp. 4864–4879, May 2016, doi: 10.1007/s10853-016-9792-z.

[107] J. Liu *et al.*, “Discovering the role of the defect morphology and microstructure on the deformation behavior of additive manufactured Ti–6Al–4V,” *Mater. Sci. Eng. A*, vol. 859, p. 144202, 2022.
[108] M. Muhammad, S. Shao, and N. Shamsaei, “Effect of Defects on the Mechanical Properties of Laser Powder Bed Fused Ti-6Al-4V,” 2022, Accessed: May 23, 2025. [Online]. Available: https://repositories.lib.utexas.edu/items/e4582bba-144b-4257-bbaf-5755635557ec
[109] G. Han, Z. J. Xie, L. Xiong, C. J. Shang, and R. D. K. Misra, “Evolution of nano-size precipitation and mechanical properties in a high strength-ductility low alloy steel through intercritical treatment,” *Mater. Sci. Eng. A*, vol. 705, pp. 89–97, Sep. 2017, doi: 10.1016/j.msea.2017.08.061.
[110] K. Li, S. Sridar, S. Tan, and W. Xiong, “Effect of homogenization on precipitation behavior and strengthening of 17-4PH stainless steel fabricated using laser powder bed fusion,” Dec. 12, 2021, *arXiv*: arXiv:2112.06289. Accessed: May 28, 2024. [Online]. Available: http://arxiv.org/abs/2112.06289
[111] R. Huang *et al.*, “Additive manufacturing of 17-4PH stainless steel: Effect of heat treatment on microstructure evolution and strengthening behavior,” *Mater. Sci. Eng. A*, vol. 908, p. 146770, Aug. 2024, doi: 10.1016/j.msea.2024.146770.
[112] P. D. Nezhadfar, M. Masoomi, S. Thompson, N. Phan, and N. Shamsaei, “Mechanical properties of 17-4 PH stainless steel additively manufactured under Ar and N2 shielding gas,” *Proc. 29th Annu. Int. Solid Free. Fabr. Austin TX USA*, pp. 13–15, 2018.
[113] H. E. Sabzi, S. Maeng, X. Liang, M. Simonelli, N. T. Aboulkhair, and P. E. J. Rivera-Díaz-del-Castillo, “Controlling crack formation and porosity in laser powder bed fusion: Alloy design and process optimisation,” *Addit. Manuf.*, vol. 34, p. 101360, Aug. 2020, doi: 10.1016/j.addma.2020.101360.
[114] P. Auguste, A. Mauduit, L. Fouquet, and S. Pillot, “Study on 17-4 PH stainless steel produced by selective laser melting,” *UPB Sci Bull Ser B Chem Mater Sci*, vol. 80, no. 4, pp. 197–210, 2018.